

Effect of grain boundaries and partial substitution of transition metals on thermoelectric properties of higher manganese silicide

Swapnil Chetan Ghodke

A Dissertation Submitted to
Nagoya University
In Partial Fulfillment of the Requirements for
The Degree of Doctor of Engineering



Department of Crystalline Materials Science,
Graduate School of Engineering
Nagoya University, Japan - 4648601

July, 2016

Declaration

I declare that this written submission represents my ideas in my own words, and where others ideas or words have been included, I have adequately cited and referenced the original sources. I also declare that I have adhered to all principles of academic honesty and integrity and have not misrepresented or fabricated or falsified any idea/data/fact/source in my submission. I understand that any violation of the above will be a cause for disciplinary action by the Institute and can also evoke penal action from the sources that have thus not been properly cited, or from whom proper permission has not been taken when needed.

(Signature)

Swapnil Chetan Ghodke

481361057

Approval Sheet

This thesis entitled “Effect of grain boundaries and partial substitution of transition metals on thermoelectric properties of higher manganese silicide” by Swapnil Chetan Ghodke is approved for the degree of Doctor of Engineering by Nagoya University, Japan.

Dr. Hiroshi Ikuta

Professor

Crystalline materials science, Nagoya University,

Examiner

Dr. Tsunehiro Takeuchi

Professor

Energy materials, Toyota Technological Institute,

Examiner

Dr. Koh Saitoh

Associate Professor

Crystalline materials science, Nagoya University,

Examiner

Dr. Takashi Itoh

Associate Professor

Materials science and engineering, Nagoya University

Examiner

Dr. Kazumasa Iida

Associate Professor

Crystalline materials science, Nagoya University,

Examiner

Acknowledgements

It was like a dream came true, when I got selected for **JICA-IITH FRIENDHIP** scholarship to study in one of the premier institute in the world, **Nagoya University**. I would consider this as a golden opportunity that had changed my life. This was all because of the people who trusted my abilities and allowed me to explore my research interest.

The extraordinary journey began with the acceptance email from **Prof. T.Takeuchi** and **Prof H. Ikuta** to join as a PhD student in Ikuta laboratory. I am really thankful to them as they gave me a chance to do my research on thermoelectrics, for which I always had an interest to work. Their guidance and constant motivation always inspired me to look for the positive in any research outcome.

Though, I was nervous in the beginning to go abroad, particularly in Japan where I could have problems with communication, food or culture. The nervousness passed in no time, it's all because of the new friends who joined my life. I thankful to my entire lab meet for helping me in problems and supporting me to get used to this Japanese life. I really appreciate all the efforts that were made to make an English atmosphere for the lab activities.

I would like to show my sincere thanks to all JICA staff specially **Komoto san, Matsuo san, Kawabuchi san, Kurono san, Ito san, Chihiro san** for helping me in any tiniest problem.

I want to thank all my friends for being my constant source of motivation and special thanks to **Yamamoto san, Sakamoto san, Naoya san, Omprakash, Iizuka san, Hiroi san, Mr. Anubhav, Mr. Ashish, Mr. Bhupendra, Mr. Mahendra, Ms. Swati, Ms. Manjiri** and my **team MASS** for being with me in my good as well as bad time and thanks for making my days memorable. Thank you for making Japan as my second home.

Last but not the least I would acknowledge the benelovance of my family members **Akash, Anand, Sumit, my mom & dad**, my uncle & aunties and my grandparents for their constant love, encouragement, blessings and support during my study. I would not forget a special person who is always in my heart, my dearest **Hemu** mama.

Dedicated to

My family and friends

My beloved grandfather Shri **Sudamrao Ghodke**

My uncle Shri **Hemant Gawali**

Abstract

The non-renewable fossil fuels in the form of crude oil, coal, or natural gas are being used to fulfill the energy need of our modern society. The energy conversion efficiency has been limited and more than 60% of available energy is wasted in the form of heat. Here, thermoelectric generators (TEGs) are believed to play a key role to convert the waste form of heat energy into useful electrical energy. TEGs with efficiency 10% can save billions of dollars when they are operational on large scale worldwide.

Thermoelectric materials used for commercial TEGs are the compounds with Pb, Te, Ag, Ge, Sb, etc. Considering the European and Japanese norms for limiting hazardous elements for technological applications TEGs would be a harmful technology. So it's a need in thermoelectric research to reconsider developing this technology from start, by finding alternatives and designing new guiding principles. One of the most promising alternative material containing cheap and non-toxic elements, while possessing a large magnitude of ZT is higher manganese silicide (HMS) stabilized at MnSi_γ ($1.73 \leq \gamma \leq 1.75$). Unfortunately, the ZT -value is not competitive with the commercially available thermoelectric materials. The need to improve the performance of higher manganese silicide has drawn our attention to investigate a new technique that can enhance the ZT .

In this study, we focused on preparing cheapest and most efficient higher manganese silicide compound for the thermoelectric generator by introducing two different strategies 1) energy filtering effect to improve the power factor and 2) partial substitution of transition metals on Mn site to tune the carrier concentration together with heavy atoms substitution to reduce lattice thermal conductivity. Here, we have tried to investigate the effect of carrier filtering due to secondary phases and grain boundaries. With the reference of Mn-Si binary phase diagram we synthesized different samples in silicon deficient and silicon rich regions, forming MnSi and Si precipitates, respectively. We employed a liquid quenching technique to obtain high density of grain boundary. The result suggests the energy filtering by grain boundaries could be an effective method to enhance performance by 30%.

The second strategy worked well to find out the optimal carrier concentration both for p-type and n-type by Cr and Fe substitution. The liquid quenching technique has helped us to improve the solubility for Cr, Fe, W and Re. We observed a reduction in grain size by a small amount of substitution. A large value of $ZT \sim 0.5$ at 700K was obtained by simultaneous substitution of Fe and W, which was the highest ZT reported for n-type HMS. The Re

substitution was very effective in reducing the lattice thermal conductivity to improve ZT more than unity above 900K. Hence, the strategy of implying energy filtering effect by grain boundaries in Re-HMS worked well to improve the power factor and could increase ZT by more than 20%. All the microstructural and physical property analyses has been systematically reported in this thesis.

List of papers

1. **Swapnil Ghodke**, Naoya Hiroishi, Akio Yamamoto, Hiroshi Ikuta, Masaharu Matsunami, Tsunehiro Takeuchi, “*Enhanced Thermoelectric Properties of W- and Fe-Substituted MnSi γ* ”, *J. Electr. Mat.*, (2016), DOI: 10.1007/s11664-016-4688-x
2. **Swapnil Ghodke**, Akio Yamamoto, Hiroshi Ikuta, Tsunehiro Takeuchi, “*Thermoelectric properties of higher manganese silicide containing small amount of MnSi/Si nanoparticles*”, *Ceramic trans*, Vol. **255** (2016), pp. 115-122
3. **Swapnil Ghodke**, Akio Yamamoto, M. Omprakash, Hiroshi Ikuta, Tsunehiro Takeuchi, *Thermoelectric properties of super-saturated Cr doped MnSi γ* “. *Materials Transactions*. (Submitted) 2016
4. A. Yamamoto, **S. Ghodke**, H. Miyazaki, M. Inukai, Y. Nishino, M. Matsunami, and T. Takeuchi, “*Thermoelectric properties of super-saturated Re solid solution of higher manganese silicides*” *Jpn. J. Appl. Phys.*, Vol. **55** (2016),pp. 020301(1-4)
5. A. Yamamoto, **S. Ghodke**, H. Miyazaki, Y. Nishino, M. Matsunami, and T. Takeuchi “*Thermoelectric properties of Al-Mn-Si based C54 phase containing small amount of C40 phase*”. *Mater. Trans*, Vol. **57** (2016), No. 7, p. 1055-1058
6. Tsunehiro Takeuchi, Akio Yamamoto, **Swapnil Ghodke** “*Development of thermoelectric materials consisting solely of environmental friendly elements*”. *Mater. Trans*, Vol. **57** (2016), No. 7, pp. 1029-1034

List of presentations and posters

A. International

1. **Swapnil Ghodke**, A. Yamamoto, H. Ikuta, T. Takeuchi, *Enhancement of power factor by energy filtering effect in Re substituted HMS*, The 35th International Conference & the 1st Asian Conference on Thermoelectrics (ICT/ACT 2016), Wuhan, China, **(Oral)**
2. Akio Yamamoto, **Swapnil Ghodke**, Masaharu Matsunami, Tsunehiro Takeuchi, *Thermoelectric performance of higher manganese silicide containing a small amount of 5d transition metal elements*, The 35th International Conference & the 1st Asian Conference on Thermoelectrics (ICT/ACT 2016), Wuhan, China, **(Poster)**
3. **Swapnil Ghodke**, A. Yamamoto, H. Ikuta, T. Takeuchi, “*Thermoelectric properties of higher manganese silicide containing small amount of MnSi/Si nano-particles*”, 11th International Conference on Ceramic Materials and Components for Energy and Environmental Applications (CMCEE-11), Vancouver, Canada, 14- 19 June 2015, **(Oral)**
4. **Swapnil Ghodke**, N. Hiroishi, A. Yamamoto, H. Ikuta, T. Takeuchi, “*Effect of microstructure on thermoelectric properties of Higher Manganese Silicide (MnSi_y)*”, Connect IITH 2015, Tokyo, 24-25 Aug 2015, **(Oral and Poster)**
5. **Swapnil Ghodke**, N. Hiroishi, A. Yamamoto, H. Ikuta, T. Takeuchi, “*Development of high performance thermoelectric material by using energy dependent scattering effects*”, Indo-Japan Human Resource Forum (HRF) , Tokyo, 1st Aug 2014, **(Poster)**
6. **Swapnil Ghodke**, N. Hiroishi, A. Yamamoto, H. Ikuta, T. Takeuchi, “*Synthesis of higher manganese silicides to study the energy dependent scattering effect*”, 5th ISAJ Symposium: Advances in Natural Sciences & Technologies, 1 Dec 2014, **(Oral and Poster)**

B. Domestic

1. **Swapnil Ghodke**, A. Yamamoto, H. Ikuta, T. Takeuchi, “*Evolution of transport properties with microstructure in Re doped MnSi γ* ”, 158th Annual spring Meeting (JIM), 24 March 2016, Tokyo (**Oral**)
2. **Swapnil Ghodke**, A. Yamamoto, H. Ikuta, T. Takeuchi, “*Enhancement of power factor by energy filtering effect in Re substituted HMS*”, 63rd JSAP spring meeting, 21 March 2016, Tokyo (**Oral**)
3. **Swapnil Ghodke**, A. Yamamoto, H. Ikuta, T. Takeuchi, “*Effect of silicon nano particles on thermoelectric properties of higher manganese silicide*”, 62rd JSAP spring meeting, 12 March 2015, Tokyo (**Oral**)
4. **Swapnil Ghodke**, N. Hiroishi, A. Yamamoto, H. Ikuta, T. Takeuchi, “*Thermoelectric properties of W-substituted bulk higher manganese silicide*”, The 76th JSAP Autumn Meeting, , 13-16 Sept 2015, Nagoya (**Oral**)
5. **Swapnil Ghodke**, N. Hiroishi, A. Yamamoto, H. Ikuta, T. Takeuchi, “*Study of Energy Filtering Scattering Effect on Higher Manganese Silicide*”, 155th Annual Autumn Meeting 2014 (JIM), 24 – 26 September 2014, (**Oral**)
6. **Swapnil Ghodke**, N. Hiroishi, A. Yamamoto, H. Ikuta, T. Takeuchi, “*Synthesis and characterization of heterogeneous higher manganese silicides to study the energy dependent scattering effect*”, 11th Annual meeting of the thermoelectric society of Japan ,29-30 Sept 2014, (**Oral**)

Nomenclature

HMS	Higher manganese silicide
LQ	Liquid quenched
a, b, c	Crystal unit cell parameter
RT	Room temperature
SEM	Scanning electron microscope
XRD	X-ray diffraction
SPS	Spark plasma sintering
DSC	Differential scanning calorimetry
EDX	Energy dispersive x-ray spectroscopy
TEM	Transmission electron microscope
TGA	Thermal gravimetric analysis
DTA	Differential thermal analysis
S	Seebeck coefficient
ρ	Electrical resistivity
κ	Thermal conductivity
κ_{el}	Electron thermal conductivity
κ_l	Lattice thermal conductivity
$S^2\sigma$	Power factor
TE	Thermoelectric
VEC	Valence electron concentration

Contents

Declaration.....	ii
Approval sheet.....	iii
Acknowledgements.....	iv
Abstract.....	vi
List of publications.....	viii
List of presentations (International).....	ix
List of presentations (domestic).....	x
Nomenclature	xi
1 Introduction	1
1.1 Overview	
1.2 History	
1.3 Applications	
1.4 Efficiency of energy conversion	
1.5 Thermoelectric materials	
1.5.1 Commercial TE materials	
1.5.2 Limitations and drawbacks	
1.6 Reference	
2 Literature Survey.....	8
2.1 Electronic structure of thermoelectric materials	
2.1.1 Linear response theory	
2.2 Guiding principles for high performance TE materials	
A. Conditions for large A-factor	
B. Conditions for large B-factor	
2.3 Prospective TE material: Higher Manganese Silicide (HMS)s	
2.4 Strategies to enhance ZT	
A Carrier concentrations tuning	
B Energy filtering effect: improving power factor	
C Reducing lattice thermal conductivity	

2.5 Motivation and objectives	
2.6 References	
3 Experimental Details.....	29
3.1 Synthesize of non-doped MnSi γ .	
3.1.1 Flow chart for synthesis: non-doped MnSi γ	
3.1.2 Flow chart for synthesis: Substitution of Cr/Fe/W/Re	
3.2 Characterization techniques	
3.2.1 X-ray diffraction	
3.2.2 Scanning electron microscopy/ EDX	
3.2.3 Steady state method: Seebeck measurement	
3.2.4 4-probe method: electrical resistivity measurement	
3.2.5 Laser flash method: thermal conductivity	
3.2.7 Differential thermal analysis	
4 TE properties of HMS containing small amount of MnSi/Si nano-particles.....	43
4.1 Introduction	
4.2 Experimental procedure	
4.3 Results	
4.4 Discussion	
4.5 Conclusion	
4.6 References	
5 Thermoelectric properties of super saturated Cr substituted MnSiγ.....	53
5.1 Introduction	
5.2 Experimental procedure	
5.3 Results	
5.4 Discussion	
5.5 Conclusion	
5.6 References	

6 Enhanced thermoelectric properties of W and Fe substituted MnSi_y.....	64
6.1 Introduction	
6.2 Results	
6.3 Discussion	
6.4 Conclusion	
6.5 References	
7 Enhancement of power factor by energy filtering in Re-substituted HMS.....	75
7.1 Introduction	
7.2 Results for bulk samples	
7.3 Strategy to enhance <i>ZT</i> by energy filtering effect in Re-HMS	
7.4 Results for LQ and SPS samples	
7.5 Discussion	
7.6 Conclusion	
7.6 References	
8 Conclusion.....	88

Chapter 1

Introduction

1.1 Overview

The non-renewable fossil fuel in the form of crude oil, coal, or natural gas is being used to fulfill the energy need of our modern society. The electrical energy comes with a cost for industrial as well as household usage. Considering the limited efficiency of energy generation and utilization, we need to utilize the energy that is given out to atmosphere in the form of heat. Here, thermoelectric generators (TEG's) can play a key role to convert waste form of heat energy into useful electrical energy.

1.2 History

In 1821, German physicist Thomas Johann Seebeck first discovered that an electrical current was generated at the junction of two different metals when a temperature difference was applied between the both ends of specimen. This effect of converting heat into electricity was named as Seebeck effect, which is applied for thermoelectric generators (TEG's) for converting waste heat into electrical energy.

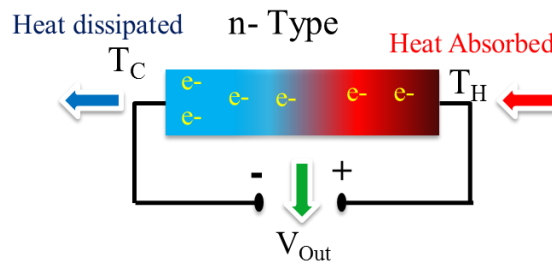


Figure 1.1 Seebeck effect

The reverse Seebeck effect was discovered by French physicist Jean Charles Athanase Peltier in 1834. He observed that when current was applied to a closed circuit made of two different conductors, a temperature difference was observed at two junctions of the circuit. This effect was called as Peltier effect.

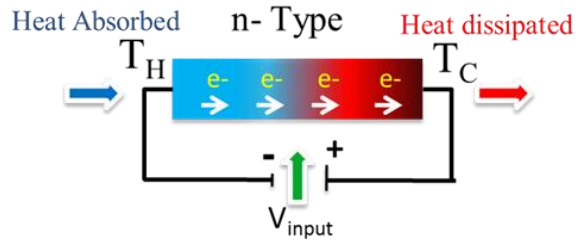


Figure 1.2 Peltier effect

The 3rd thermoelectric effect was discovered by William Thomson. He observed that when current is passed through conductor placed in a field of finite temperature gradient, then the heat generation or absorption, that is proportional to both the temperature gradient and the current, was observed together with the Joule heating. The effect is known as Thomson effect.

1.3 Applications of thermoelectrics

As mentioned above, Seebeck effect has wide applications in conversion of waste heat to useful form of electrical energy.

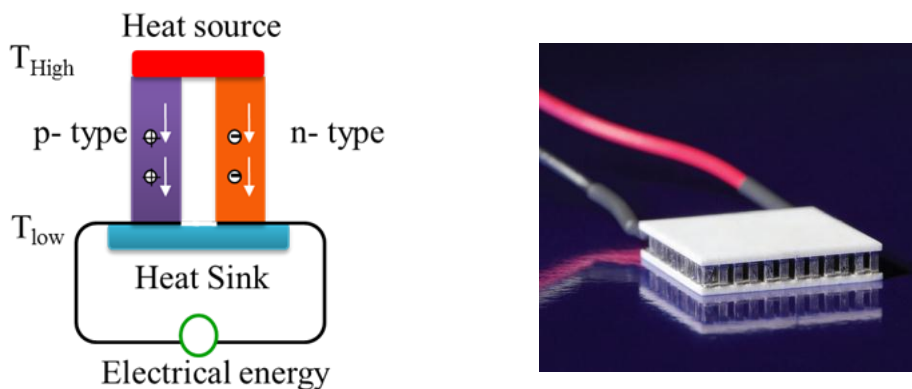


Figure 1.3 Schematic diagram of p-n junction (left), thermoelectric module TEG (right)

In a typical TEG module many p-type and n-type legs are connected in series for electrical conduction and parallel for thermal conduction. This technology has been used for energy harvesting for example in automobiles [1], power plants or industries. It's been used in space applications to generate electricity by converting decay heat of radioisotope degradation [2].

The potential of this technology has been improved with time. Ongoing worldwide research works on thermoelectric are exclusively focused on developing new materials with high performance.



Figure 1.4 TEGs for automobiles (left) and for space applications (right)
[\(http://www.spacesafetymagazine.com/aerospace-engineering/nuclear-propulsion/energy-resources-space-missions/\)](http://www.spacesafetymagazine.com/aerospace-engineering/nuclear-propulsion/energy-resources-space-missions/)

1.4 Efficiency of energy conversion and figure of merit ZT

The main objective of this work is to develop thermoelectric materials and generators for effectively recovering waste heat. The efficiency of energy conversion for thermoelectric generator is an increasing function of the dimensionless figure of merit, which is determined by the thermoelectric properties of p-type and n-type thermoelectric materials. The relationship between the maximum energy conversion efficiency (η) and ZT in the thermal power generation can be described by the following equation. [3]

$$\eta = \frac{T_H - T_C}{T_H} \frac{\sqrt{1 + ZT} - 1}{\sqrt{1 + ZT} + \frac{T_C}{T_H}} \quad (1.1)$$

Here, T_H and T_C represent the temperature of hot end and cold end respectively. The maximum energy conversion efficiency is also a fraction of Carnot efficiency. Figure 1.5 shows the relationship between efficiency of energy conversion, ZT and temperature gradient. It is easy to understand that as temperature gradient increases, but considering the diffused heat available the value of ZT becomes more important. Hence to convert energy efficiently the material should have a large ZT value.

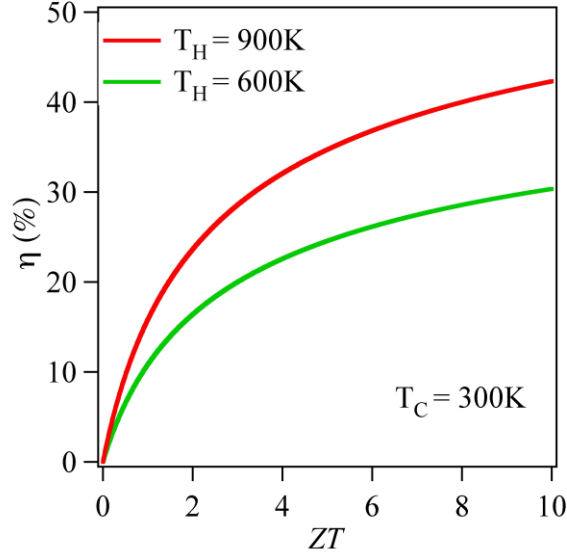


Figure 1.5 Efficiency of energy conversion η vs. ZT

The dimensionless figure of merit ZT in Eq. (1.2) is defined by Seebeck coefficient (S), electrical conductivity (σ), and thermal conductivity (κ) at absolute temperature T .

$$ZT = \frac{(S^2 \sigma)T}{\kappa_e + \kappa_l} \quad (1.2)$$

The Seebeck coefficient (S) is defined as the coefficient of temperature gradient for the induced thermoelectric field $\mathbf{E} = S \nabla T$. The thermal conductivity κ is defined as the coefficient of temperature gradient for the heat current $\mathbf{j}_Q = -\kappa \nabla T$ and mainly determined as the sum of lattice thermal conductivity κ_l and electron thermal conductivity κ_e .

A large magnitude of Seebeck coefficient and that of electrical resistivity leads to a large magnitude of ZT and consequently to a high performance of thermoelectric device, because the former leads to a large thermoelectric voltage and the latter to a small internal resistance. On the other hand, a small magnitude is preferable for the thermal conductivity, which stays in the denominator of equation of ZT , because the small magnitude of thermal conductivity indicates the small loss of heat passing through the material. It is also very important to know that the

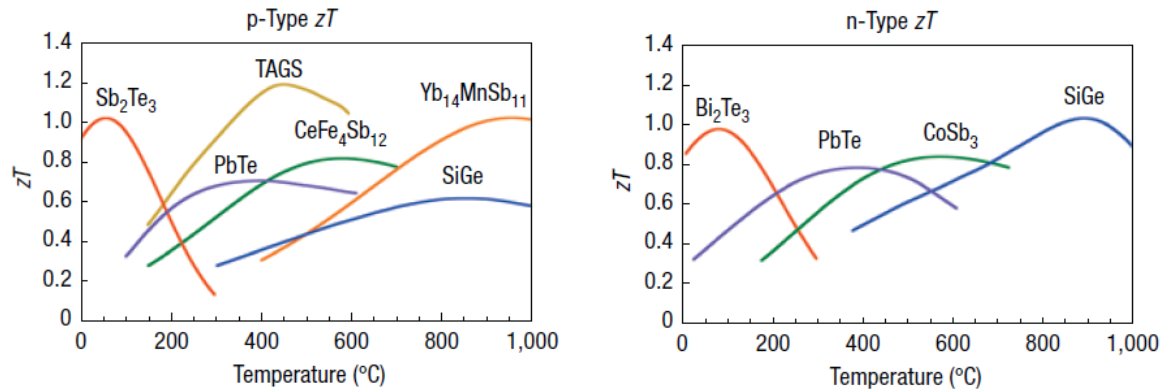


Figure 1.6 High performance p-type and n-type thermoelectric materials [5]

quantity $PF = S^2 \sigma$ is called as the power factor and often used to evaluate the electrical power generated by the thermoelectric devices [4].

1.5 Thermoelectric materials

1.5.1 Commercial TE materials

Intensive research work on the TE materials had been done in the last 3 decades. Researchers have found materials with $ZT = 1$, which are called as state of the art materials, as they are being used in practical applications. Figure 1.6 shows some of the typical examples of p-type and n-type high performance thermoelectric materials. It can be confirmed that every compound has high ZT at certain temperature, known as operating temperature. Sb_2Te_3 and Bi_2Te_3 are used for low temperature applications, whereas TAGS (GeTe-AgSbTe₂) alloy for high temperature applications. The diffused waste heat available from industries, automobiles or from other power plant is from high temperature around 600°C. So in our research we have focused on the materials with high operating temperature.

1.5.2 Limitations and drawbacks

It is worth mentioning that the examples mentioned in Fig. 1.6 are mainly alloys with Te and/or Pb, which is toxic element. Ge, Te, and Ag are known to be expensive. The toxicity and high cost are the disadvantages that made it difficult to mass produce the thermoelectric devices and limit the usage for large scale applications. So there is a strong demand to develop high performance cheap and environmental friendly thermoelectric materials.

1.6 Purpose of this thesis

1. To develop the high performance thermoelectric materials solely using cheap, environmentally friendly elements.
2. New technique energy filtering effect is investigated and employed for enhancing thermoelectric performance of selected materials.
3. Besides, lattice thermal conductivity is decreased without altering electron transport properties by employing small amount of heavy element substitutions.
4. Obtaining high ZT by combining energy filtering effect together with heavy element substitution.

1.7 References

1. C. B. Vining, Nat. Mater. **8**, 83 (2009).
2. Energy Resources for Space Missions, (<http://www.spacesafetymagazine.com/aerospace-engineering/nuclear-propulsion/energy-resources-space-missions/>).
3. H. J Goldsmid, CRC Handbook of Thermoelectrics ed. by D. M. Rowe (CRC Press, Boca Raton, 1995), pp. 22-23
4. A. Mehdizadeh Dehkordi, M. Zebarjadi, J. He, and T. M. Tritt, Mater. Sci. Eng. R Reports **97**, 1 (2015).
5. A. D. Lalonde, Y. Pei, H. Wang, and G. Jeffrey Snyder, Mater. Today **14**, 526 (2011).

Chapter 2

Strategies to obtaining a large ZT value for materials consisting solely of cheap, environmentally friendly elements

2.1 Electronic structure of thermoelectric materials

Thermoelectric properties can be derived from electronic structure of a material.

2.1.1 Linear response theory

Linear response theory is used to calculate the electronic structure [1]. The thermoelectric properties are described by considering electric field E and temperature gradient ∇T . The electric current is described as:

$$\mathbf{J} = K_0 \mathbf{E} - \frac{K_1}{|e|T} (-\nabla T) \quad (2.1)$$

The first term represents the change in the distribution function in momentum space created by the external electric field \mathbf{E} and the second term for the change in distribution function caused by the temperature gradient. K_n is transport integral.

$$K_n = \int \sigma(\varepsilon, T) (\varepsilon - \mu)^n \left(-\frac{\partial f_{FD}(\varepsilon, T)}{\partial \varepsilon} \right) d\varepsilon \quad (2.2)$$

$\sigma(\varepsilon, T)$ is called the spectral conductivity that represents the "ability of electronic states staying at ε to contribute to the electrical conduction at a temperature T ". As each electron carries energy with it, the energy flow is represented as:

$$\mathbf{JQ} = \frac{K_1}{|e|} \mathbf{E} - \frac{K_2}{e^2 T} (-\nabla T) \quad (2.3)$$

Relationship of electrical conductivity $\sigma(T)$ can be deduced in absence of temperature gradient, the Seebeck coefficient $S(T)$ in absence of electric field and electron thermal conductivity by substituting value of $\sigma(T)$ and $S(T)$ in eqn. 2.

$$\begin{aligned}
\mathbf{J} &= \sigma(T)\mathbf{E} \\
\mathbf{E} &= S(T)\nabla T \\
J_Q &= \kappa_{el}(T)(-\nabla T)
\end{aligned} \tag{2.4}$$

The complete solutions for $S(T)$, $\sigma(T)$ and $\kappa_{el}(T)$ are expressed in eqn. (2.5) – (2.7)

$$\sigma(T) = 1/\rho(T) = \int \sigma(\varepsilon, T) \left(-\frac{\partial f_{FD}(\varepsilon, T)}{\partial \varepsilon} \right) d\varepsilon \tag{2.5}$$

$$S(T) = -\frac{1}{|e|T} \frac{\int \sigma(\varepsilon, T)(\varepsilon - \mu) \left(-\frac{\partial f_{FD}(\varepsilon, T)}{\partial \varepsilon} \right) d\varepsilon}{\int \sigma(\varepsilon, T) \left(-\frac{\partial f_{FD}(\varepsilon, T)}{\partial \varepsilon} \right) d\varepsilon} \tag{2.6}$$

$$\begin{aligned}
\kappa_{el} &= \frac{1}{e^2 T} \int \sigma(\varepsilon, T)(\varepsilon - \mu) \left(-\frac{\partial f_{FD}(\varepsilon, T)}{\partial \varepsilon} \right) d\varepsilon - \frac{1}{e^2 T} \frac{\left\{ \int \sigma(\varepsilon, T)(\varepsilon - \mu) \left(-\frac{\partial f_{FD}(\varepsilon, T)}{\partial \varepsilon} \right) d\varepsilon \right\}^2}{\int \sigma(\varepsilon, T) \left(-\frac{\partial f_{FD}(\varepsilon, T)}{\partial \varepsilon} \right) d\varepsilon} \\
&= \frac{1}{e^2 T} \int \sigma(\varepsilon, T)(\varepsilon - \mu) \left(-\frac{\partial f_{FD}(\varepsilon, T)}{\partial \varepsilon} \right) d\varepsilon - S^2 \sigma T
\end{aligned} \tag{2.7}$$

These formulas are basically dependent on two functions, spectral conductivity $\sigma(\varepsilon, T)$ (material property) and Fermi-Dirac distribution function f_{FD} , together with one parameter, the chemical potential $\mu(T)$.

In the case of isotropic system, the spectral conductivity can be expressed in terms of electronic density of states $N(\varepsilon)$, mean group velocity $v_G(\varepsilon)$ of electron, and the relaxation time $\tau(\varepsilon, T)$.

$$\sigma(\varepsilon, T) = \frac{e^2}{3} N(\varepsilon) v_G^2(\varepsilon) \tau(\varepsilon, T) = \frac{e^2}{3} N(\varepsilon) v_G(\varepsilon) l(\varepsilon, T) \tag{2.8}$$

2.2 Guiding principles for high performance TE materials

Guiding principles have been constructed for developing high performance thermoelectric materials. The thermoelectric properties can be calculated by knowing the spectral conductivity of a material [2,3].

The formulas in eqn. (2.5) – (2.7) are expressed in terms of Fermi-Dirac distribution function f_{FD} . The derivatives of this functions are called as *window functions* $W_n = (\varepsilon - \mu)^n (-\partial f_{FD} / \partial \varepsilon)$, for $n = 0, 1$, and 2 . These window functions can be calculated at a given temperature of 50 K, 100 K, and 200 K, as shown in figure 1.

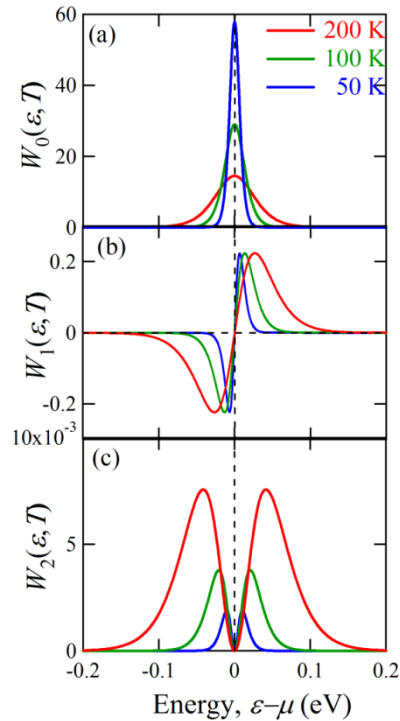


Figure 2.1 Window functions W_n ($n = 0, 1, 2$) as a function of $\varepsilon - \mu$.

These window function shows energy dependence in a few $k_B T$ range. The electrical conductivity is determined by $W_0 = (-\partial f_{FD} / \partial \varepsilon)$. W_0 shows a peak exactly at the chemical potential with a full-width-half-maximum of about $3.5 k_B T$. The peak becomes broader as the temperature is increased. This means that the energy range of carriers contributing to the electrical conductivity increases.

The Seebeck coefficient is strongly dominated by the product of $W_1 = (\varepsilon - \mu)(-\partial f_{\text{FD}} / \partial \varepsilon)$ and spectral conductivity. Here, W_1 has negative and positive maxima at $\varepsilon - \mu = \pm 1.7 k_B T$. It can be understood that to obtain a large Seebeck coefficient the spectral conductivity must show very different magnitudes at the energy ranges of $\varepsilon - \mu \sim 1.7 k_B T$ and $\varepsilon - \mu \sim -1.7 k_B T$.

The $W_2 = (\varepsilon - \mu)^2 (-\partial f_{\text{FD}} / \partial \varepsilon)$ governs the electron thermal describing the conductivity, where it shows two positive peaks above and below the chemical potential at $\varepsilon - \mu \sim \pm 2.4 k_B T$. It has a center null point at the chemical potential. This behavior makes it clear that the electrons contributing to electrical and thermal conductivity are from different energy ranges.

On the basis of the above theory we can modify the equation of ZT , to understand the conditions for high ZT

$$ZT = \frac{S^2 T}{\rho(\kappa_{el} + \kappa_{lat})} = \frac{S^2 T}{\rho \kappa_{el}} \left(\frac{1}{1 + \kappa_{lat} / \kappa_{el}} \right) \quad (2.9)$$

There are two factors $A = S^2 \sigma T / \kappa_{el}$, which can be calculated from spectral conductivity and chemical potential. A is dependent on the electronic structure, whereas, $B = 1 / (1 + \kappa_{lat} / \kappa_{el})$ depends on the ratio of $\kappa_{lat} / \kappa_{el}$. The maximum value of B is 1, so that it is necessary to have a large A factor to realize a large ZT value.

On the basis of facts described above, the necessities of electronic structure for high-performance thermoelectric materials possessing a large magnitude of A are described below [3];

A. The condition to obtain large A –factor

- a) A wide band gap exceeding $10 k_B T_0$ in energy-width, where T_0 is the working temperature of practical application.
- b) Multiple bands in the narrow energy range of a few $k_B T_0$ from band edge.
- c) Sharp increase of electronic density of states from band edge.

The condition (a) prohibits the reduction of Seebeck coefficient in association with bi-polar diffusion effect, and the condition (b) is important for the large magnitude of Seebeck coefficient. The condition (c) allows the chemical potential to move drastically with increasing temperature

for a larger magnitude of Seebeck coefficient with a large carrier concentration. The materials possessing these characteristics in their electronic structure must exhibit a large magnitude of A factor.

B. The condition to obtain large B –factor (Low κ_{lat})

The magnitude of B becomes large towards unity with a smaller magnitude of lattice thermal conductivity and a larger magnitude of electron thermal conductivity. The latter is already satisfied by the conditions of large magnitude of A , so that we have to find the conditions leading to small lattice thermal conductivity to realize a large magnitude of B .

$$\kappa_{lat} = \frac{1}{3} C_v v_g^2 \tau = \frac{1}{3} C_v v_g l_{ph} \quad (2.10)$$

Here lattice thermal conductivity is dependent on specific heat at constant volume C_v , the average group velocity v_g , phonon relaxation time τ or phonon mean free path l_{ph} . The lattice thermal conductivity is directly proportional to the phonon mean free path and it can be reduced by the strategies mentioned below.

The sophisticated solid-state-physics suggest that the objective materials should have at least one of the following conditions.

1. Large number of atoms per primitive cell
2. Partial substitution of heavy elements for the constituent elements in the materials consisting solely of lighter elements
3. Anharmonic oscillation of lattice vibration
4. Strong grain boundary scattering

The importance of these effects is described below in the following subsections.

1. Large number of atoms per primitive cell

The illustration (Fig. 2.2) can be used to understand the effect of large number of atoms in the unit cell.

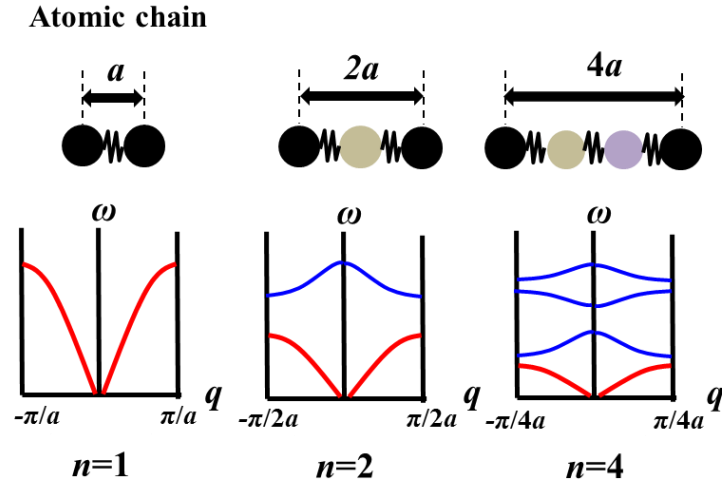


Figure 2.2 Phonon modes and number of atoms in unit cell

As we increase number of atoms (n) the phonon mode increases. The interaction of phonon modes with Brillouin zone increases the probability of Umklapp scattering. The Umklapp scattering thus reduces the mean group velocity of phonons and consequently the small magnitude of lattice thermal conductivity is realized.

Case (1) there is only one acoustic mode of vibration with same type atoms in unit cell. Case (2) by introducing one more atom the Brillouin zone becomes half and optical phonon mode appears. Case (3) 4 atoms further increases optical modes of vibration and the probability of scattering is maximum in this case.

2. Partial substitution of heavy elements for lighter elements

If the heavy element was partially substituted for lighter element, then a large disturbance is introduced into the crystal. Decrease of phonon relaxation time by introducing disorder of the crystal structure contributes to a reduction in the lattice thermal conductivity.

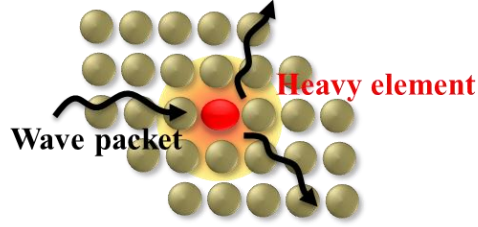


Figure 2.3 Effect of heavy element substitution

According to Klemans formula for lattice thermal conductivity [4],

$$\kappa_{lat} = \frac{1}{3} C_v \frac{4\pi v_G^5}{\Omega \omega^4 \Gamma} \quad (2.11)$$

Where, Ω is average volume of the atom, ω is the angular frequency of the phonons, v_G is the average velocity of the phonons. Γ indicates the degree of scattering (scattering intensity). The intensity of scattering increases by increasing the difference between the masses of substituted atoms M_i , M . The eqn. (2.12) shows that the Γ is directly proportional to the square of mass difference, therefore by having a small mass difference can be effective to reduce lattice thermal conductivity.

$$\Gamma = \sum_i c_i \left(\frac{M_i - M}{M} \right)^2 \quad (2.12)$$

This method can be used for the alloys, which are made up of only light elements or heavy elements; the partial substitution of heavy element in the former and the light element substitution in the latter case, can effectively reduce the lattice thermal conductivity. We have employed this technique in our work for HMS, as Mn and Si are light elements, we have

partially substituted heavy elements like W or Re for Mn. The results of lattice thermal conductivities are shown in respective chapters 6,7.

3. Anharmonic oscillations

The anharmonicity can occur by anisotropic local structure around the atom. The complex crystal structure can have different types of bonding such as metallic, ionic, covalent or van der Waals. These interatomic potential gets affected by such atomic forces, which increases the scattering probability of phonons.

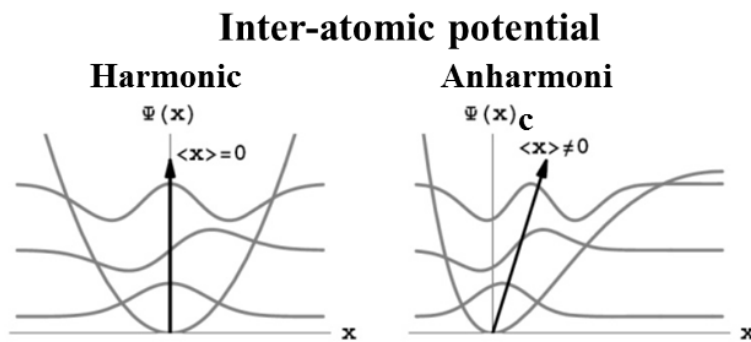


Figure 2.4 Schematic of harmonic and anharmonic oscillations

4. Grain boundary scattering

Every polycrystalline structure possesses defects known as grain boundaries. These grain boundaries have different crystal structure than the matrix phase. Also there are low angle and high angle grain boundaries depending on misorientation between the two grains. Hence this defect can act as scattering centers for the phonon. The grain boundary density can be increased in nano-structured materials made by means of top down or bottom up methods. This strategy of reducing lattice thermal conductivity had already been demonstrated successfully for several compounds like SiGe alloy or Bi_2Te_3 . The illustration in Fig. 2.5 shows the mechanism of phonon scattering at grain boundaries.

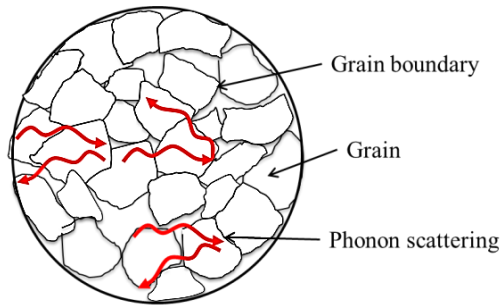


Figure 2.5 Phonon scattering at grain boundaries

2.3 Prospective TE material: Higher Manganese Silicide (HMS)

Higher manganese silicides are the intermetallic compounds in Mn-Si binary phase diagram with silicon content of 63 - 64 %. The “Higher” word comes from higher Mn concentration compared to all the di-silicide compounds. In the phase diagram HMS is not a eutectic compound but forms through the peritectic reaction. This means the synthesis is tricky as manganese mono silicide impurity phase, the melting temperature of which is very high at 1276 °C to be hardly removed, is involved in the HMS even at the composition of single HMS phase. MnSi shows metallic behavior due narrow band gap (~ 0.2 eV). The room temperature transport properties: 40 $\mu\text{V/K}$ Seebeck coefficient, good electrical conductivity ($0.2 \text{ m}\Omega\cdot\text{cm}$) due to large hole concentration and large thermal conductivity are not suitable for thermoelectric applications [5]. Therefore the syntheses parameters have to be carefully controlled to obtain the single phase of HMS.

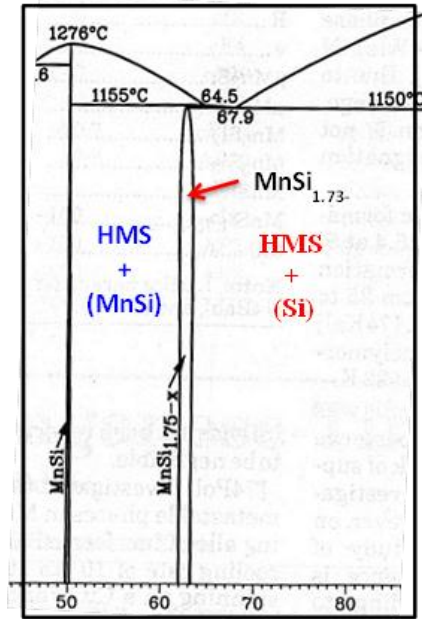


Figure 2.6 Mn-Si binary phase diagram [6]

There are 4 different crystal structures reported Mn_4Si_7 , $\text{Mn}_{11}\text{Si}_{19}$, $\text{Mn}_{15}\text{Si}_{26}$, and $\text{Mn}_{27}\text{Si}_{47}$ for HMS. This variation in structure makes the composition range of HMS slightly larger, and therefore the chemical formula is expressed as MnSi_γ ($1.73 \leq \gamma \leq 1.75$) [7-10]. The four different crystal structures are shown in Fig. 2.7, where Mn and Si sub systems are stacked together. These are famously known as Nowotny Chimney Ladder (NCL) because Si atoms are stacked in the form of ladder around Chimney of Mn atoms. The NCL structure is derived from TiS_2 type structure. The structures have unusual long c -axis compared to a -axis.

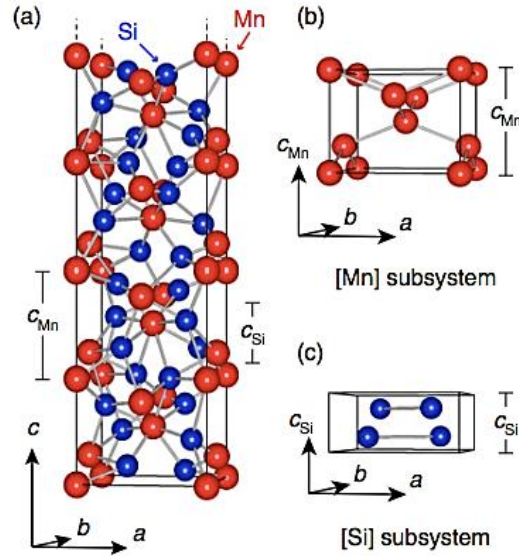


Figure 2.7 Nowotny chimney ladder structure of higher manganese silicide [12]

The ε - k dispersion for $Mn_{11}Si_{19}$ calculated by means of Full potential Linearized Augmented Plane Wave method with Generalized Gradient Approximation (FLAPW-GGA) is shown in Fig. 2.8. The calculated electronic structure clearly shows that the HMS possesses a wide band gap of 840 meV in width and the multiple bands existing near the band edge. This result suggests that HMS has an electronic structure suitable for thermoelectric materials. Using the calculated electronic structure, the estimated value of A -factor actually exceeded 4 at 1000 K, as shown in Fig. 2.9.

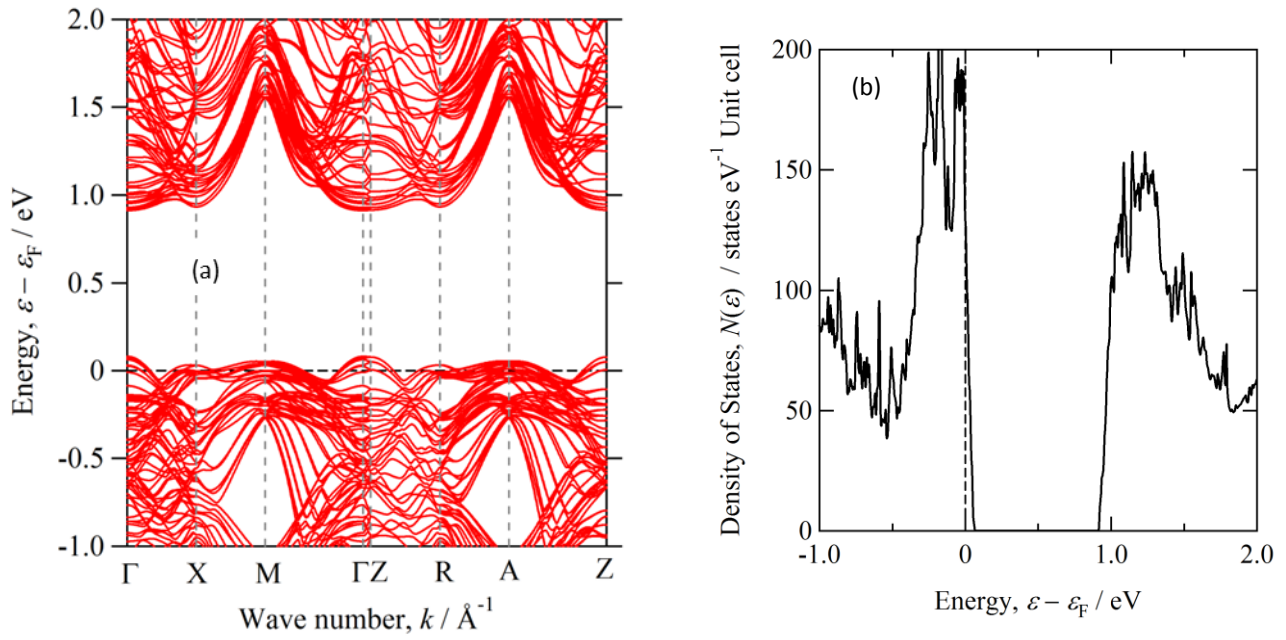


Figure 2.8 The (a) ε - k dispersion with electronic density of states for MnSi. (b) Energy dependence of density of states for MnSi.

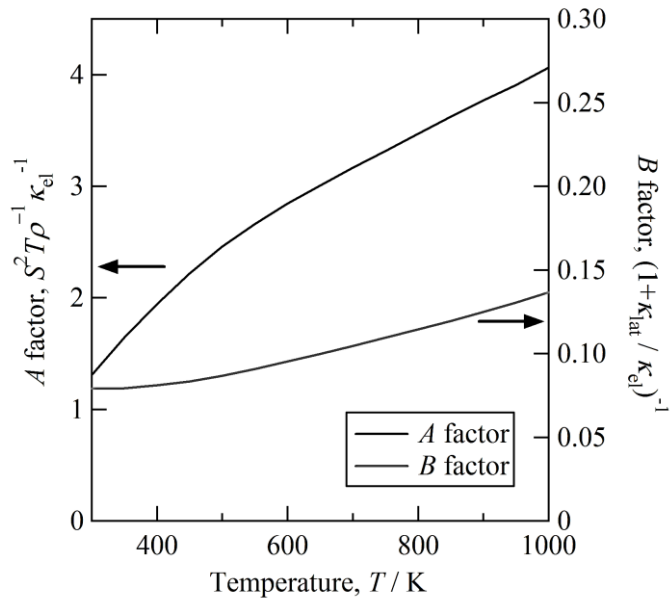


Figure 2.9 Temperature dependence of estimated A-factor for MnSi, [11]

The thermal stability of these transition metal NCl compounds is explained by 14 electron rule, which states that the each phase should have an average of 14 valence electrons per transition metal atom. If there is a deficiency in Si atoms, the material shows a p-type behavior. This means that it can show p-type and n-type behavior by doping hole/electrons.

HMS single crystals showed large anisotropy in TE properties, with high ZT along c-axis [20]. But to obtain single crystals of HMS without impurity of MnSi is very difficult. Polycrystalline samples are definitely preferable for practical applications. There are various reports for polycrystalline HMS synthesized by different techniques such as ball milling, solid state reaction, hot press, spark plasma sintering, induction melting or induction melting. The maximum ZT for non-doped p-type HMS was observed between 0.3- 0.55 above 700 K [12].

2.4 Strategies to enhance ZT of HMS

A. Tuning carrier concentration

The carrier concentration must be optimized in a region where the materials possess high ZT . This method has been used as a general principle to obtain high performance. Generally speaking, the insulators have a large Seebeck coefficient but low electrical conductivity and thermal conductivity [13]. The metallic materials have good thermal and electrical conductivity due to high carriers but low Seebeck coefficient. The optimal concentration for the largest ZT is in semiconductor region. Particularly degenerate semiconductors showed high thermoelectric performance. These conditions are schematically drawn in Fig. 2.10.

The thermoelectric properties are very sensitive to the carrier concentration and it can be tuned by partial substitution of elements. Recently, there are various reports on doping of HMS, where Cr and Fe atoms were substituted for Mn, and Ge or Al atoms were substituted for Si [21-25]. The results showed that the performance of HMS was improved by the carrier concentration tuning, but unfortunately the optimization was limited by the solubility limits of the doping elements. This means that the increase in solubility limits of such composition can further improve the performance. Thus, in this study we have tried to increase the solubility using a rapid quenching technique, which we have discussed in Chapter 5, Chapter 6, and Chapter 7.

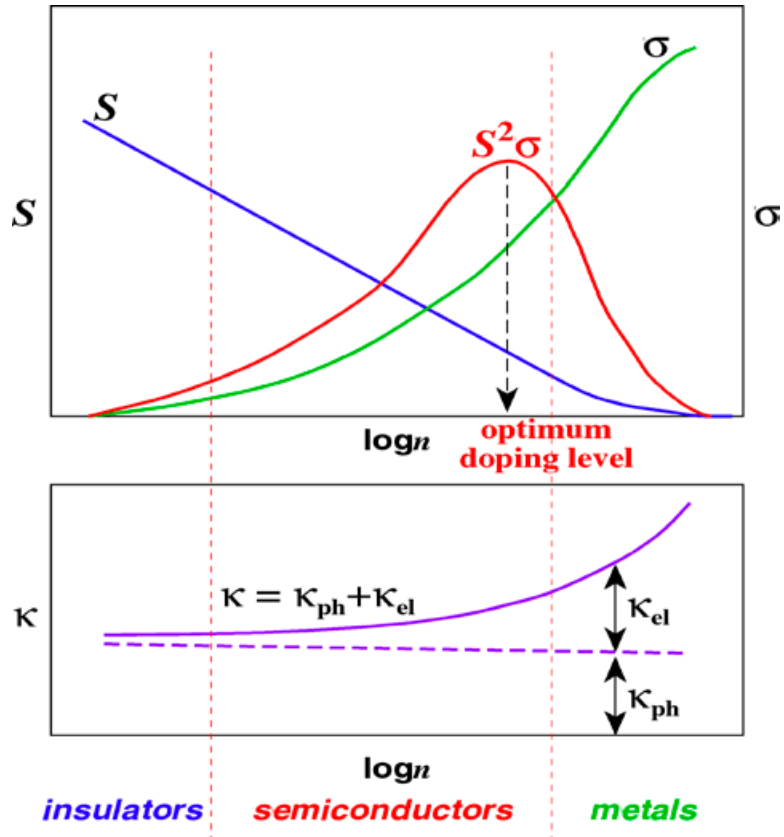


Figure 2.10 Carrier concentration dependence of S , σ , κ , and ZT [26]

B. Effect of energy dependent scatterings on thermoelectric properties.

The grain boundary can be assumed as a scattering center both for electrons and phonons. In case of phonon scattering, it reduces the phonon mean free path and consequently reduces lattice thermal conductivity. Many reports on reduction of lattice thermal conductivity by nanostructuring had been reported in past decade. On the other hand, the barriers introduced by the interfaces of inclusion /grain boundaries act as scattering centers for low energy carriers.

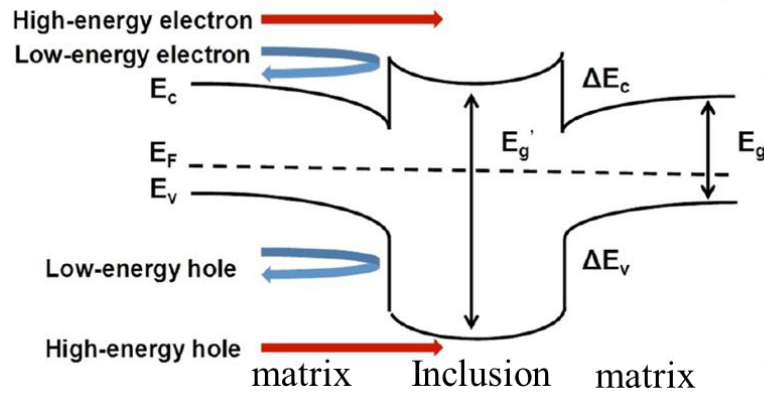


Figure 2.11 Schematic diagram of energy filtering effect having different n-type and p-type materials [13].

In case of n-type material, scattering of low energy electrons and filtering the high energy electron increases the Seebeck coefficient. However the scattering of carrier increases electrical resistivity, but the Seebeck is a square term and the slight increase in S makes large contribution to power factor. Similarly in p-type material only high energy holes are allowed by scattering low energy holes. Recently, Dong-Kyun Ko *et al.* reported that by making nano-composite with Pt nano-inclusion in Sb_2Te_3 matrix (Fig. 2.12), the Pt nano crystal (NC) act as a barrier for low energy carriers and the ZT was increased [15].

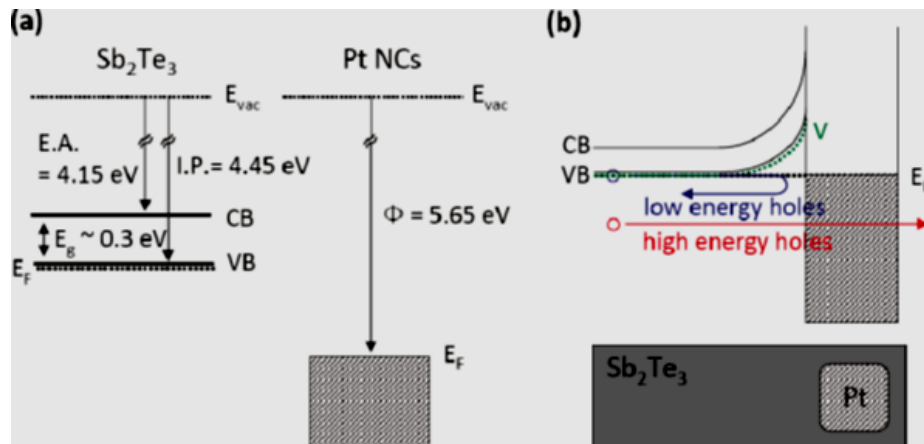


Figure 2.12 Schematic diagram of (a) valence band (VB) and conduction band (CB) near the fermi level for pure Sb_2Te_3 and Pt NCs. (b) Sb_2Te_3 including Pt NCs [15].

Mohanraman *et al.* reported that the nano structuring can greatly reduce lattice thermal conductivity (Fig. 2.13). The scattering of phonons occurs at nano precipitates and grain boundaries [16].

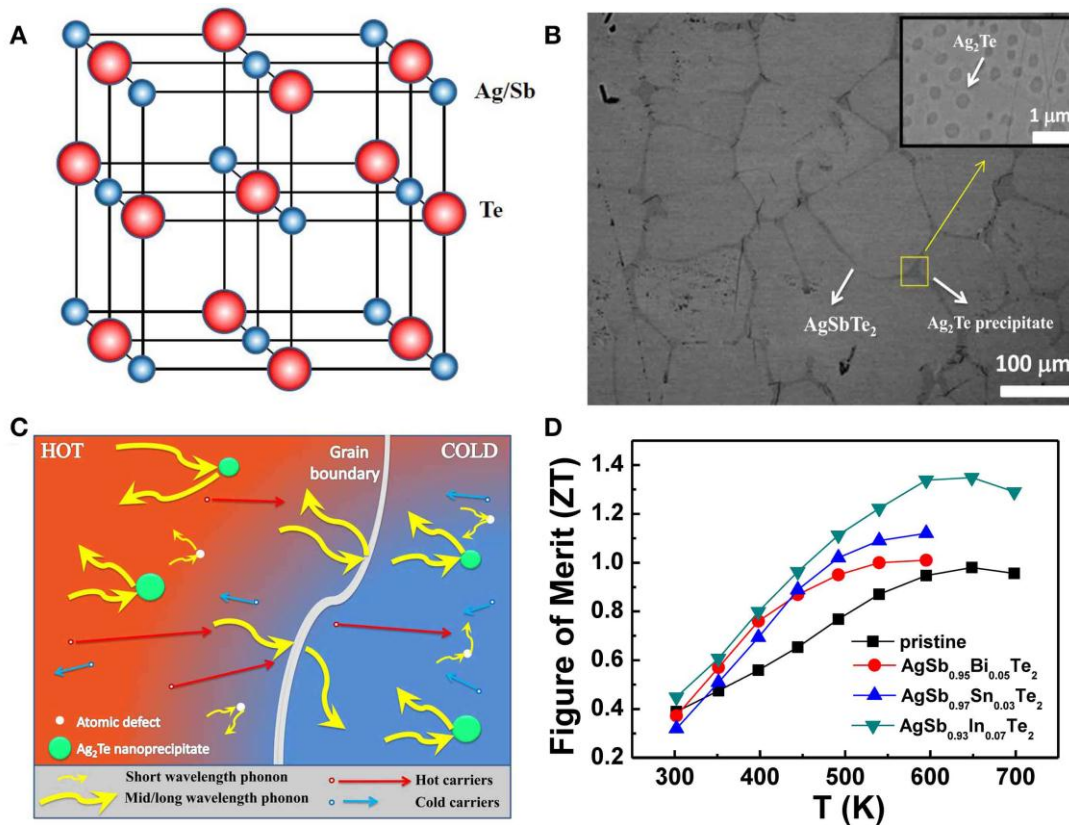


Figure 2.13 (a) Crystal structure, (b) SEM image, (c) schematic picture of phonon scattering, and (d) resulting ZT value [16].

Soni *et al.* found out similar effect of energy filtering at grain boundaries [17]. They studied the effect of sintering temperature on grain size, as the grain size was increased the effect of energy filtering on power factor was minimized. The results of sintering on grain size and TE properties are shown in Fig. 2.14.

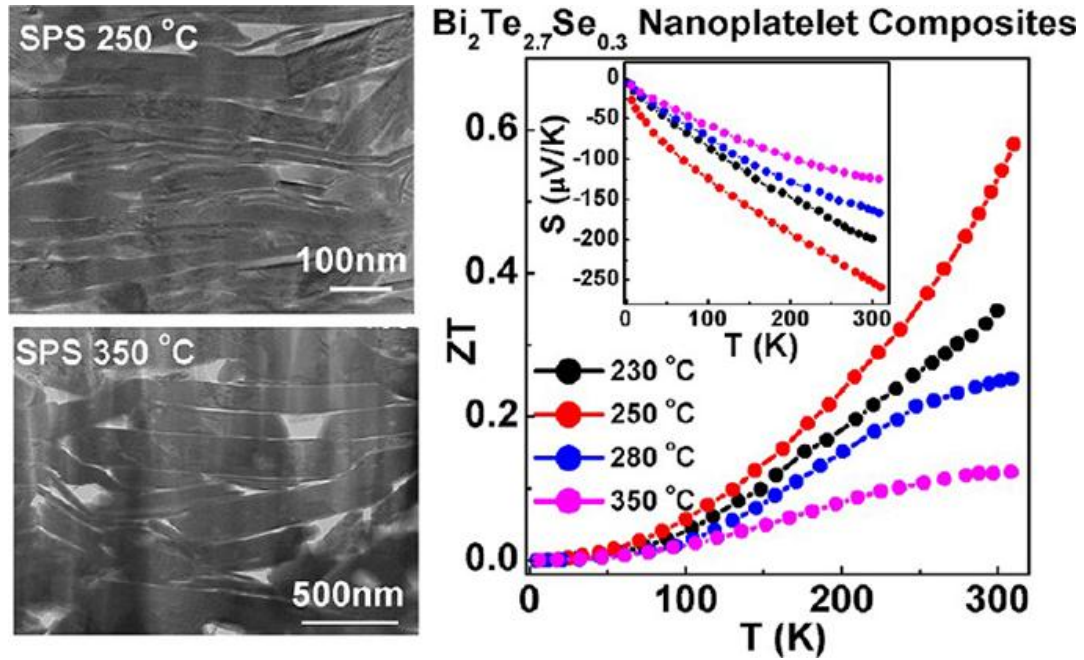


Figure 2.14 SEM images of the spark plasma sintered (SPS) Bi₂Te_{2.7}Se_{0.3} nano-platelet composite pellets [17].

As we derived the expression for $S(T)$ and $\sigma(T)$ from linear response theory, we wanted to understand this phenomenon in terms of electronic structure. Generally, the energy dependence of relaxation time is ignored, but if we purposefully introduce some energy dependence by increasing scattering probability for low energy carriers the $S(T)$ and $\sigma(T)$ would be modified. For example, if the scattering of carriers occurs below the chemical potential by introducing barrier by grains or inclusions, the negative contribution of Seebeck coefficient below the chemical potential can be reduced (W_1). Thus the numerator part of Seebeck is increased. The W_0 is also affected by the scattering and the reduction of carriers reduces the electrical conductivity. This means the denominator term for $S(T)$ is also reduced. So the carrier scattering

increases $S(T)$ and reduces $\sigma(T)$. If we substitute it in power factor term, the power factor increased as the $S(T)$ is a square term. These conditions are schematically illustrated in Fig. 2.15.

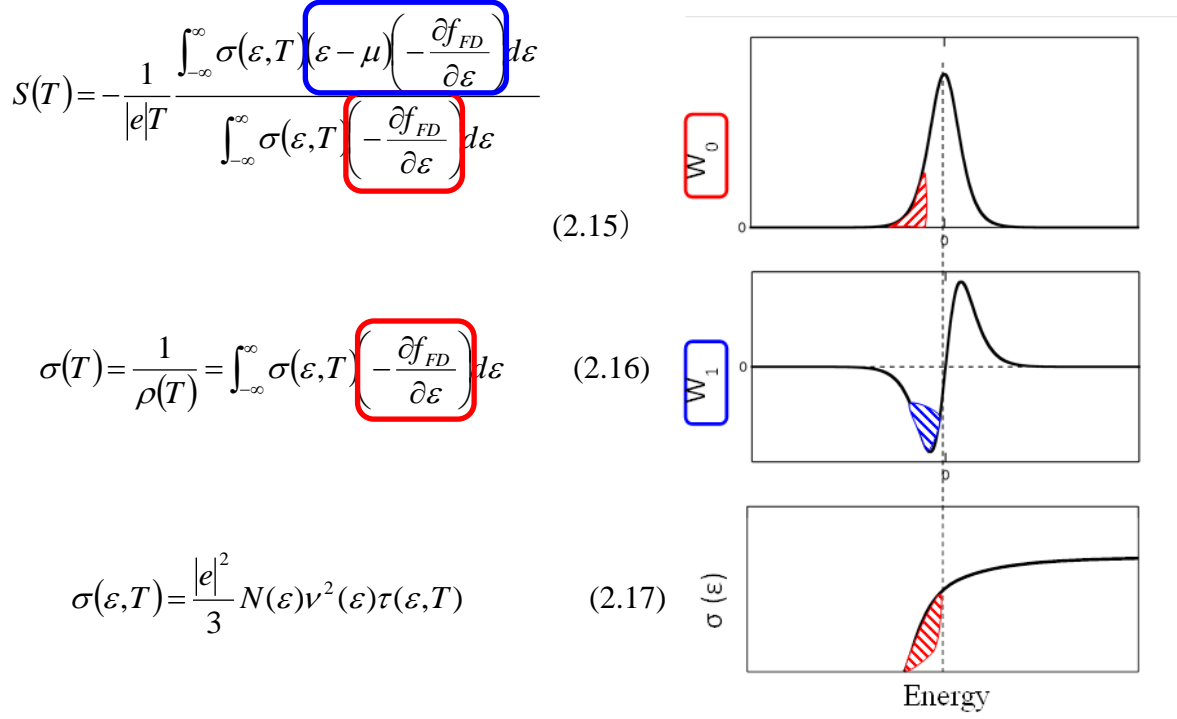


Figure 2.15 Energy dependence of W_0 , W_1 and spectral conductivity

HMS is also very good phase to know the energy dependent scattering of electrons in association with the precipitated secondary phase, because we can make the Si-precipitated HMS and MnSi-precipitated HMS easily. This condition is easily confirmed in the phase diagram shown in Fig. 6. The semiconducting Si particle would provide us energy dependent scatterings of electrons due to the different size of energy gaps between HMS and Si. MnSi, on the other hand, presumably produces a Schottky barrier at the boundary to make the strong energy dependence of electron scatterings. We considered that the effect of energy dependent scattering of conduction electrons should be revealed by employing the single phase HMS together with the HMS involving Si or MnSi nano-particles.

C. Partial substitution of heavy element, which is selected by first principle band calculations

It is reported that the partial substitution of heavy element Ta, W, Re for Mn in Al-Mn-Si C54 phase is effective way to enhance the ZT through the reduction of lattice thermal conductivity without greatly affecting electron transport properties (S, σ) [18,19]. The Al-Mn-Si C54-phase are belongs to the same NCL structure (HMS phase) and these structures have similarity in local atomic arrangement around Mn atoms. Therefore, Ta,W or Re substitution for Mn in HMS also would lead to enhance the ZT due to the reduction of lattice thermal conductivity without greatly affecting the electron transport properties.

2.5 Motivation and objectives

The motivation of my work is closely related with the energy crises or the energy need for the modern human society. The life of human being is strongly dependent on electrical energy which is derived from non-renewable fossil fuel. Considering the future we need to use these valuable resources more efficiently. Here, we are focusing on thermoelectricity to be the helping hand. We want to develop new materials which are cheap, environmental friendly and high performance. Though the goal seems difficult but we are aiming for it, with our guiding principles.

In this work we chose higher manganese silicide as a potential material. The objective is to enhance the thermoelectric performance by three different strategies, carrier tuning, heavy element substitution and energy filtering effect.

2.6 References

1. J.M. Ziman: Principles of the Theory of Solids, Cambridge University Press, New York, NY (1972).
2. T. Takeuchi, Mater. Trans. 50, 2359 (2009).
3. T. Takeuchi, A. Yamamoto, S. Ghodke: Mater.Trans. doi:10.2320/materials.MF201610
4. P. G. Klemens, Proc. R. Soc. London, Ser. A **68**, 1113 (1955).
5. A. F. Ioffe: Semiconductor Thermoelements and Thermoelectric Cooling, (Infosearch Limited, London, 1957).
6. A. B. Gokahale and G. J. Abbaschian, Binary Alloy Phase Diagrams, pp. 2603 (1990).
7. P. Norouzzadeh, Z. Zamanipour, J.S. Krasinski, D. Vashaee, J. Appl. Phys. 112 (2012) 124308.
8. O.G. Karpinskii, B.A. Evseev, Izv. Akad. Nauk SSSR, Neorg. Mater. 5 (1969) 525.
9. O. Shwomma, A. Preisinger, H. Nowotny, A. Wittman, Monatsh. Chem. 95 (1964)1527.
10. H.W. Knott, M.H. Mueller, L. Heaton, Acta Crystallogr. 23 (1967) 549.
11. A. Yamamoto, K. Kitahara, H. Miyazaki, M. Inukai, T. Takeuchi, Proceedings of *11th International Conference on Ceramic Materials and Components for Energy and Environmental Applications*, American ceramic society, 14-20 June 2015.
12. Y. Miyazaki, Y. Saito, K. Hayashi, K. Yubuta, and T. Kajitani, Jpn. J. Appl. Phys. 50, 035804 (2011).
13. G. Jeffrey Snyder and Eric S. Toberer, Nature Materials **7** (2008) 105-114.
14. Yichi Zhang and Galen D. Stucky, Chemistry of Materials **26** (2014) 837-848.
15. Dong-Kyun Ko, Yijin Kang and Christopher B. Murray, Nano Letters **11** (2011) 2841-2844.
16. R. Mohanraman, Tian-Wey Lan Te-Chih Hsiung Dedi Amada, Ping-Chung Lee, Min-Nan Ou and Yand-Yuan Chen, Frontier in Chemistry **3** (2015) 63.
17. Ajay Soni, Yiqiang shen, Ming Yin, Yanyuan Zhao, Ligen Yu, Xiao Hu, Zhill Dong, Khaim Alk Knor, Mildred S. Dresselhaus and Qihua Xiong, Nano Lett. **12** (2012) 4305-4310.

18. A. Yamamoto, H. Miyazaki, and T. Takeuchi: *J. Appl. Phys.* **115**, 23708 (2014).
19. A. Yamamoto, H. Miyazaki, M. Inukai, Y. Nishino, and T. Takeuchi: *Jpn. J. Appl. Phys.*, **54**, 071801 (2015).
20. L. M. Levinson, *J. Solid State Chem.* **1973**, *6*, 126–135.
21. W. B. Bienert, F. M. Gillen, Process of making MnSi thermoelectric element and product of said process. U. S. Patent No. 3407037, **1968**.
22. A. J. Zhou, T. J. Zhu, X. B. Zhao, S. H. Yang, T. Dasgupta, C. Stiewe, R. Hassdorf, E. Mueller, *J. Electron. Mater.* **2010**, *39*, 2002–2007.
23. X. Chen, A. Weathers, D. Salta, L. Zhang, J. Zhou, J. Goodenough, L. Shi, *J. Appl. Phys.* **2013**, *114*, 173705.
24. W. Luo, H. Li, F. Fu, W. Hao, X. Tang, *J. Electron. Mater.* **2011**, *40*, 1233–1237.
25. S. Barczak, R. A. Downie, S. R. Popuri, R. Decourt, M. Pollet, J. W. G. Bos, *J. Solid State Chem.* **2015**, *227*, 55–59.
26. M. Ohtaki. *Journal of the Ceramic Society of Japan* 119, no. 1395 (**2011**): 770-775.

Chapter 3

Experimental Details

The work of this project is focused on synthesis and characterization of higher manganese silicide (HMS) based compounds for thermoelectric application. In this work we have prepared samples with different grain size to understand the effect of grain boundary density on transport properties. Furthermore, we employed Fe/ Cr substitution for Mn to obtain optimal carrier concentrations and W/ Re substitution for Mn to reduce the lattice thermal conductivity. The synthesis technique for each series of samples was modified according to the requirements. Those detailed experimental parameters are reported in each chapter separately.

This chapter is dedicated to elaborate working procedure of each experimental technique used for synthesis and characterization. The list of synthesis techniques and characterization methods are following.

Table 3.1: Each procedure of synthesis and evaluation

Synthesis techniques	Characterization and physical property measurement
Induction melting	X-Ray diffraction
Arc melting	Scanning electron microscope
Liquid quenching	Seebeck coefficient (Steady state method)
Spark plasma sintering	Resistivity (4 probe method)
	Thermal conductivity (Laser flash method)
	Specific heat (DSC)
	Density (Archimedes method)

Broadly, we synthesized samples in two different methods depending on the objective. First, the flow chart shown in Fig. 3.1 is for the non-doped HMS samples and the flow chart of Fig. 3.10 is for the samples with doping of Re/W/Cr/Fe.

3.1 Synthesize of non-doped MnSi_y .

It was reported that HMS alloy can be synthesized by high energy ball milling, arc melting, induction melting and also single crystal by Bridgmann method. In this study, we choose induction melting to prepare polycrystalline HMS samples because of two reasons. 1) In arc melting the control over composition is difficult, as the Mn have high vapor pressure; it can get evaporated due to very high temperature generated in plasma. 2) The ball milling has been associated with the contamination problem so the formation of HMS without impurity would be a tedious work. The best option we found was induction melting, where heating can be controlled manually to avoid evaporation of Mn. Thus the composition can be effectively controlled in induction furnace. Chapter 4 is dedicated to the samples prepared by induction melting, where series of compounds were prepared by changing Silicon concentration.

3.1.1 Flow chart for synthesis: non-doped MnSi_y

Each step mentioned in the flow chart (Fig. 3.1) was elaborated below.

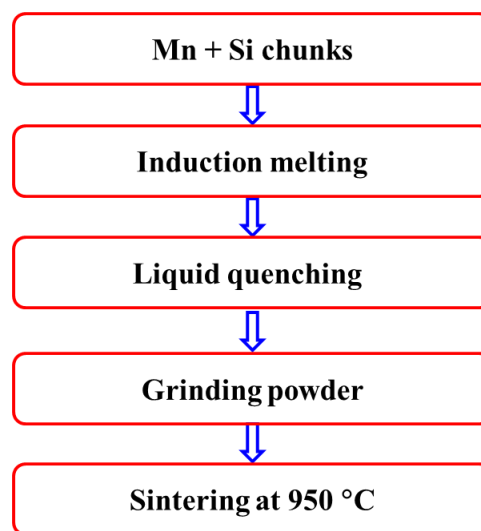


Figure 3.1 Flow chart for synthesis of MnSi_y

I. Weighing

To maintain the stoichiometric ratio is very important. Thus, the Mn (99.99%) and Si (99.99%) chunks of few millimeter sizes were weighted precisely according to the composition.

II. Induction melting

The induction melting process started with placing pieces of high purity elements in boron nitride (BN) crucible. The crucible was then kept inside the chamber, at the center of Cu coil. Argon gas was used for chamber flushing and making inert atmosphere after evacuation. The Cu- coil was made of a hollow tube so that cooling water flowed inside it. When an alternating high current was passed through coils, eddy current was generated in the sample pieces. The generated eddy current increased the temperature of sample with joule heating. The elements with low melting point were kept at the bottom of the crucible to avoid the loss by evaporation. The applied current was controlled manually by a knob. The sample was heated slowly till all the pieces melts and the molten state was maintained for a few minutes for homogeneous mixing. The molten liquid generally rotates due to eddy current, which helps in mixing the sample properly. The factors such as resistivity of element and size of pieces are very critical for sample preparation with induction melting. The schematic of induction furnace is shown in Fig. 3.2 and the typical ingot prepared is shown in Fig. 3.3.

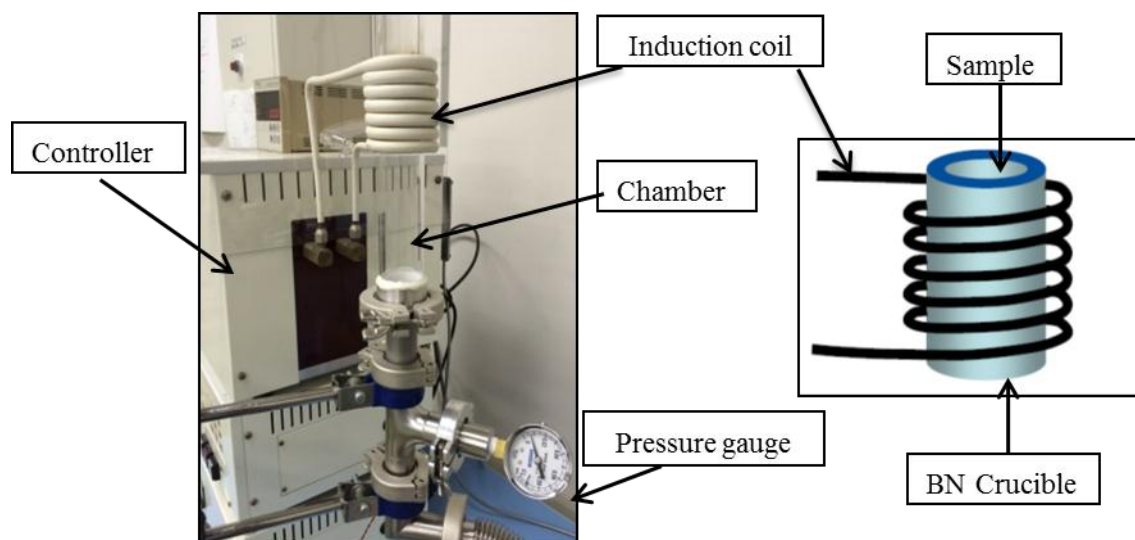


Fig. 3.2 Image of induction furnace



Figure 3.3 Typical ingot from induction melting

III. Liquid quenching

The liquid quenching (LQ) method was used to rapidly solidify the sample from molten state into ribbons. The schematic diagram of the liquid quenching is shown in Fig. 3.4. The molten sample was injected on the copper wheel, where high thermal conductivity of Cu and the high speed rotation generates a cooling effect of 10^5 K/sec. Ribbon like samples were obtained with very fine polycrystalline microstructure.

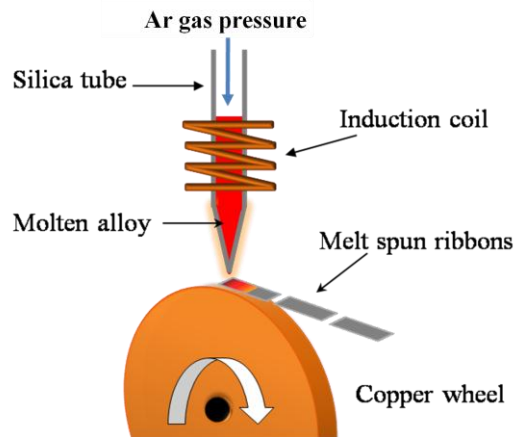
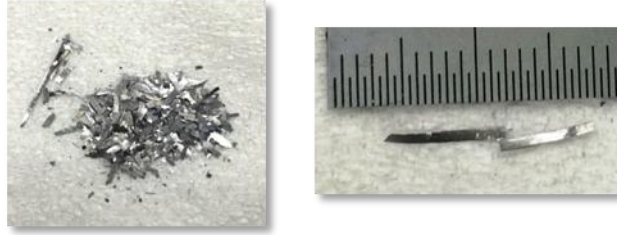


Figure 3.4 Schematic diagram of liquid quenching/melt spinning

The main purpose of using this technique was to refine the microstructure and to obtain higher solubility for the dopant elements.

The preparation started with sizing the arc melted/ induction melted ingot to fit inside a quartz tube of 8 mm (inner diameter), that was prepared from opaque quartz with a glass nozzle having an outer diameter of 10 mm. The nozzle was set in the center of induction coil, with injection distance of 0.4 mm between nozzle orifice and copper wheel ($\phi 200$ mm). The chamber was evacuated to about 9.0×10^{-5} Torr and Ar gas inert atmosphere was created with operating pressure of about 680 mmHg. The molten sample was injected on copper wheel, which is rotating at 4500 rpm by passing pressurized Ar gas inside nozzle. The obtained ribbon samples were used for characterization. The ground ribbons were used for making bulk samples.



Length: **10~15 mm**, Width: **0.5~1mm**, Thickness: **10~15 μ m**

Figure 3.5 Liquid quenched ribbon samples with dimensions

IV. Spark Plasma Sintering:

Spark Plasma Sintering (SPS) is a thermal treatment for densification of a solid structure via mass transport process at atomic scale inside the particles. In the sintering process, powder sample was kept inside the hollow graphite die and punch, as shown in Fig. 3.6. The sample was also surrounded by carbon sheet, to avoid reaction with die and punch. The sample was heated up to 800 °C at 50 °C/min rate and then up to 950 °C with 25 °C/min rate, maintained for a few minutes and then slowly cooled down to room temperature (Fig. 3.7).

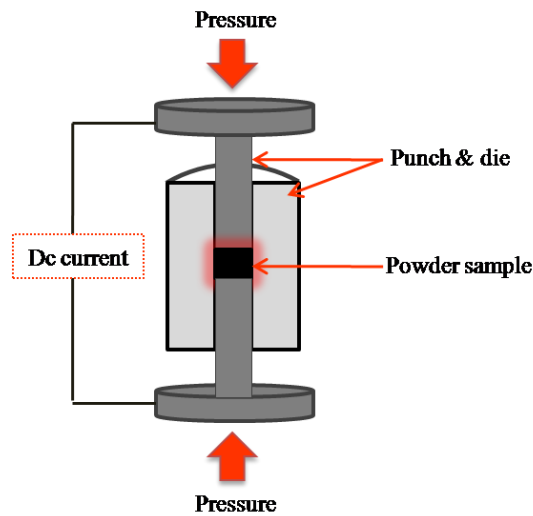


Figure 3.6 Systematic representation of stages in SPS process

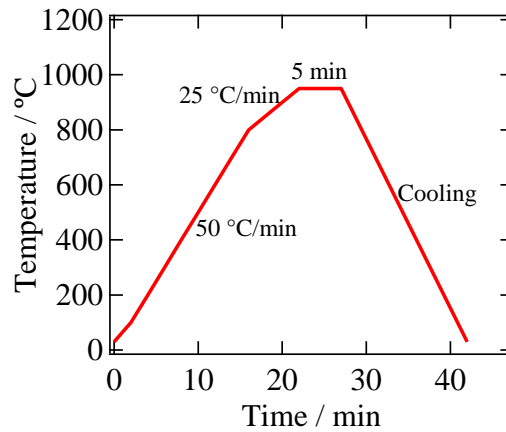


Figure 3.7 Schematic representing of the SPS cycle

Figure 3.8 shows the steps involved in sintering process. Here, the plasma and joule heating accelerates the densification by reduction in surface energy, where the reduction in surface energy act as driving force to diffuse the particles and densify the pellet. The porosity decreases as the loose powder particle start to react and inter diffuse into each other. Thus the neck formation signifies strengthening of the material, and at final stage there are minimal pores with maximum density. In the final stage of sintering grain growth occurs with rapid grain boundaries migration. The rate of particle bonding during sintering depends on temperature, materials, particle size and several processing factors.

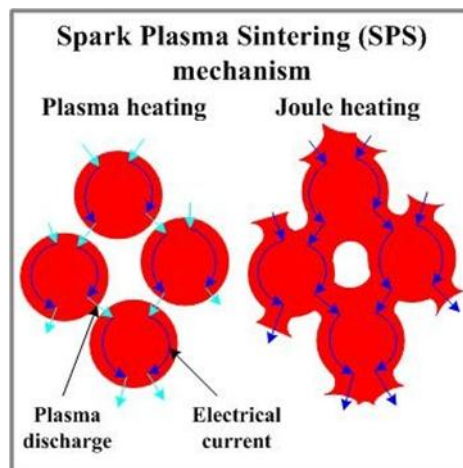


Figure 3.8 Mechanism of spark plasma sintering (www.substech.com)

V. Density measurement : Archimedes method

The sample densities were measured by following method:

First, accurate volume was estimated by the Archimedes' principle with measuring weight in ethanol (M_0) and out of ethanol (M). The difference in weights corresponds to the buoyant force. So with the known density of ethanol ($\rho_{ethanol}$), one can obtain the volume displaced fluid V_{Liquid} , which is equal to the volume of sample V_{Sample} .

$$M - M_0 = V_{Sample} * \rho_{ethanol} \quad 3.1$$

From estimated sample volume and measured weight, one can calculate the density of the sample,

$$\rho_{Sample} = M/V_{Sample} \quad 3.2$$

The schematic diagram shown in Fig. 3.9 illustrates the working principle of an Archimedes method.

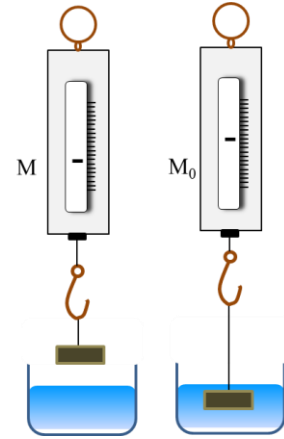


Figure 3.7: Schematic diagram of Archimedes method

3.1.2 Flow chart for synthesis: Substitution of Cr/Fe/W/Re

The synthesis of partially substituted HMS was slightly different. For example, samples were prepared by using arc melting instead of induction melting. There are two reasons for the change: (1) the large temperature difference in melting points of constituent elements can make inhomogeneous mixture by performing induction melting, (2) the precursor elements were in powder compared to the chunks of elements which can not be melted by induction melting. Here only the preparation of ingot is different and the other processes are same as mentioned in section 3.1.1.

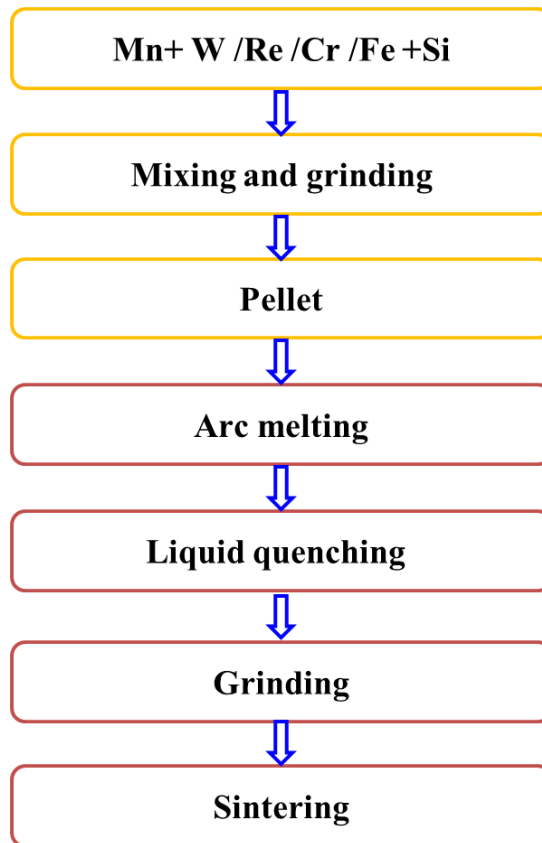


Figure 3.10 Flow chart for synthesis of doped MnSi_y

1. Cold isostatic press

The each weighted elements were grinded into powders using an alumina mortar and a pestle. Cold isostatic press was performed on the powders using punches and die, which are made of hardened stainless steel. The pellets were obtained by applying pressure on punch up to 200 MPa.

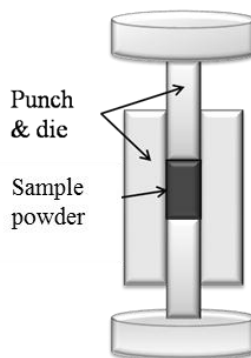


Figure 3.11 Schematic diagram of cold isostatic press

I. Arc melting

In this method electric arc was used to heat the sample of high melting point. The maximum temperature can reach above 3000 °C. The arc melting apparatus is shown in Fig. 3.12. The water cooled copper hearth had 3 cavities for keeping weighted samples. This method was used for cast melting, powder melting, or making alloys. The process is carried out in pressurized Argon atmosphere (680 mmHg).

First the titanium bead was melted to absorb residual oxygen to avoid oxidation. To get homogeneous mixture sample was melted several times by flipping it with a tungsten rod. In this arc melting process temperature increased instantaneously, so we needed to carefully increase the current. We used it for melting the samples with W or Re where the constituent elements have a very high melting point.

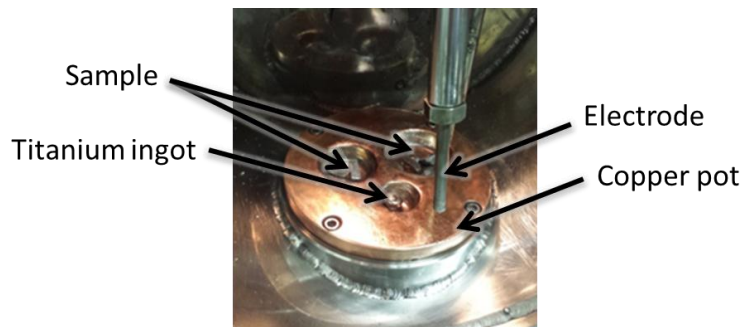


Figure 3.12: Image of arc melting furnace

3.2 Characterization techniques

The synthesized materials described above were characterized by various experimental techniques at different measurement conditions to study its structural and functional properties. The fundamental of characterization techniques used was explained with an example of prepared sample. Various characterization techniques were used depending on the sample, so systematically characterization of ribbon sample and sintered samples were described below. The structural characterization was done by X-Ray diffraction, morphological by scanning electron microscopy, elemental analysis by energy dispersive x-ray (EDX) and the thermoelectric properties measurement (S, κ, ρ) by respective methods are discussed in this section.

3.2.1 X-ray diffraction (BRUKER D8 Advance)

X-ray diffraction (XRD) is characterization technique which gives the details of atomic arrangements, crystal structure of the material. The X-rays of wavelength (λ) 1.5406 Å are incident on the material while the detector collects the constructive interference pattern of diffracted rays coming from the plane which satisfies the Bragg's condition,

$$2d \sin \theta = n\lambda \quad 3.3$$

Where n is the order of diffraction, d is the interplanar distance of crystal and θ is the angle of incidence. The XRD scan was done at room temperature from $20^\circ \leq 2\theta \leq 80^\circ$.

The XRD patterns were obtained for following sample to verify and study the phase formed in the material after the reactions.

1. Ingot samples after arc melting/ induction melting
2. Crushed LQ ribbon samples
3. Sintered pellet samples
4. Powders after thermal analysis

3.2.2 SEM-EDX (Hitachi SU6600)

The microstructure by scanning electron microscope (SEM) and energy dispersive x-ray spectroscopy (EDX) was analyzed by Hitachi 6600. High resolution micrographs were obtained for liquid quenched and sintered samples. The micrographs were used to study the morphology and the crystal structure of the material.

Secondary electrons and backscattered electrons were used for imaging samples. Secondary electrons gave the morphology and topography of samples and backscattered electron illustrate the contrasts in composition in multiphase samples. The elemental analysis by EDX was done to obtain sample composition.

3.2.3 Seebeck measurement (Micro-miniature refrigerator (MMR) technologies Inc.)

Seebeck coefficient was measured by steady state method. The image of apparatus and the sample mounting are shown in Fig. 3.13. On the mounting stage, the constantan wire as reference on left side and the measuring sample on right side were symmetrically arranged and set by using silver paste. The silver paste was used to obtain good thermal and electrical connection. The stage was mounted on a Joule Thompson module and the chamber was evacuated to avoid additional heat flow. To obtain a temperature gradient, high pressure (12 MPa) Nitrogen gas flows through the Joule-Thompson module. To current was applied to the heater. Seebeck coefficient was measured from 300 to 700 K.

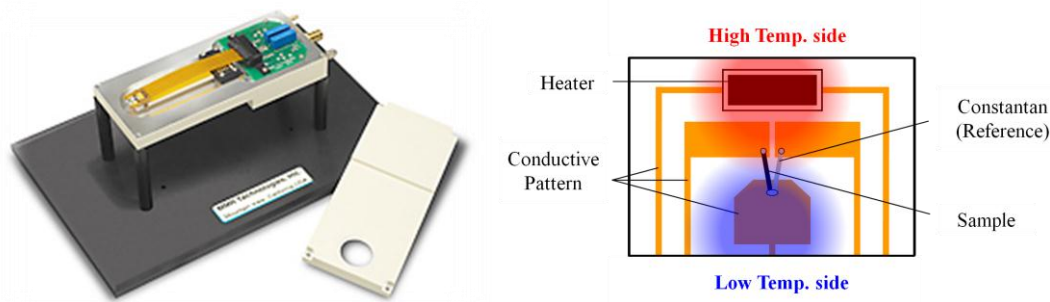


Figure 3.13 Image of Seebeck measurement systems (left), and the sample mounting (right).

The working principle of this instrument can be described briefly as follows. The temperature difference between two edges of sample with and without using the heater are $\Delta T(P)$, $\Delta T(0)$, respectively. Similarly, the voltage of the two edges with and without the heating are V_{Heat} and V_0 . The obtained voltage contains voltage from Seebeck effect and offset voltage, here V_0 is produced by the apparatus.

$$V(P) = -S\Delta T(P) + V_0 \quad 3.4$$

$$V(0) = V_0, \quad 3.5$$

by subtracting two equations,

$$V(P) - V(0) = -S(\Delta T(P) - \Delta T(0)) \quad 3.6$$

We can write two equations using Seebeck coefficient for reference and sample as,

$$V_{s_{amp,print}}(P) - V_{s_{amp,print}}(0) = -S_{s_{amp,print}}(\Delta T(P) - \Delta T(0)) \quad 3.7$$

$$V_{r_{ef,print}}(P) - V_{r_{ef,print}}(0) = -S_{r_{ef,print}}(\Delta T(P) - \Delta T(0)) \quad 3.8$$

Here, the subscript “*print*” means the additional properties of wiring material printed on the ceramic stage. The simultaneous solution of (3.7) and (3.8), is:

$$S_{s_{amp,print}} = S_{r_{ef,print}} \frac{V_{s_{amp,print}}(P) - V_{s_{amp,print}}(0)}{V_{r_{ef,print}}(P) - V_{r_{ef,print}}(0)} \quad 3.9$$

The obtained $S_{s_{amp,print}}$ is assumed to be the sum of $S_{s_{ample}}$ and $S_{p_{rint}}$. Using known value of $S_{p_{rint}}$, $S_{s_{ample}}$ was obtained.

$$S_{s_{amp,print}} = S_{s_{ample}} + S_{p_{rint}} \quad 3.10$$

The $S_{p_{rint}}$ is known value for a standard apparatus and it deducted before showing $S_{s_{ample}}$ value.

3.2.4 Resistivity measurement (4-probe method)

The resistance of the sample was calculated from voltage vs current plot (V-I plot). The room temperature resistivity for a rectangular shape, with a cross section of sample S , and distance between the voltage probes l , was calculated by Eq. 3.11

$$\rho = \frac{RS}{l} \quad 3.11$$

Temperature dependence of electrical resistivity was measured in range 300 K to 1000 K. In high temperature measurement system, Ni wire was used for making electrical connections, as it has a good oxidation resistance. The measurement was done using a hand-made 4-probes system under vacuum atmosphere inside a tubular furnace. A schematic diagram of the four-probe constructed on a ceramic plate is shown in Fig. 3.14.

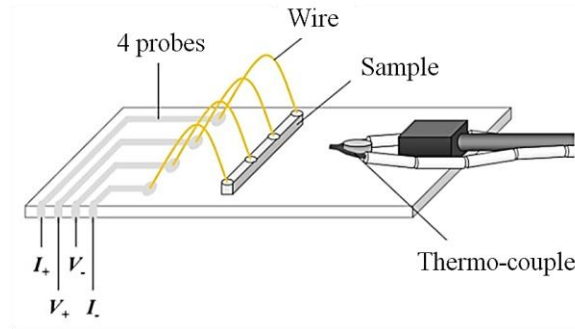


Fig. 3.14: Schematic diagram of four probe measurement

3.2.5 Thermal conductivity measurement (laser flash)

The thermal diffusivities α were measured by a laser flash method. The heat capacities of samples C_p were estimated from reference sample (Alumina powder). Using the measured α , sample density ρ and estimated C_p , thermal conductivities κ were calculated.

$$\kappa = C_p \rho \alpha \quad 3.12$$

The sample surface is irradiated by a shot of laser pulse and high energy pulse is absorbed by the sample with thickness d , and the time required for heat to reach the rear surface is noted with the rise in temperature on the rear surface as detected by detectors. The following expression is used to calculate the diffusivity:

$$\alpha = \frac{1.38}{\pi^2} \times \frac{d^2}{t_{1/2}} \quad 3.13$$

$t_{1/2}$ is the time for the temperature to reach half of the maximum value on rear surface.

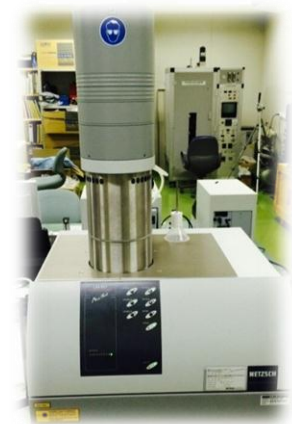


Figure 3.15 NETZSCH-LFA457

3.2.6 Differential thermal analysis (Thermo plus EVO2 TG-8121)

Differential thermal analysis (DTA) was used to understand the thermal stability of the materials. The working principle is based on the temperature difference ΔT between reference (**R**) and the sample (**S**). As shown in Fig. 3.16, thermocouples are connected to reference and sample and the signals are detected by a voltmeter.

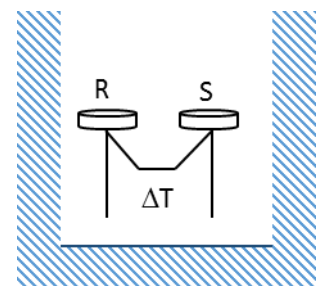


Figure 3.16 Schematic diagram of DTA

As the temperature increases the voltmeter shows a deflection if there is a phase change in sample. The deflection is related to exothermic or endothermic reaction, which is latent heat of material required for a phase change. We used DTA to investigate the decomposition temperature of manganese silicide liquid quenched samples containing small amount of W/Re/Cr/Fe. The DTA was performed at the temperature range from 300 K to 1200 K with Al_2O_3 as reference material. The sample was heated at a rate of $7^\circ\text{C}/\text{min}$.

Chapter 4

Thermoelectric properties of higher manganese silicide containing small amount of MnSi/Si nano-particles

4.1 Introduction

In this study, we prepared higher manganese silicides (HMS) containing small amount of MnSi or silicon nano-particles to study the energy dependent scattering effect, which had been reported to improve the thermoelectric power factor. HMS is one of the best phase for this purpose because we can prepare Si precipitated HMS and MnSi precipitated HMS when the composition of samples were located at slightly Si deficient and Si excess compositions, respectively (Fig. 4.1). Note here that Si particles and MnSi particles precipitated in HMS are semiconducting and metallic, respectively. Here, we have also investigated the effect of grain boundary by employing liquid quenching technique, which enabled us to obtain fine grain samples.

4.2 Experimental procedure:

Higher manganese silicide MnSi_γ with different composition $\gamma = 1.67, 1.73, 1.79, 1.81,$ and 2.11 were synthesized by the induction furnace. The ingot was further used for melt spinning/liquid quenching. The ribbon-shaped samples with 10~15 mm in length, 0.5~0.1 mm in width, and 10~15 μm in thickness were obtained. Then the ribbon sample was grounded by a mortar and pestle, the obtained powder was sintered in graphite die ($\phi=10$ mm) by spark plasma sintering under a pressure of 60 MPa at 950 °C for 5 min in vacuum.

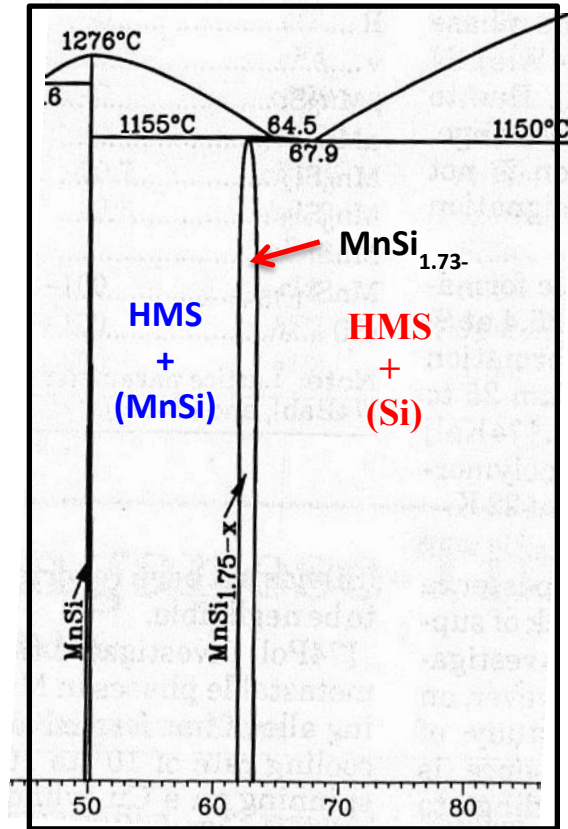


Figure 4.1 Binary phase diagram of Mn-Si [1]

We prepared two types of samples for characterization; liquid quenched ribbons and bulk-sintered samples. The phase purity of the compounds was identified by powder X-ray diffractometer of BRUKER D8 advance with Cu-K α radiation. The microstructure was observed by Hitachi SU6600 scanning electron microscope (SEM). Seebeck coefficient was measured by a steady state method using Seebeck measurement system manufactured by MMR technologies. Electrical resistivity was measured by a conventional four-probe method. Thermal conductivity was calculated by the formula $\kappa = D\rho C_p$. Thermal diffusivity (D) was measured by laser flash technique (LFA457, NETZSCH), and the density (ρ) of sintered samples was measured by an Archimedes method.\

4.3 Results

The XRD pattern of $\text{MnSi}_{1.73}$ plotted in Fig. 4.2 clearly showed the formation of phase pure HMS, without the precipitation of any impurity phase. A small peak of MnSi was observed in the $\text{MnSi}_{1.67}$ sample. Samples containing silicon above the nominal composition showed small peaks of silicon, which was precipitated during the liquid quenching process. The intensity of peak for silicon increases with γ ($1.79 \leq \gamma \leq 2.11$), without forming any other impurity phases.

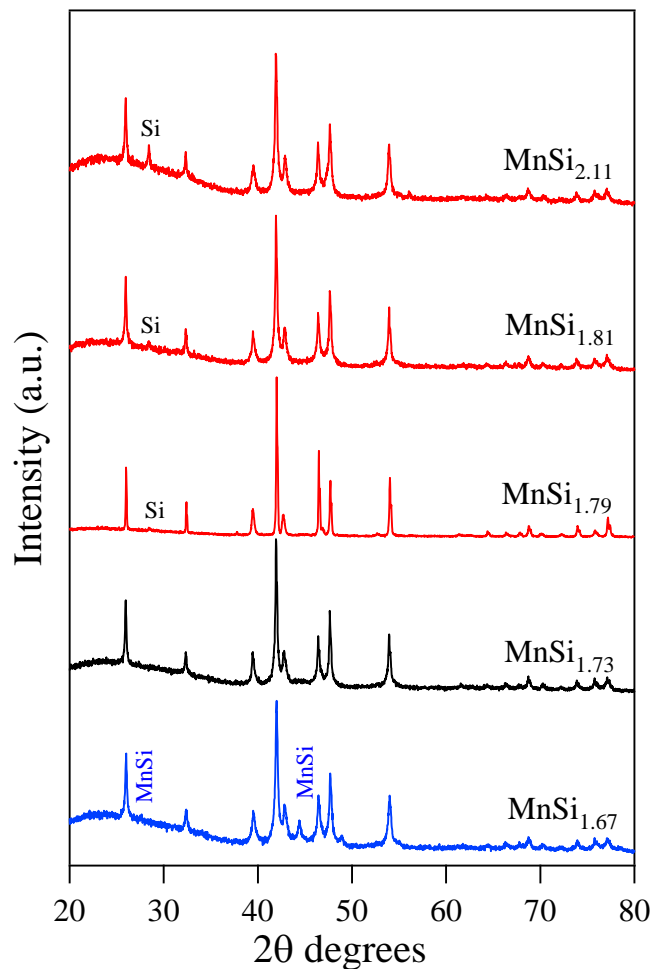


Figure 4.2 XRD data plotted for MnSi_γ with different composition $\gamma = 1.67, 1.73, 1.79, 1.81,$ and 2.11 .

To investigate the particle size, grain size, and the distribution of secondary phases, we took SEM images, which were shown in Fig. 4.3. In Figs. 4.3 (a) - (c), grains of 2 - 3 μm are observed for the liquid quenched samples with $\gamma = 1.67, \gamma = 1.73,$ and $\gamma = 1.79$. Figure 3(d) - (f) shows the dense microstructures of bulk samples. The grain boundaries are highly

diffused after spark plasma sintering process. By comparing (a) and (d) for the composition of $\gamma = 1.67$, we can clearly confirm the effect of processing on microstructure. The density of grain boundaries was definitely reduced to a large extent in SPS samples, though both the samples show nano-size precipitates of MnSi. A similar effect can be seen throughout the whole composition range.

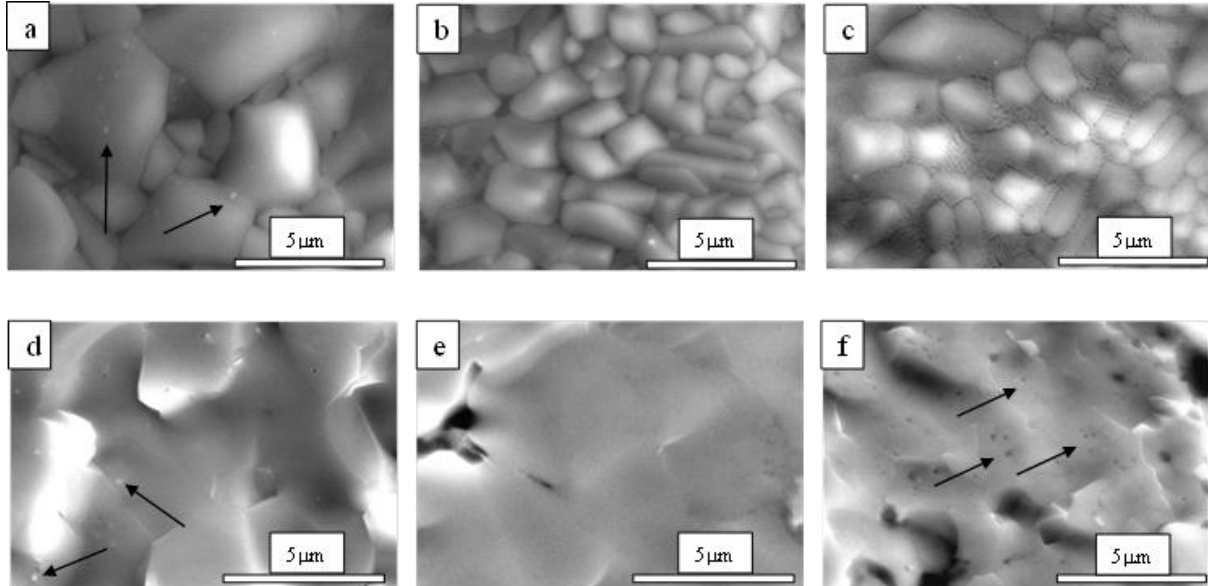


Figure 4.3 SEM images: (a), (b), and (c) show microstructure of liquid quenched samples of $\gamma=1.67$, 1.73, and 1.81, respectively. (d), (e) and (f) show microstructure of SPS samples $\gamma=1.67$, 1.73, and 1.81, respectively

The microstructure of LQ and SPS samples at $\gamma = 1.73$ showed no impurity phases. This fact is consistent with the XRD data. Figure 4.3 (c) and (f) for Si-rich composition ($\gamma = 1.81$) show difference in grain boundary density, as for other composition samples. Nano precipitates in black color were observed in the gray colored matrix of $\gamma = 1.81$ SPS sample shown in (f), which could be silicon nano-particles, as small peak of Si was observed in XRD data. A similar microstructural behaviour for Si-rich compositions were also observed for $\gamma = 1.79$ and $\gamma = 2.11$ samples.

The Seebeck coefficient at 300 K is plotted as a function of composition in Fig. 4.4. The sign of Seebeck coefficient was positive regardless of the compositions, indicating that the present samples are p-type thermoelectric materials. It was clearly observed that the absolute value of Seebeck coefficient for the LQ samples was definitely larger than that of the SPS samples. The Seebeck coefficient is almost constant within the error bars over compositions for liquid quenched or SPS samples.

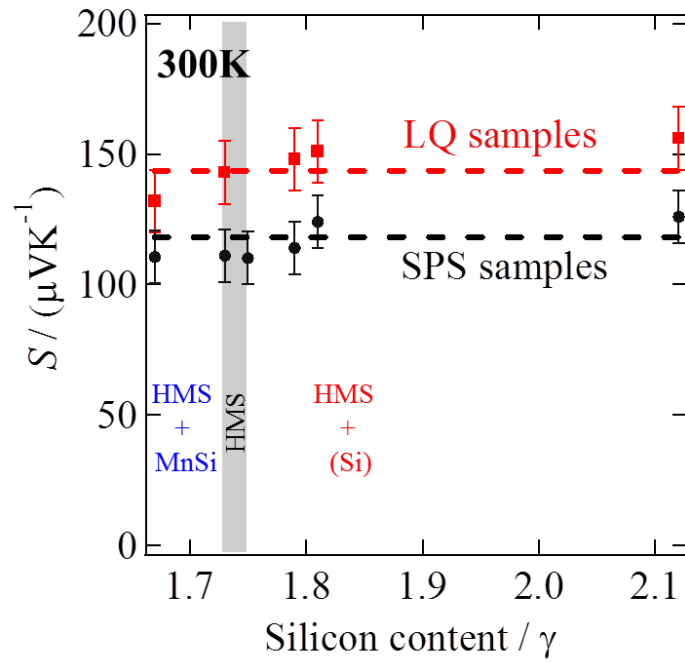


Figure 4.4 The composition dependence of Seebeck coefficient for LQ and SPS (MnSi_γ) samples at room temperature.

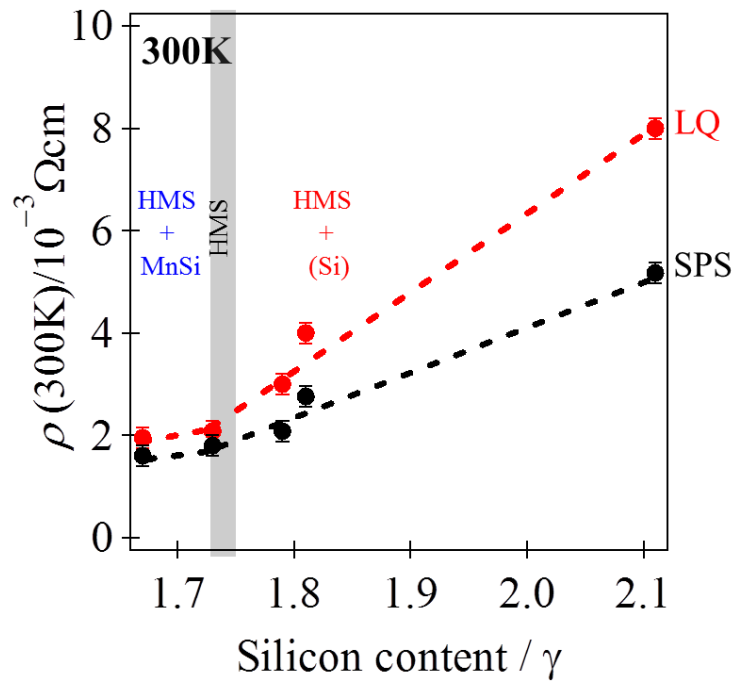


Figure 4.5 The composition dependence of electrical resistivity for LQ and SPS (MnSi_γ) samples at room temperature.

Figure 4.5 shows the composition dependence of electrical resistivity at 300 K. The resistivity of $\gamma = 1.67$ sample was the lowest which might be due to the presence of metallic MnSi as impurity phase in the matrix. The sample with Si-rich composition showed an increase in electrical resistivity with increasing silicon concentration because of the increasing amount of precipitated silicon nano-particles. Similar to the behaviours in Seebeck effect, here we observed small but finite process dependent difference in LQ sample and SPS sample in absolute electrical resistivity for a composition. The LQ samples always showed slightly higher electrical resistivity than that of SPS samples. This experimental fact is presumably brought about by the enhanced scattering effect of grain boundary because the former has much dense grain boundary than the latter.

The composition dependence of power factor ($S^2\sigma$) is shown in Fig. 4.6. The power factor showed ~20 % difference between LQ & SPS samples. The power factor is large for all the LQ samples, which is due to dominant contribution of Seebeck coefficient. The power factor is large for the nominal composition ($\text{MnSi}_{1.73}$) HMS, and it is reduced by the presence of MnSi or Si as a secondary phase in the matrix.

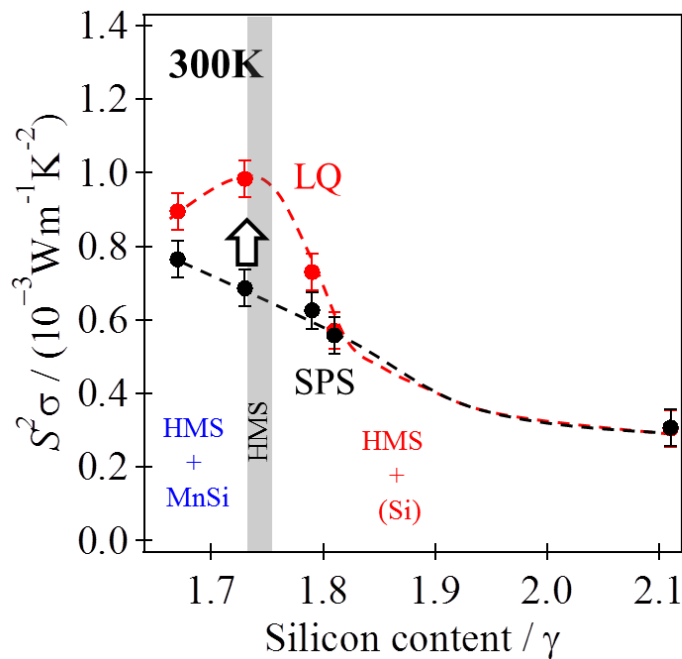


Figure 4.6 The composition dependence of power factor for LQ and SPS (MnSi_γ) samples at room temperature.

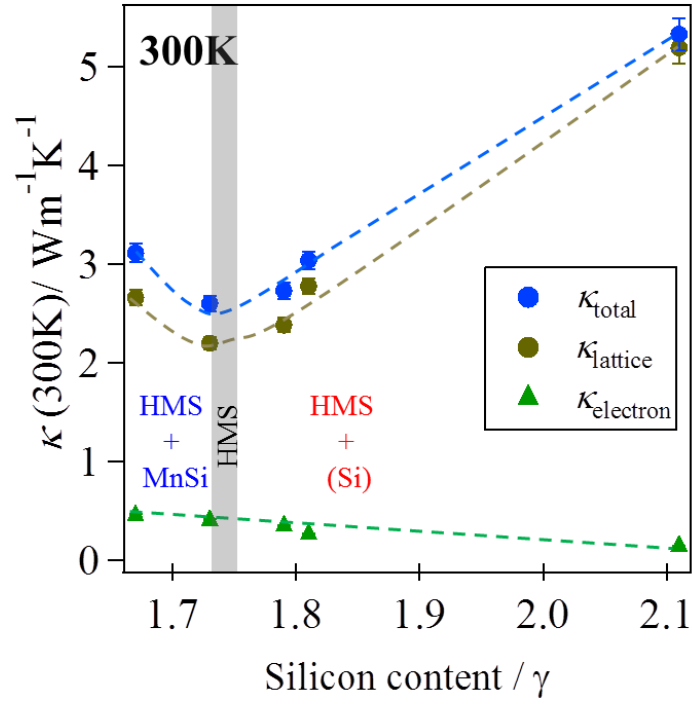


Figure 4.7 The composition dependence of measured κ_{total} , with estimated $\kappa_{lattice}$, and $\kappa_{electron}$ for $(MnSi_\gamma)$ SPS samples

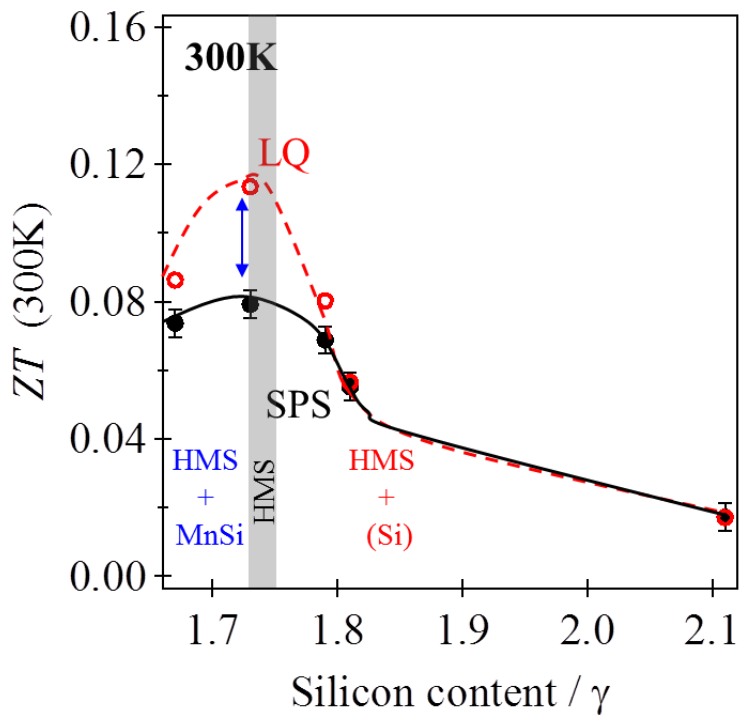


Figure 4.8: The composition dependence of ZT for $MnSi_\gamma$ at room temperature.

The thermal conductivities of the liquid quenched ribbon samples were not measured due to the experimental limitation. The composition dependence of the thermal conductivity for SPS samples is shown in Fig. 4.7. The results suggested that the addition of secondary phases MnSi/Si particles could increase the thermal conductivity. In the case of $\gamma = 1.67$ sample, both the contribution due to lattice and electron was definitely increased, whereas the thermal conductivity of Si-rich samples $\gamma = 1.79$ or $\gamma = 1.81$ was enhanced solely by lattice thermal conductivity and the electronic contribution was reduced as compared to $\gamma = 1.73$ of pure HMS. The increased thermal conductivities with secondary phases was clearly by the inherent contribution of MnSi ($10 \text{ Wm}^{-1}\text{K}^{-1}$) and Si ($149 \text{ Wm}^{-1}\text{K}^{-1}$) to the matrix phase.

The composition dependence of ZT at 300 K is plotted in Fig. 4.8. By assuming the same thermal conductivity values of the SPS samples, we calculated the ZT even for the liquid quenched samples. The maximum ZT at room temperature was observed for MnSi_{1.73} SPS sample that has no precipitation of secondary phase. The ZT of MnSi_{1.67} was reduced due to the large thermal conductivity of precipitated MnSi. The large electrical resistivity of precipitated silicon nano-particles also reduced ZT of MnSi_{1.79}/MnSi_{1.81} samples.

4.4 Discussion

By considering (a) Seebeck coefficient is not generally dependent on the density of material, (b) the grain boundary density in LQ samples was definitely higher than that of SPS samples, and (c) an increase of Seebeck coefficient in LQ samples was observed regardless of compositions, we reached the conclusion that the finite difference observed in Seebeck measurement between LQ and SPS samples can be attributed to energy filtering at grain boundary [2-4]. There was large difference in grain size between LQ and SPS samples, which means higher grain boundary density in LQ samples.

The enhancement of Seebeck coefficient in LQ samples would be closely related to the increase of electrical resistivity. The energy filtering effect should be brought about by the enhanced scattering at a limited energy range. This enhancement of scattering probability naturally leads to an effective increase of electrical resistivity.

The enhancement of Seebeck coefficient of p-type materials, such as the present HMS, should be realized with the strong scattering at the energy range above the chemical potential, despite that we do not have any critical evidence that proves the enhanced scattering at this particular range. It should be investigated with new analytical techniques, and therefore we left this serious point for future study.

The most important point we found in this study is that the high density of grain boundary is capable of increasing power factor. We should investigate this effect for other thermoelectric materials to know whether it is universal behaviour or not.

4.5 Conclusion

In this work we successfully synthesized a higher manganese silicide compound with MnSi/Si as secondary phases in it. The secondary phases were precipitated in nanometer range due to rapid quenching. Simultaneously, this work focused to investigate the effect of grain boundary density on the thermoelectric properties. We clearly observed the finite difference in Seebeck coefficient, which we attributed to energy filtering effect due to grain boundaries by comparing the result of liquid quenched and bulk sintered samples. The energy filtering/scattering effect could improve the Seebeck coefficient up to 120%. Further, the results obtained for $\gamma = 1.67$ SPS sample suggest that the presence of MnSi metallic phase could reduce the electrical resistivity, but a simultaneous increase in electron thermal conductivity nullifies improvement in ZT . Similarly, the precipitation of silicon particles increases electrical resistivity and thermal conductivity, which largely reduces the ZT at room temperature. Hence, we want to conclude that increasing grain boundary density could enhance the power factor of thermoelectric material. The understanding of physical properties and electronic structure of grain boundaries is essential to improve the performance of thermoelectric materials.

4.6 Reference

1. A.B.Gokhale and G.J.Abbaschian: "Mn-Si (Manganese- Silicon)", *Binary Alloy Phase Diagrams*, 2nd Edition, T.B.Massalski, H.Okamoto, P.R.Subramanian and L.Kacprzak ed., OH, ASM International, (1990)
2. Mona Zebarjadi, Keivan Esfarjani, Ali Shakouri, Je-Hyeong Bahk, Zhixi Bian, Gehong Zeng, John Bowers, Hong Lu, Joshua Zide, and Art Gossard. *Applied Physics Letters* 94, no. 20 (2009): 202105.
3. W.J. Xie , Y.G. Yan , S. Zhu , M. Zhou , S. Populoh , K. Gałazka , S.J. Poon , A. Weidenkaff , J. He, X.F. Tang, T.M. Tritt, *Acta Materialia* 61.6 (2013): 2087-2094.
4. Ajay Soni, Yiqiang Shen, Ming Yin, Yanyuan Zhao, Ligen Yu, Xiao Hu, Zhili Dong, Khiam Aik Khor, Mildred S. Dresselhaus, and Qihua Xiong, *Nano letters* 12.8 (2012): 4305-4310.

Chapter 5

Thermoelectric properties of super saturated Cr substituted MnSi_γ

5.1 Introduction

It has been reported that the partial Cr substitution for Mn in HMS could be an effective method to improve the ZT [1,2]. The report showed that the hole-concentration increases with increasing Cr concentration, and the ZT -value was slightly increased from that of Cr-free sample. The improvement in ZT was limited by the amount of Cr substitution for Mn, as the maximum solubility was observed for the $\text{Mn}_{0.8}\text{Cr}_{0.2}\text{Si}_{1.74}$ sample, which contained 7.3 at% Cr. This result suggested that if the solubility limit of Cr in HMS was increased, the ZT -value would be further increased.

Recently, by employing liquid quenching method, the solubility limits of W [3] and Re [4] in Al-Mn-Si was increased. There is similarity in the crystal as well as electronic structure of Al-Mn-Si and HMS. Therefore, we expected that a further increase in the amount of Cr substitution for Mn could be realized by means of liquid quenching method. The larger solubility limit of Cr indicates the wider tuning the carrier concentration, which would help us to obtain a higher ZT -value.

In this chapter, therefore, we focused on revealing the process dependent structural changes and the effect of carrier concentrations on thermoelectric properties of HMS.

5.2 Experimental procedure

A series of higher manganese silicides $\text{Mn}_{36.5-x}\text{Cr}_x\text{Si}_{63.5}$ with Cr concentration varying from $x = 0$ to $x = 11\%$ were synthesized using the following procedure mentioned in chapter 3 section 3.1.2.

5.3 Results

The measured XRD patterns of $\text{Mn}_{36.5-x}\text{Cr}_x\text{Si}_{63.5}$ were plotted in Fig. 5.1. The XRD patterns of arc melted samples clearly showed the precipitation of the impurity CrSi_2 phase at $x \geq 7.3$, whereas this impurity phase disappeared by the rapid quenching (Fig. 5.1 (b)). However, there remained a small amount of MnSi impurity in all the samples and the intensity of impurity peaks increased with increasing Cr concentration. The precipitation of MnSi was confirmed also by the SEM-EDX analysis.

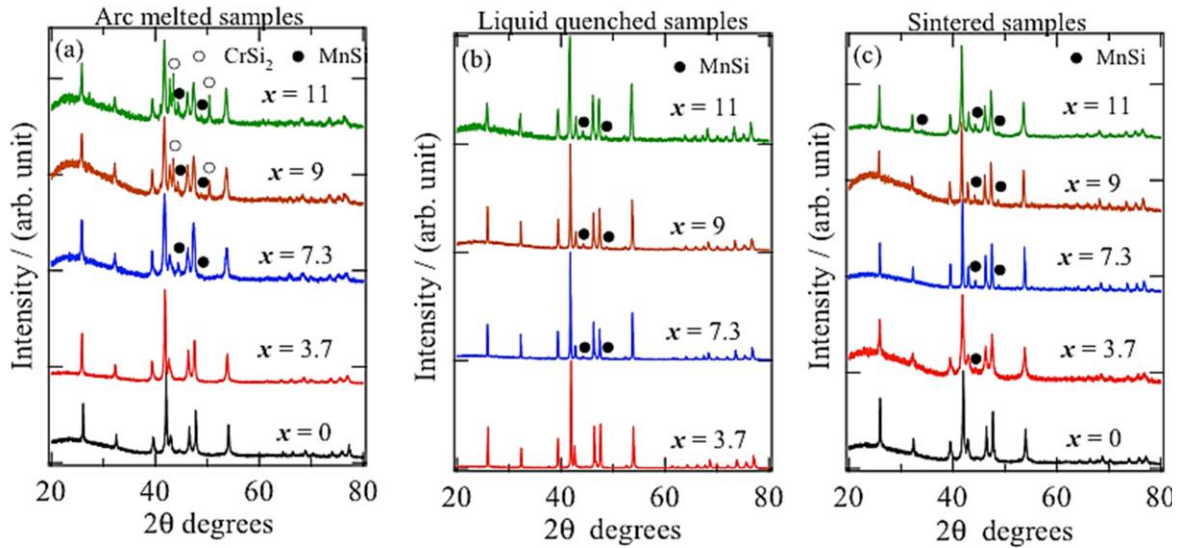


Figure 5.1 Powder X-ray diffraction patterns for (a) arc-melted, (b) liquid-quenched and (c) sintered samples. ($\text{Mn}_{36.5-x}\text{Cr}_x\text{Si}_{63.5}$)

The lattice constants of the sintered samples are plotted in Fig. 5.2 (a) as a function of Cr concentration x . Even after the sintering, the impurity phase CrSi_2 was not observed regardless of Cr concentrations as shown in Fig. 5.1 (c). This fact indicates that the thermal stability of supersaturated solid solution was good enough to keep the nearly single chimney-ladder phase at high temperatures at least up to 1123 K. The relative density for all the sintered samples was more the 91 %, which is good enough to measure thermoelectric properties.

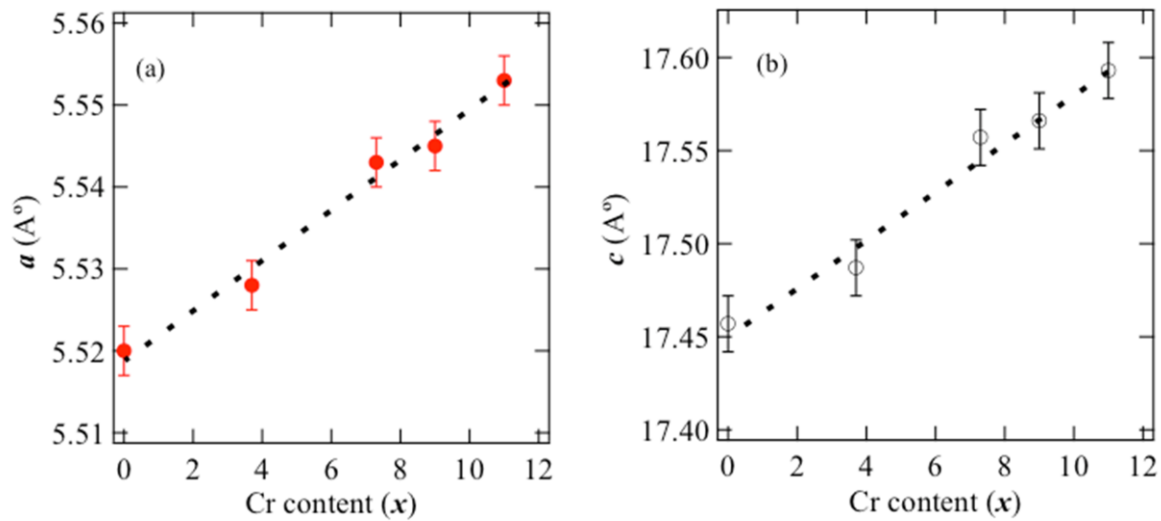


Figure 5.2 Lattice constants ‘*a*’ and ‘*c*’ are plotted as a function of Cr concentration for liquid quenched samples. ($\text{Mn}_{36.5-x}\text{Cr}_x\text{Si}_{63.5}$)

The SEM image of the liquid quenched ribbon shaped $\text{Mn}_{25.50}\text{Cr}_{11}\text{Si}_{63.5}$ was shown in Fig. 3a. We observed a very fine microstructure with an average grain size of ~500 nm. This value was much smaller than ~2000 nm of the rapidly quenched $\text{MnSi}\gamma$. This significant reduction in grain size was related the enhanced nucleation in association with Cr atoms in the rapid quenching process [5]. Figure 5.4 shows the wider range SEM image of $\text{Mn}_{25.50}\text{Cr}_{11}\text{Si}_{63.5}$ sintered sample, where we observed the impurity phase together with the chimney ladder phase. The EDX mapping confirmed that the impurity phase has a composition of (Mn, Cr) Si and it was safely assigned to MnSi-phase. This result was very consistent with the XRD patterns.

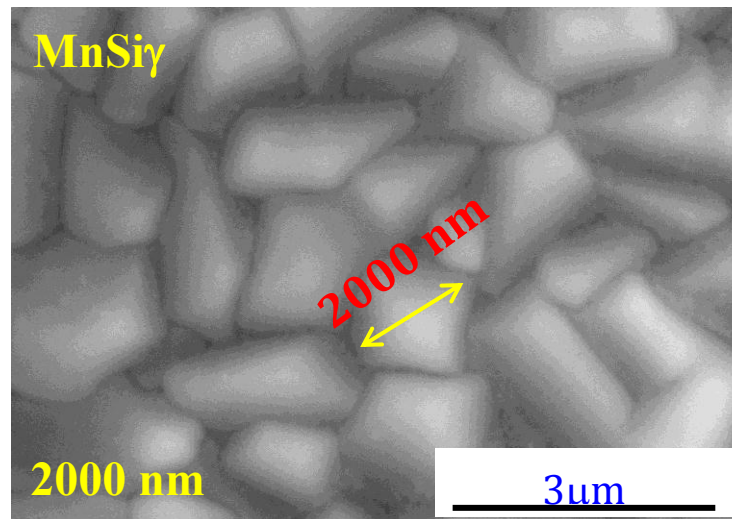
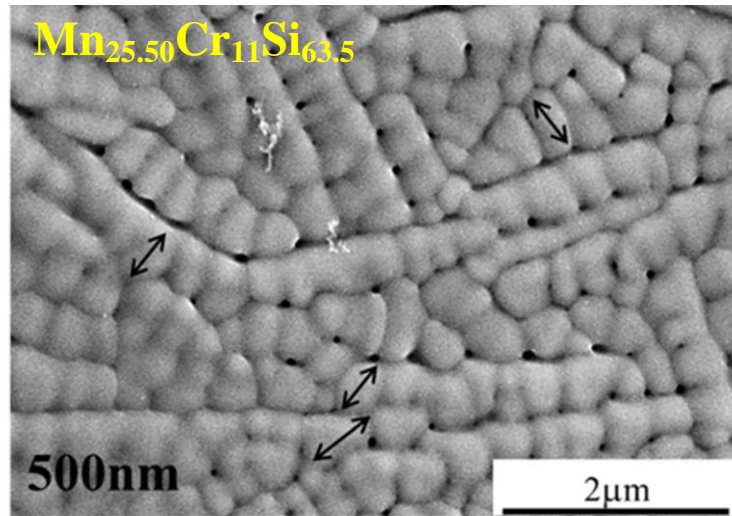


Figure 5.3 SEM image of Mn_{25.50}Cr₁₁Si_{63.5} (top) and Cr free MnSi_y (bottom) of liquid quenched samples with average grain size of 500nm and 2000nm, respectively.

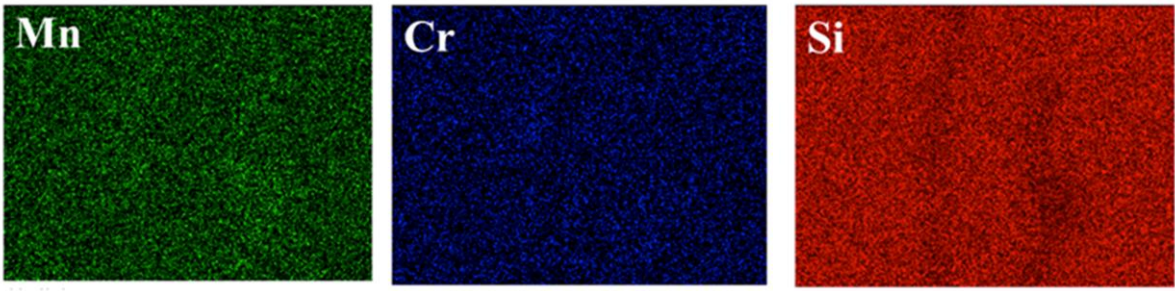
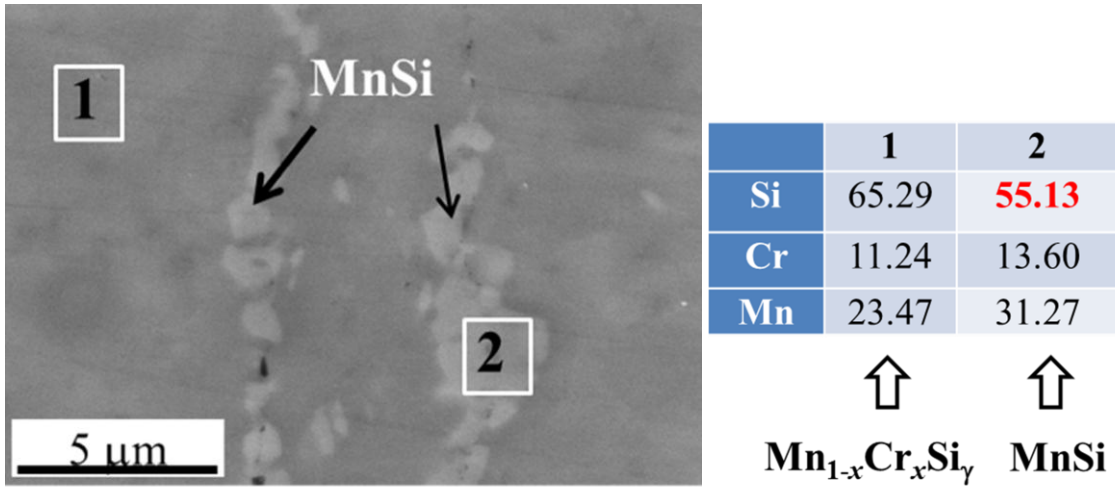


Figure 5.4 SEM image of $\text{Mn}_{25.50}\text{Cr}_{11}\text{Si}_{63.5}$ sintered sample with point 1 and point 2 showing the composition of matrix and the secondary phase, respectively. The elemental mapping for silicon, manganese, and chromium is shown for the same region as SEM image.

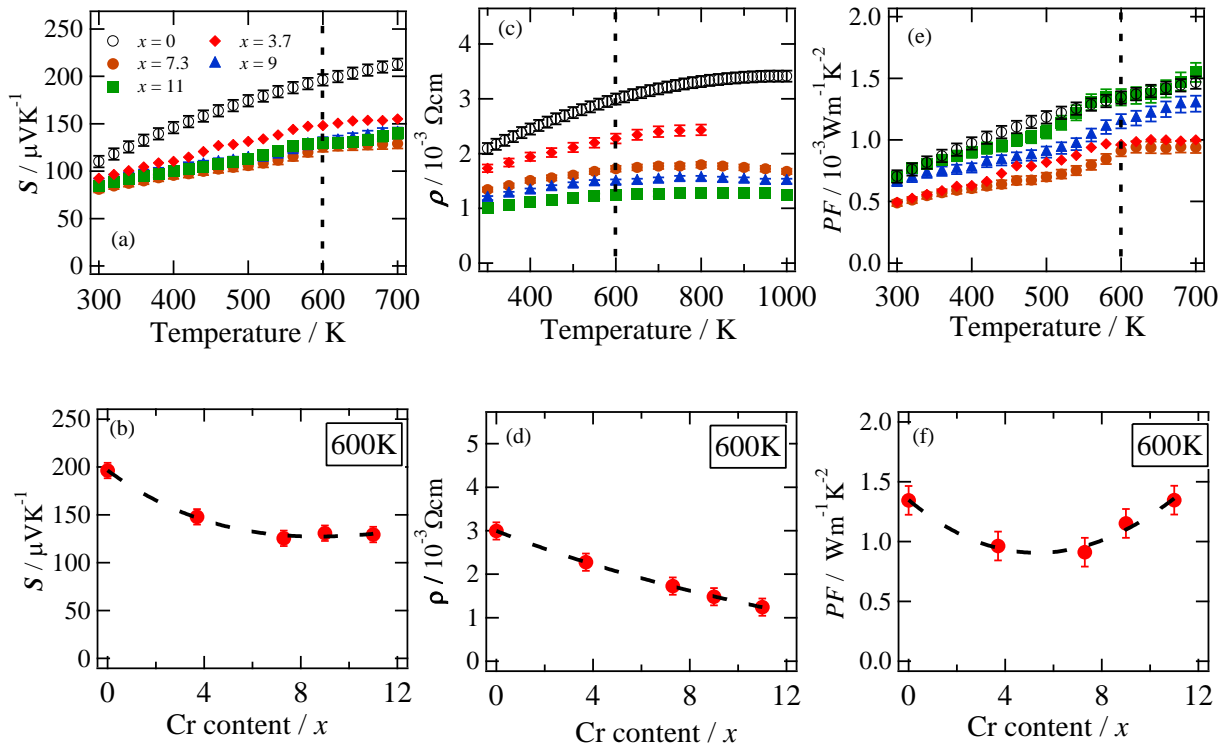


Figure 5.5 Temperature dependent (a) Seebeck coefficient, (c) electrical resistivity, (e) power factor for $\text{Mn}_{36.5-x}\text{Cr}_x\text{Si}_{63.5}$ composition. The (b) Seebeck coefficient, (d) electrical resistivity, and (f) power factor at 600 K are plotted as function of Cr concentration.

The temperature dependence of Seebeck coefficients were plotted in Fig. 5.5 (a), and their values at 600 K were plotted in Fig. 5.5 (b) as a function of Cr concentration x . The Seebeck coefficient of $\text{Mn}_{36.5}\text{Si}_{63.5}$ at 600 K was $200 \mu\text{VK}^{-1}$ which was the largest among the present samples, and the value of Seebeck coefficient was reduced with increasing Cr concentration up to 7 at.% and saturated at $\sim 130 \mu\text{VK}^{-1}$ for the larger Cr concentration. A very small increase of Seebeck coefficient was also observable for $x > 9$ from that of $x = 7$. The reduction in Seebeck coefficient must be related to the increased carrier concentration because the number of valence electron in Cr is smaller than that of Mn.

The electrical resistivity shown in Figs. 5.5 (c) and (d) was reduced with Cr substitution. The reduction of electrical resistivity indicates that the hole-concentration was increased with Cr substitutions. It is also very important to note that very weak temperature dependence, which is almost flat at high temperature [1] was observable especially for the samples containing more than 7 at. % Cr. The less obvious temperature dependence of electrical resistivity means that the mean free path of carriers reached the minimum value known as Mott-Ioffe-Regel limit [6] never to be further shortened.

The temperature dependence of power factor PF was plotted in Fig. 5.5 (e), and the value of PF at 600 K was also plotted in Fig. 5.5 (f) as a function of Cr concentration x . We observed a local minimum of PF at around $x = 3.7$ in Fig. 5.5 (f). The increases of PF at $x < 3.7$ and $x > 3.7$ were attributed to the increase of Seebeck coefficient and the decrease of electrical resistivity, respectively. The largest value of PF at 600 K was $1.4 \text{ Wm}^{-1}\text{K}^{-2}$ and this value was realized both at $x = 0$ and 11.

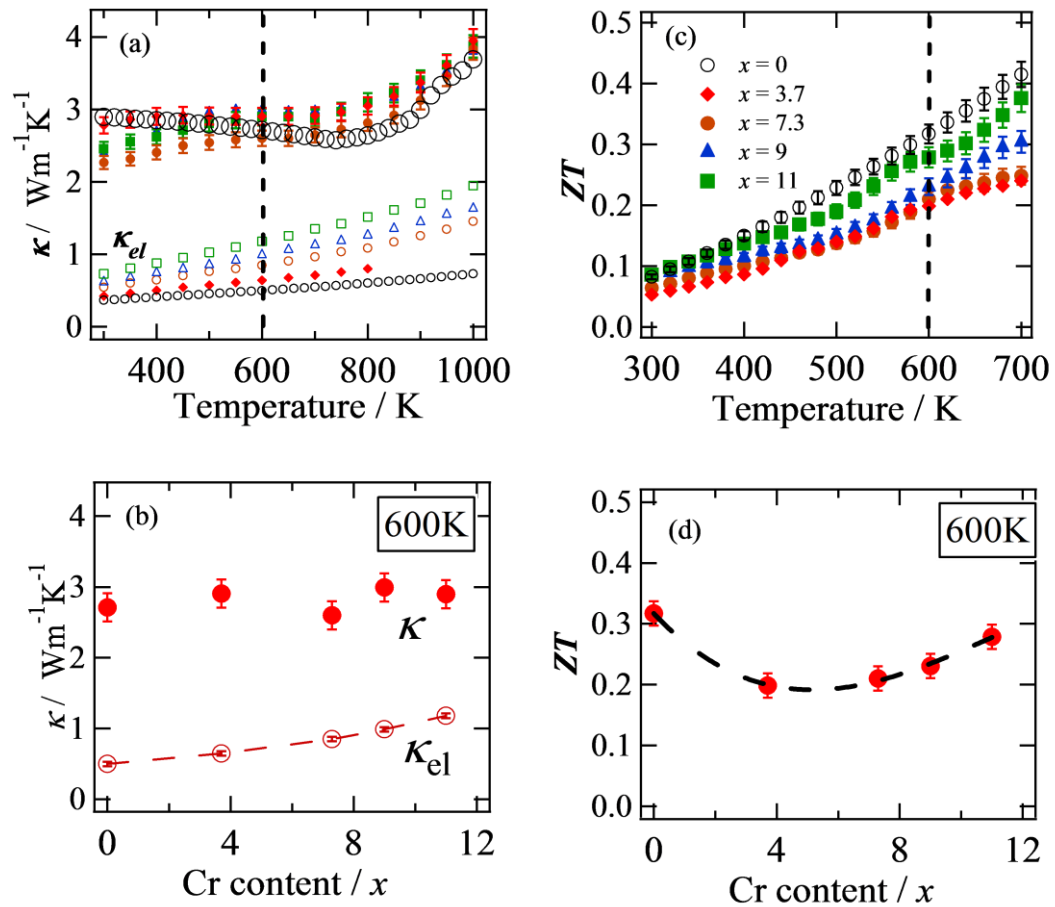


Figure 5.6 Temperature dependence of (a) thermal conductivity and (c) ZT for $\text{Mn}_{36.5-x}\text{Cr}_x\text{Si}_{63.5}$ composition. The (b) thermal conductivity and (d) ZT -values at 600K are plotted as function of Cr concentration.

The measured thermal conductivity was plotted as a function of temperature in Fig. 5.5 (a). Its values at 600 K were also plotted as a function of x in Fig. 5.6 (b). We confirmed that the lattice thermal conductivity was hardly affected by Cr substitution presumably due to the similar atomic mass of Cr and Mn. The electrical thermal conductivity, on the other hand, increased with increasing Cr concentration because of the increased number of carrier concentration. The linear increase of κ_{el} with increasing temperature was naturally brought about by the nearly temperature independent σ and the Wiedemann-Franz law $\kappa_{el} = L_0\sigma T$ used to estimate the electron thermal conductivity.

The temperature dependence and composition dependence of ZT were plotted in Fig. 5.6 (c) and (d), respectively. The behavior of ZT was similar to the power factor. The highest value of ZT was observed at $x = 0$, and the sample at 11 at.% Cr showed comparable value with that of $x = 0$. The minimum value of ZT at 600 K was observed at $x = 3.7$.

5.4 Discussion

The present results of transport properties are definitely conflicting with the results reported by Y. Kikuchi *et al.*, [1] who claimed the power factor and ZT increased with increasing Cr concentration, but our results showed the maximum values were obtained for the Cr free sample. We considered that the difference lied in the carrier concentration of Cr-free sample, which could be varied by different composition or different synthesis technique because of the high vapor pressure of Mn. The XRD patterns reported by Y. Kikuchi *et al.* showed a small amount of silicon precipitation, while our samples showed the precipitation of MnSi. This means that the samples reported by Y. Kikuchi *et al.* and our samples stayed in the highest and lowest Si concentrations, respectively. At the composition, our sample showed the maximum ZT , while Kikuchi's sample presumably stayed at a condition of smaller carrier concentration.

The increase of ZT at $x > 7$ is also very important. In the present study, we succeeded in increasing the solubility limit of Cr in HMS by employing the liquid quenching technique. However, near the solubility limit ZT showed increasing tendency with increasing Cr concentration. We strongly expect that the value of ZT would increase more if we could increase the solubility limit of Cr to $x > 11$. This could be realized when we employ a faster quenching technique, i.e., the much higher rotating speed or a larger diameter of Cu wheel in the liquid quenching apparatus.

Before closing discussion, we would like to briefly comment on the grain size of samples. We observed very fine grains in the liquid quenched, Cr-substituted HMS. We also considered that the reduction of grain size is attributed to the rapid quenching and the increased number of nucleation sites in association with Cr atoms. Recently, the energy filtering effect to increase Seebeck coefficient was reported for the several different compounds [7, 8]. In chapter 4 we had confirmed that the energy filtering effect can be introduced by grain boundaries. If it is the case, the fine grain boundary realized in the present samples, would contribute to the increase of ZT .

5.5 Conclusion

We succeeded in increasing the solubility limit of Cr in HMS up to 11 at.% from 7 at.% by employing a liquid quenching technique. We also obtained a fine microstructure with average grain size of ~500 nm. As a result, the largest ZT of ~0.4 at 700K was observed both at $x = 0$ and 11.

5.6 References

1. Y. Kikuchi, Y. Miyazaki, Y. Saito, K. Hayashi, K. Yubuta, T. Kajitani, *Jpn. J. Appl. Phys.* **51**, (2012) 085801. doi:10.1143/JJAP.51.085801
2. V. Ponnambalam, Donald T. Morelli, *J. Electron. Mater.*, **41(6)**, (2012), pp. 1389-1394.
3. Yamamoto, H. Miyazaki, and T. Takeuchi: *J. Appl. Phys.* **115**, 23708 (2014).
4. Yamamoto, H. Miyazaki, M. Inukai, Y. Nishino, and T. Takeuchi: *Jpn. J. Appl. Phys.*, **54**, 071801 (2015).
5. T.Z. Kattamis and S. Skolianos, *Rapid Quenching of Metals*, ed. by S. Steeb, **Vol. 1** (Elsevier , Germany, 1985), pp. 51-54.
6. N. E. Hussey, K. Takenaka, H. Takagi: *Phil. Mag.* **84**, 2847 (2004).
7. M. Zebarjadi, K. Esfarjani, A. Shakouri, Je-Hyeong Bahk, Z. Bian, G. Zeng, J. Bowers, H. Lu, J. Zide, and A. Gossard, *Appl. Phys. Lett.* 94, no. 20 (2009): 202105.
8. A. Soni, Y. Shen, M. Yin, Y. Zhao, L. Yu, X. Hu, Z. Dong, K. A. Khor, M. S. Dresselhaus, and Q. Xiong, *Nano letters* 12.8 (2012): 4305-4310.

Chapter 6

Enhanced thermoelectric properties of W and Fe substituted MnSi

6.1 Introduction

In this Chapter, we focused on preparing the cheapest and most efficient higher manganese silicide compound for the thermoelectric generator by introducing heavy tungsten atoms as the substitute for manganese atoms. We selected tungsten partly because it was used for the partial substitution for manganese in Si₂Ti-type Al-Mn-Si, which has a similar local atomic arrangement with that of HMS [1], and partly because it is non-toxic and the cheapest element among the all 5d transition metal elements leading to the significant reduction of lattice thermal conductivity. Considering the negligibly small solubility limit of W in higher manganese silicide [2], we have used a rapid quenching technique to increase the solubility limit. Besides, to find out the optimal carrier concentration for both p-type and n-type conditions, we simultaneously employed Fe substitution for Mn.

6.2 Results

The measured X-ray diffraction (XRD) patterns of Mn_{36.36-x}W_xSi_{63.64} ($0 \leq x \leq 7.3$) are plotted in Fig. 6.1 (a) and Fig. 6.1 (b) for arc-melted samples and liquid quenched samples, respectively. The XRD patterns of arc-melted samples clearly show peaks of impurity phases (Si₂W and MnSi) even with a very small amount of W. On the contrary, the impurity peaks disappears for $x = 1.8$ and $x = 3.6$ after the liquid quenching. In Fig. 6.1 (c), the lattice constant calculated from the XRD data of the liquid quenched samples monotonically increased with increasing W concentration at $x \leq 3.6$, and it was almost constant at $3.6 \leq x \leq 7.3$. These data clearly indicate that the solubility limit is at least 3.6 at.% W in higher manganese silicide when prepared by liquid quenching.

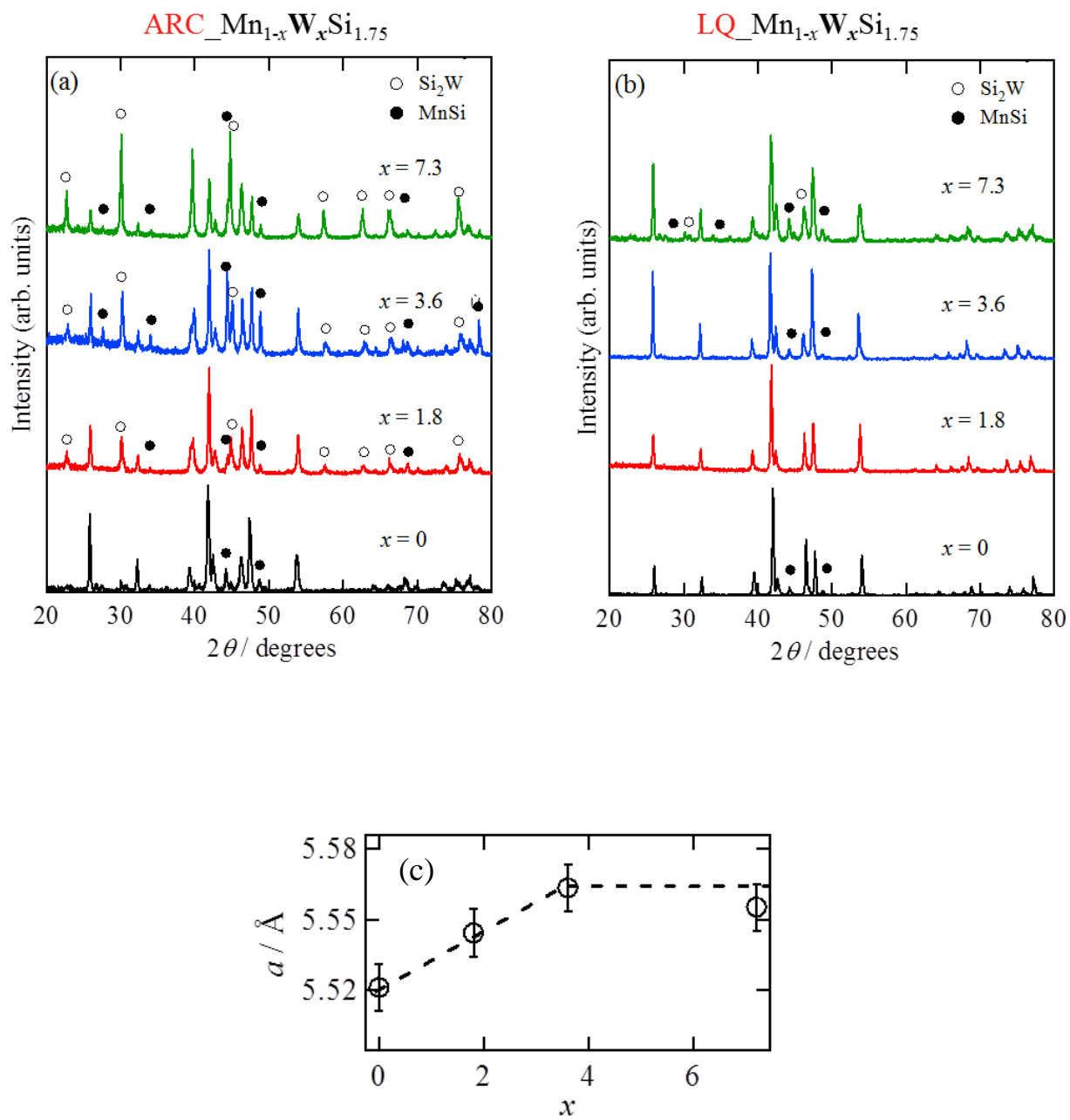


Figure 6.1 XRD data plotted of (a) arc-melted and (b) liquid-quenched $\text{Mn}_{36.4-x}\text{W}_x\text{Si}_{63.6}$. Lattice constant a is plotted as a function of W concentration in (c).

After successfully obtaining the solid solution with W, the carrier concentration was controlled by additionally substituting Fe for Mn. The solubility limit of Fe in HMS was found to reach up to 15 at.%, which can be clearly confirmed from the XRD patterns shown in Fig. 6.2 (a) and (b). Miyazaki *et al.* reported that the solubility limit of Fe in HMS was less than 10 at.% [3]. The increase of Fe concentration would be caused in association with the simultaneously introduced W, this is similar to results obtained for the double doped (Al, Fe) HMS solid solution, where the solubility limit of Al was increased by Fe substitution [4].

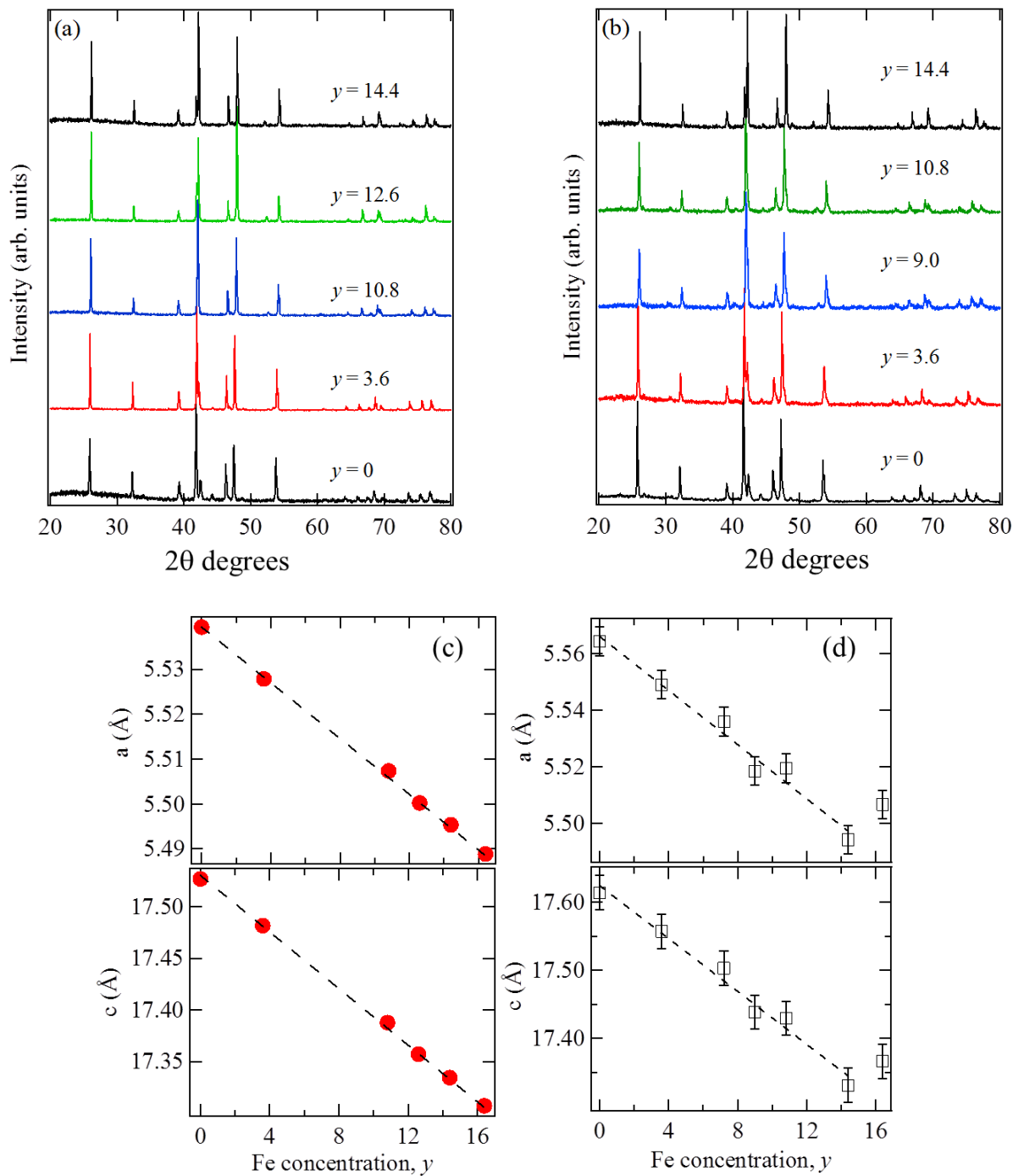


Figure 6.2 XRD data plotted of liquid-quenched (a) $\text{Mn}_{34.6-y}\text{W}_{1.8}\text{Fe}_y\text{Si}_{63.6}$ and (b) $\text{Mn}_{32.8-y}\text{W}_{3.6}\text{Fe}_y\text{Si}_{63.6}$. Lattice constants a and c are plotted as a function of W concentration in (c) and (d) for $\text{Mn}_{34.6-y}\text{W}_{1.8}\text{Fe}_y\text{Si}_{63.6}$ and $\text{Mn}_{32.8-y}\text{W}_{3.6}\text{Fe}_y\text{Si}_{63.6}$, respectively.

The large amount of Fe in HMS naturally leads to a larger number of electron concentration, which can be used to prepare an n-type material. Thermoelectric properties of liquid quenched and bulk samples were investigated.

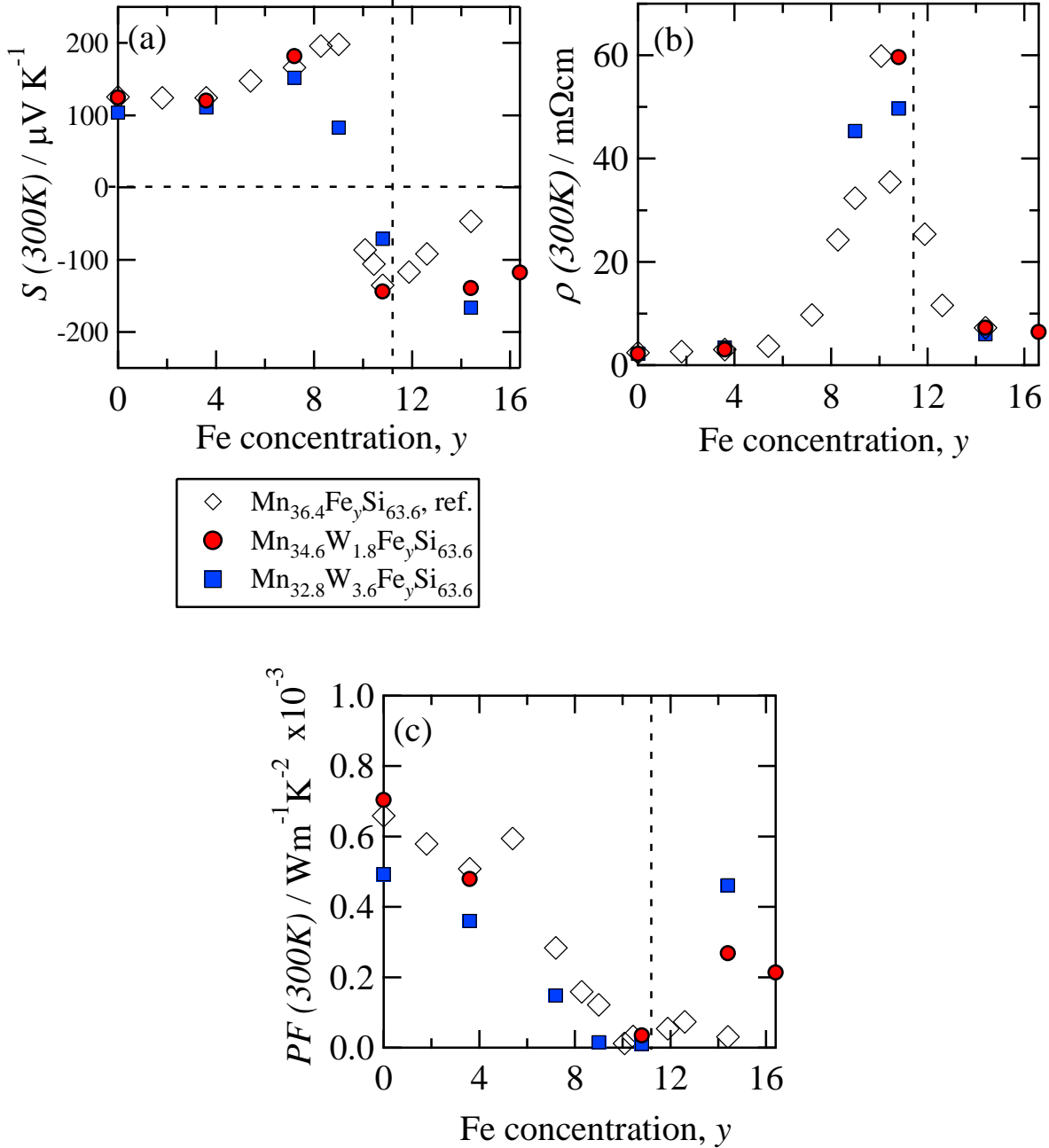


Figure 6.3 (a) Seebeck coefficient, (b) electrical resistivity, and (c) PF of $\text{Mn}_{36.6-y}\text{Fe}_y\text{Si}_{63.4}$, [Ref. 9] $\text{Mn}_{34.6-x}\text{W}_{1.8}\text{Fe}_y\text{Si}_{63.6}$, and $\text{Mn}_{32.8-x}\text{W}_{3.6}\text{Fe}_y\text{Si}_{63.6}$ at room temperature are plotted as a function of Fe concentration.

Seebeck coefficient at room temperature is plotted as a function of Fe concentration in Fig. 6.3 (a). All the three series of samples, $\text{Mn}_{34.6-y}\text{W}_{1.8}\text{Fe}_y\text{Si}_{63.6}$ ($0 \leq y \leq 14.4$), $\text{Mn}_{32.8-y}\text{W}_{3.6}\text{Fe}_y\text{Si}_{63.6}$ ($0 \leq y \leq 14.4$), and $\text{Mn}_{36.4-y}\text{Fe}_y\text{Si}_{63.6}$ [3], show similar behavior irrespective of different W content. This fact indicates that tungsten atom does not produce any impurity states near the chemical potential when it is located in Mn-site in HMS. The sign of Seebeck coefficient was positive at $y \leq 10$ while it turned out to be negative at $y \geq 10$.

The magnitude of electrical resistivity divergently increased near the compositions where Seebeck coefficient showed the sign-reversal. This fact is well interpreted for the presence of energy gap between the valence and conduction bands together with the shift of Fermi energy by varying Fe concentration. Fig. 6.3 (c) shows composition dependence of power factor. The maximum power factor for p-type $\text{Mn}_{34.56}\text{W}_{1.8}\text{Si}_{63.64}$ $0.7 \text{ mWm}^{-1}\text{K}^{-2}$ and for n-type $\text{Mn}_{18.36}\text{W}_{3.6}\text{Fe}_{14.4}\text{Si}_{63.6}$ $0.46 \text{ mWm}^{-1}\text{K}^{-2}$ was obtained at 300 K.

The ribbon samples prepared in this study were thermodynamically metastable and therefore the thermal stability was investigated by Differential Thermal Analysis (DTA). As a typical example, we plotted the DTA curve observed for $\text{Mn}_{32.76}\text{W}_{3.6}\text{Si}_{63.64}$ in Fig. 6.4 (a). A sharp exothermic peak was observed at around 1000 K, presumably indicating the phase transition from metastable HMS to a mixed phase of HMS and other. Figure 6.4 (b) shows the XRD pattern of the sample heat treated above 1000K, which clearly shows secondary phases. The working temperature of HMS is supposed to be lower than 900 K because it possesses the largest value typically at around 800 K [5]. These facts let us firmly believe that the thermal stability of the metastable HMS containing a small amount of W is good enough for making the samples usable in practical applications, if the bulk sample can be prepared below 1000 K.

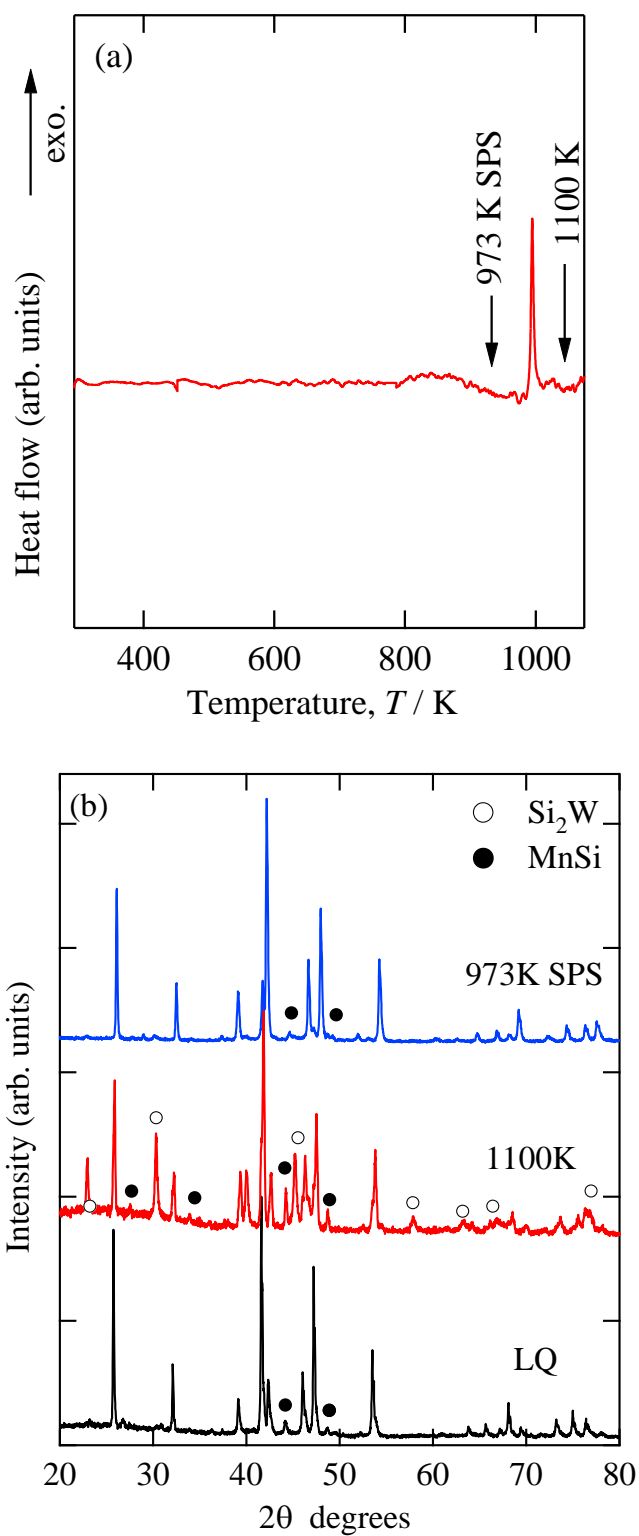


Figure 6.4 (a) DTA curve of liquid quenched $\text{Mn}_{32.8}\text{W}_{3.6}\text{Si}_{63.4}$ and (b) XRD patterns measured after liquid quenching, heat treatment at 1100 K and sintering at 973K.

The sintering temperature for HMS, however, was reported to be 1223 K, which is much higher than the decomposing temperature. Therefore, we tried to employ a high pressure (100 MPa), and long duration (150 min) for the pulse current sintering process at 973K. As a consequence, bulk samples having 90 % of theoretical density were successfully prepared for p-type $\text{Mn}_{32.6}\text{W}_{1.8}\text{Si}_{63.6}$ and n-type $\text{Mn}_{18.4}\text{W}_{3.6}\text{Fe}_{14.4}\text{Si}_{63.6}$. In Fig.4 (b) the XRD pattern shows almost no phase separation for the sintered sample. Although the density was slightly smaller than the ordinary samples, we decided to study the thermoelectric properties of these slightly porous samples.

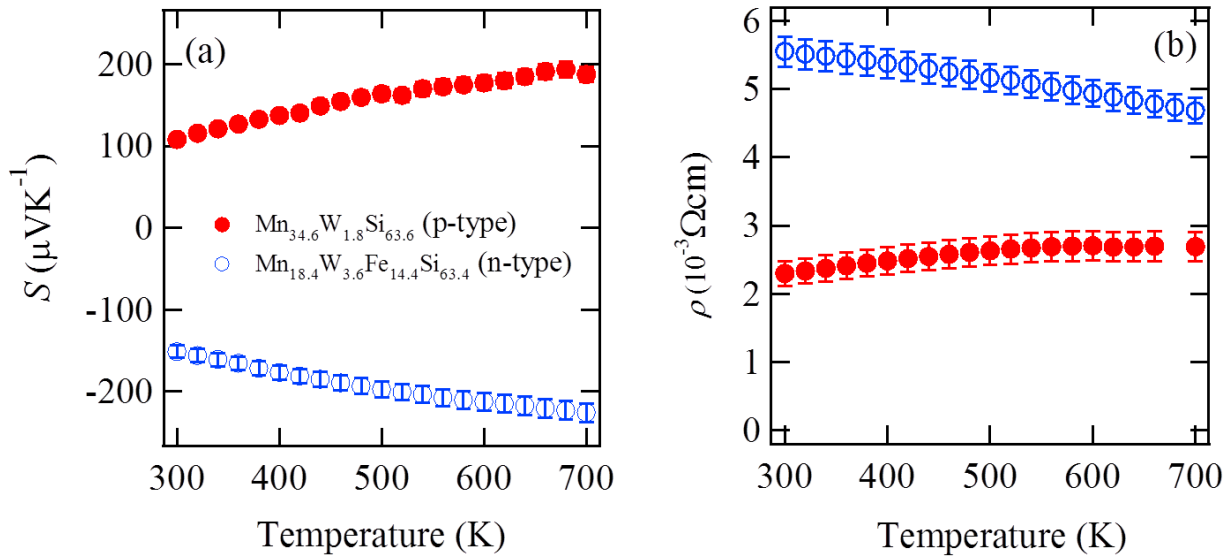


Figure 6.5 (a) Seebeck coefficient and (b) electrical resistivity observed for p-type $\text{Mn}_{34.6}\text{W}_{1.8}\text{Si}_{63.6}$ and n-type $\text{Mn}_{18.4}\text{W}_{3.6}\text{Fe}_{14.4}\text{Si}_{63.6}$ bulk samples.

Figure 6.5 shows the temperature dependence of the thermoelectric properties of the prepared bulk samples. We should note that the Seebeck coefficient of the present p-type $\text{Mn}_{32.56}\text{W}_{1.8}\text{Si}_{63.64}$ shows almost the same magnitude and temperature dependence with that of $\text{Mn}_{36.36}\text{Si}_{63.64}$ most likely due to the absence of impurity states near the chemical potential in association with tungsten atoms. The electrical resistivity of p-type $\text{Mn}_{34.6}\text{W}_{1.8}\text{Si}_{63.6}$ shows slightly larger value than that of p-type $\text{Mn}_{36.36}\text{Si}_{63.64}$ mainly due to the lower density.

The thermal conductivity of p-type $\text{Mn}_{34.6}\text{W}_{1.8}\text{Si}_{63.6}$ plotted in Fig. 6.6 (a) showed a lower value than that of $\text{Mn}_{36.36}\text{Si}_{63.64}$ due to the low density and phonon scattering effect of W. As a result, the magnitude of ZT was increased by 10 % for p-type $\text{Mn}_{32.56}\text{W}_{1.8}\text{Si}_{63.64}$ from that of p-type $\text{Mn}_{36.36}\text{Si}_{63.64}$. The largest ZT value reached up to 0.5 at 700 K, and this value is supposed to increase at around 800 K (Fig. 6.6 (b)).

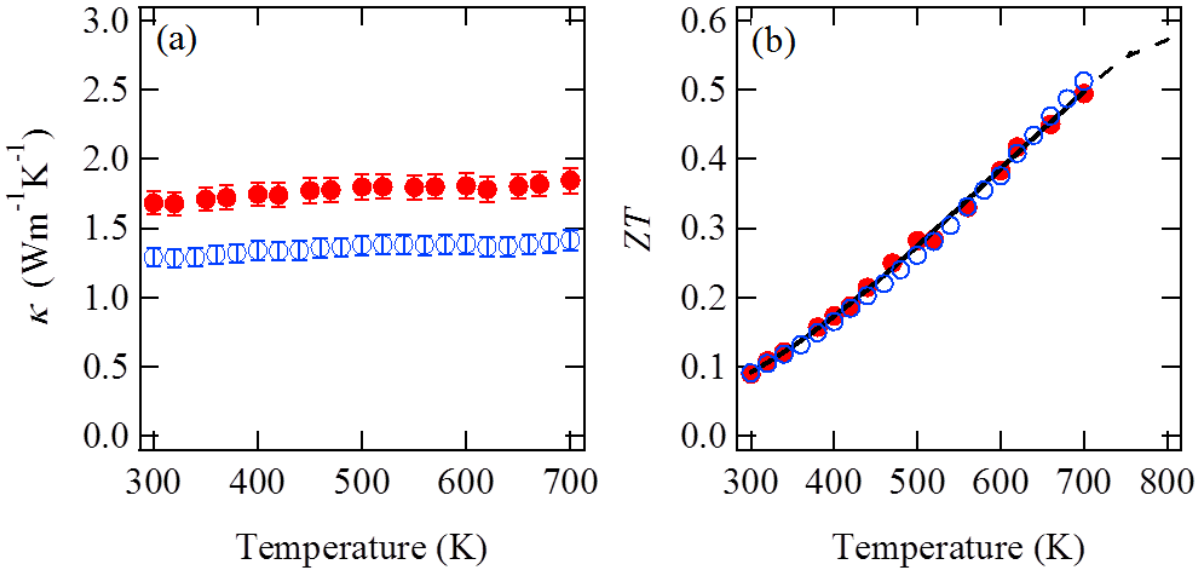


Figure 7.6 (a) thermal conductivity and (b) dimensionless figure of merit observed for p-type $\text{Mn}_{34.6}\text{W}_{1.8}\text{Si}_{63.6}$ and n-type $\text{Mn}_{18.4}\text{W}_{3.6}\text{Fe}_{14.4}\text{Si}_{63.6}$ bulk samples.

Notably, n-type $\text{Mn}_{18.4}\text{W}_{3.6}\text{Fe}_{14.4}\text{Si}_{63.6}$ also shows almost the same magnitude of ZT with that of p-type $\text{Mn}_{32.6}\text{W}_{1.8}\text{Si}_{63.6}$, which is the largest value ever observed for n-type HMS. This result together with the non-toxic, less-expensive characteristics strongly let us to believe that HMS could become practical thermoelectric material widely used for various applications.

6.3 Discussion

The magnitude of ZT observed for the present HMS containing a small amount of tungsten was much less than unity, and was presumably inappropriate for practical applications. However, we still have a chance to increase the ZT -value by using other 5d transition metal elements. For example, ZT of Si_2Ti -type Al-Mn-Si alloys was increased by partial substitution of Ru and Re for Mn. [6] The lattice thermal conductivity of these alloys was drastically decreased with increasing heavy element concentrations. Notably, these heavy elements were selected because their substitution for Mn does not produce impurity states near the chemical potential to sustain the good electron transport properties for thermoelectric applications. The similarity in local atomic arrangements between Si_2Ti -type structure, Cr_2Si -type structure, and HMS suggests that the partial substitution of W, Re, and Ru for Mn can effectively reduce the lattice thermal conductivity of HMS without greatly affecting the electron transport properties.

6.4 Conclusion

In this study, we have tried to improve the performance of HMS by simultaneously substituting W and Fe for Mn. The rapid cooling by single role liquid quenching technique effectively increased the solubility limit of W in HMS up to 3.6 at.%. The simultaneous substitution of Fe and W for Mn has helped in obtaining both n-type and p-type samples. We have successfully prepared bulk samples by using low temperature (973 K), high pressure (100 MPa) and long sintering (150 min.) technique even below the phase transition temperature, which was not possible by using conventional sintering parameter used for HMS. The W substitution has effectively reduced the thermal conductivity without affecting the electronic structure, which led to improvement in the magnitude of ZT . The maximum ZT value of 0.5 was obtained not only for p-type but also of n-type sample at 700K.

6.5 References

1. A. Yamamoto, H. Miyazaki, M. Inukai, Y. Nishino, T. Takeuchi, *Jpn. J. Appl. Phys.* 071801. (2015) doi:10.7567/JJAP.54.071801
2. P. Villars, A. Prince, H. Okamoto, *Handbook of ternary alloy phase diagram*, (ASM International, Ohio, 1995) Vol. 10, p. 12463.
3. Yuzuru Miyazaki and Yuta Kikuchi, *Thermoelectric Nanomaterials*, ed. by K. Koumoto and T. Mori (Springer, Heidelberg, 2013) Vol. 182, pp.141-155.
4. S.A. Barczak, R.A. Downie, S. R. Popuri, R. Decourt, M. Pollet, J. W. G. Bos, *J. Solid State Chem*, 227, 55–59. (2015) doi: 10.1016/j.jssc.2015.03.017
5. T. Itoh, and M. Yamada, *J. Electron. Mater.*38, 925-929. (2009)
6. A. Yamamoto, H. Miyazaki, T. Takeuchi, *J. Appl. Phys.* 115, 023708.(2014) doi:10.1063/1.4861643

Chapter 7

Enhancement of power factor by energy filtering in Re-substituted HMS

7.1 Introduction

The heavy element substitution is an effective strategy to reduce the lattice thermal conductivity. In Chapter 6 we showed that the lattice thermal conductivity was effectively reduced by W substitution. Similarly, Re substitution in Al-Mn-Si C54 phase and C40 phase had effectively reduced the lattice thermal conductivity [1-2]. These substitutions did not strongly affect the electron transport properties, because of the absence of impurity states near the chemical potential and the strongest scatterings limit of conduction electrons. The HMS has the similar crystal structure with that of Al-Mn-Si C54-phase, so we considered that the Re substitution should work for HMS to reduce the lattice thermal conductivity without affecting electron transport properties. To obtain smallest lattice thermal conductivity by Re substitution, we need to increase the solubility of Re in HMS, which was limited to 2 at% [3]. In Chapter 5 and Chapter 6, we succeeded in increasing the solubility limits for Cr and W/Fe by employing liquid quenching technique. In this chapter we tried to combine two different strategies (1) Reducing lattice thermal conductivity by increasing the solubility limit of Re in HMS and (2) implementing energy filtering effect by grain boundaries in HMS (Chapter 4) to increase the power factor.

7.2 Results for bulk samples

The powder XRD patterns and the lattice constants of quenched ribbon samples prepared at the nominal compositions of $\text{Mn}_{36.4-x}\text{Re}_x\text{Si}_{63.6}$ ($0 \leq x \leq 18$) are shown in Fig. 7.1 (a). No evidence of an impurity phase was observed up to 10 at.% Re, whereas the samples prepared at 12 and 18 at.% Re clearly showed diffraction peaks from the secondary phase, ReSi_2 . The lattice constants monotonically increased with increasing Re concentration at $x \leq 10$, but became constant at $10 \leq x \leq 18$ (Fig. 7.1 (b)). Thus, the maximum solid solubility limit of Re in HMS prepared in our currently employed process was determined to be ~ 10 at. %.

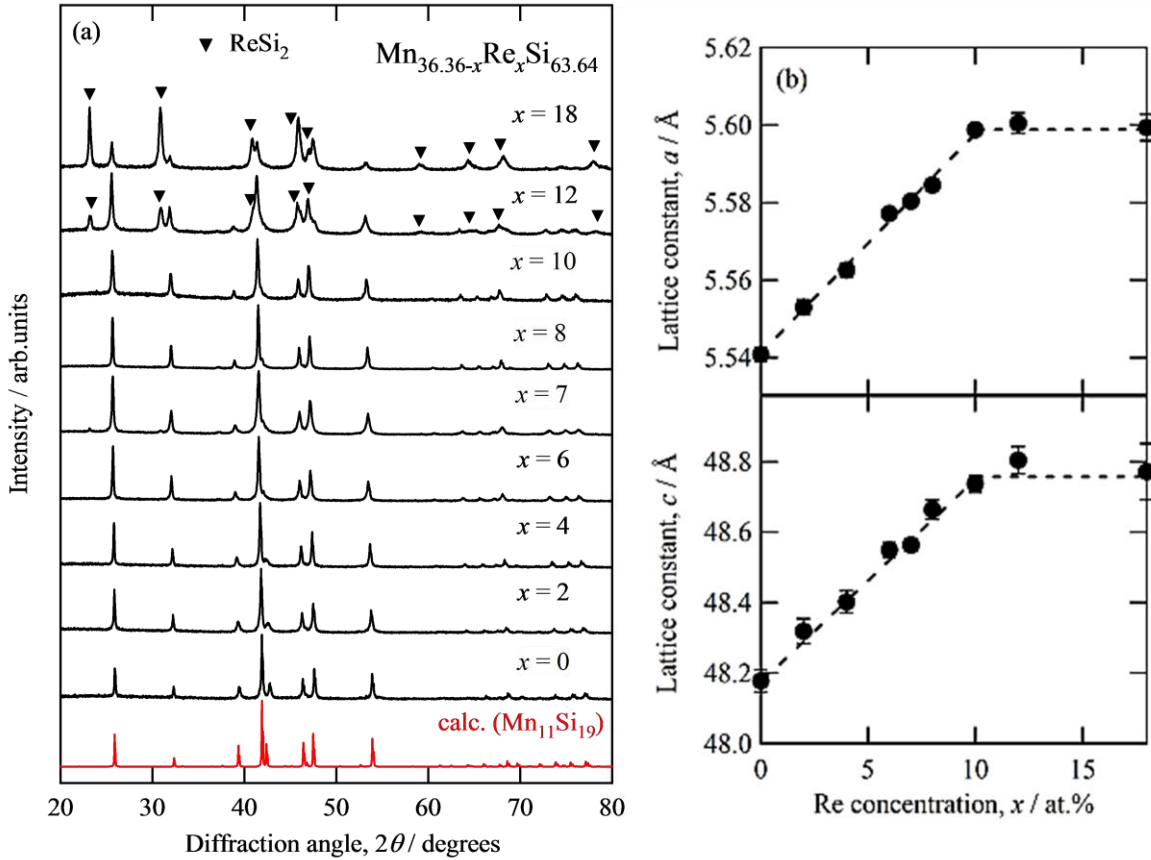


Figure 7.1 (a) XRD patterns for the Re substituted HMS samples, (b) lattice constant 'a' and 'c' plotted with respect to Re concentration.

Seebeck coefficient at room temperature shown in Fig. 7.3 (a) slightly increased with increasing Re concentration up to 6 at.%, but it turns out to be reduced at $x > 6$ after taking the maximal value at $x = 6$. The electrical resistivity (Fig. 7.3 (b)), on the other hand, showed a monotonic reduction with increase in Re concentration. These variations in electron transport properties indicate that Re substitution for Mn produces a small but finite number of impurity states near the chemical potential despite that those states are absent from Al-Mn-Si C54-phase. Although the variation in electron transport properties reduces power factor of many thermoelectric materials, but the power factor of HMS fortunately was slightly increased due to the unchanged Seebeck coefficient and the reduced electrical resistivity.

The clear evidence of reduction in lattice thermal conductivity by the partial substitution of heavy element is shown in Fig. 7.4 (a). The strategy of heavy element substitution worked for Re-HMS. The lattice thermal conductivity reduced drastically with Re concentration. Notably, the ZT showed the maximum value at 6 at.% Re (Fig. 7.4 (b)).

The temperature dependence of S , ρ , κ and ZT are shown in Fig. 7.5. The Seebeck coefficient showed increasing tendency with temperature for all the compositions up to 950 K (Fig. 7.5 (a)). Electrical resistivity showed very weak temperature dependence for higher Re concentration (Fig. 7.5 (b)). Similar to the electrical resistivity, thermal conductivities for higher concentration was almost flat at higher temperature (Fig. 7.5 (c)). Hence, the effective reduction in the absolute value of lattice thermal conductivity, weak temperature dependence of electrical conductivity and lattice thermal conductivity, and unchanged Seebeck coefficient increased the ZT . The ZT value at 920 K was increased from 0.5 for Re free HMS to 1.04 for 6 at% Re HMS, which was 2.1% larger.

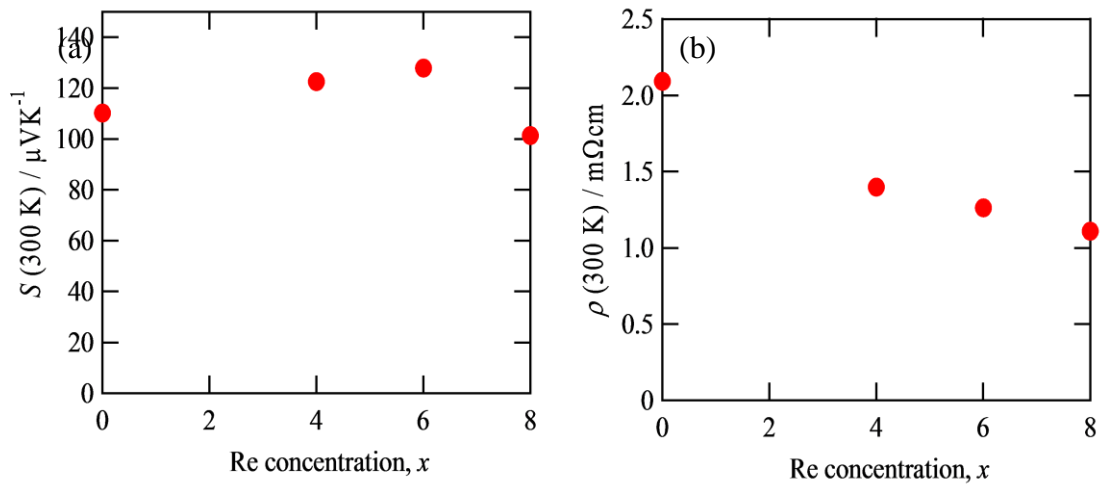


Figure 7.3 Re concentration dependence of (a) Seebeck coefficient (left) (b) electrical resistivity (right) plotted at 300 K for $\text{Mn}_{36.4-x}\text{Re}_x\text{Si}_{63.6}$.

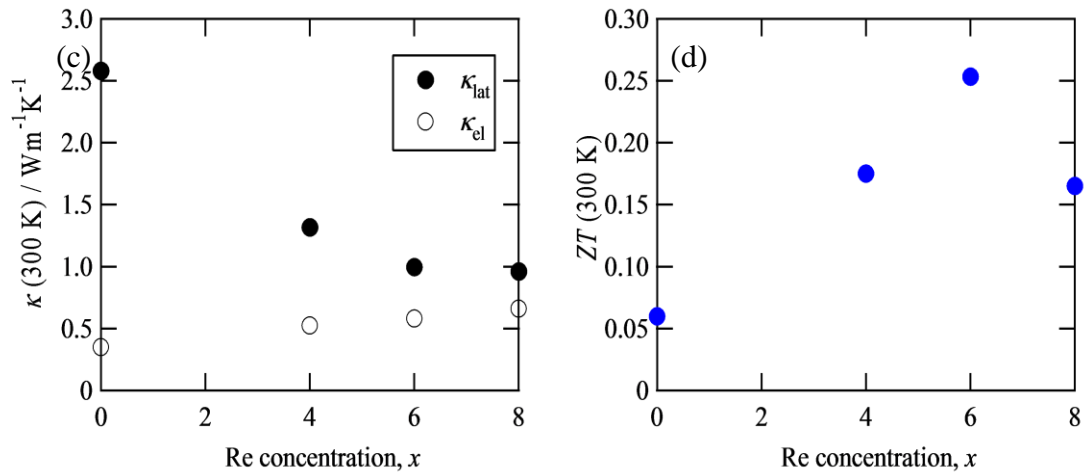


Figure 7.4 Re concentration dependence of (a) thermal conductivity (left) (b) ZT (right) plotted at 300 K

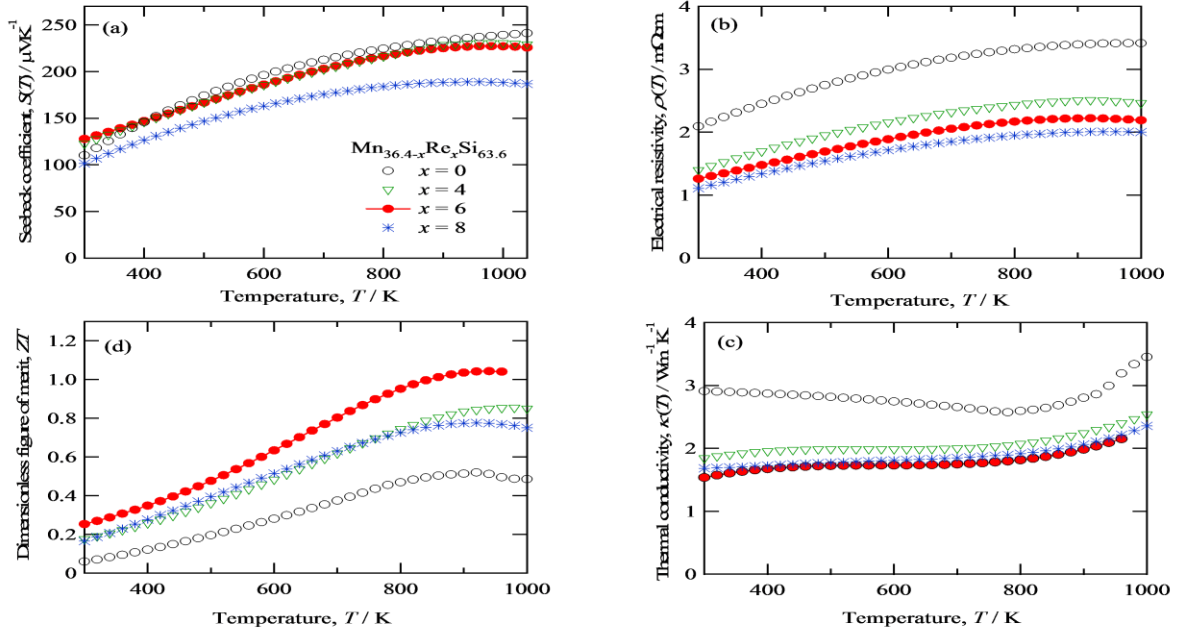


Figure 7.2 Temperature dependences of thermoelectric properties [(a) Seebeck coefficient, (b) electrical resistivity, and (c) thermal conductivity] for $\text{Mn}_{36.4-x}\text{Re}_x\text{Si}_{63.6}$ ($x = 0, 4, 6, 8$). (d) temperature dependence of dimensional figure of merit ZT

7.3 The strategy to enhance ZT for Re-HMS



Figure 7.5 Energy filtering effect by grain boundaries and reduction in lattice thermal conductivity by Re substitution.

In order to enhance ZT value of HMS, we simultaneously employed the energy filtering effect and heavy element substitution effect. The former increases power factor and the latter reduces lattice thermal conductivity. We selected 6 at.% Re sample and its grain size was modified by means of liquid quenching technique, subsequent annealing, and SPS.

7.4 Grain structure of LQ and SPS samples

The measured X-ray diffraction (XRD) patterns were plotted in Figs. 6 (a) and (b) for liquid quenched (LQ) samples before and after annealing, and sintered sample for $\text{Mn}_{30.36}\text{Re}_{6.0}\text{Si}_{63.64}$. The XRD pattern for the LQ sample showed broadening in peaks, as indicated by arrows. The peak broadening would be caused by the inhomogeneous compositions, small grain size, and/or heterogeneous strain in the sample. Notably, the peak broadening was disappeared after annealing at 1200 K for 5 hrs. We used the same temperature with that used in the SPS sintering. The crystallinity of samples changes after heat treatment process. The sharpened peaks were also observed after the SPS sintering at 1200 K.

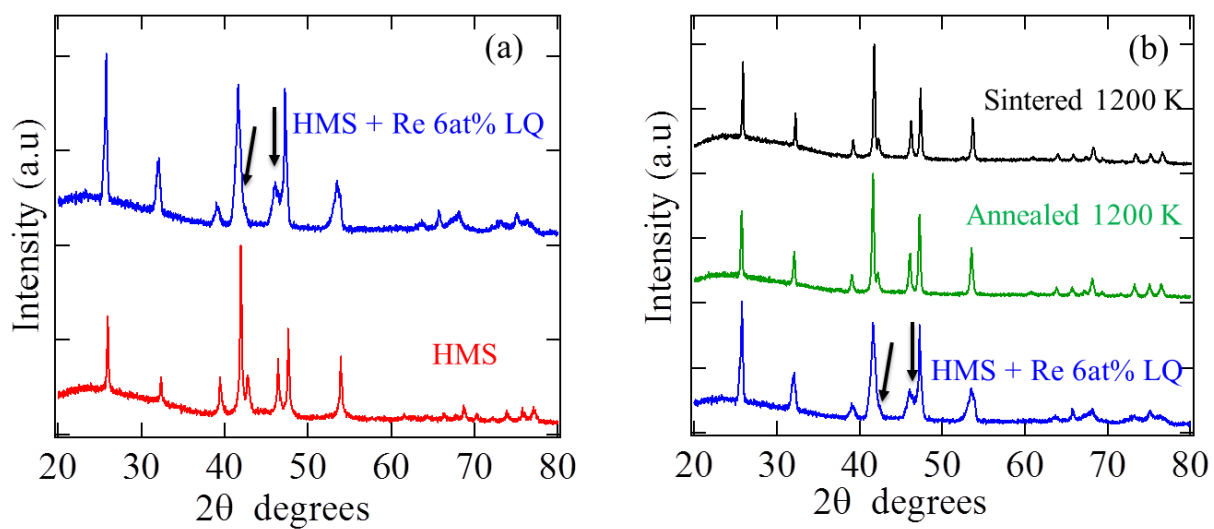


Figure 7.6 (a) XRD pattern of liquid quenched Re free and Re substituted HMS, (b) XRD patterns of non-annealed and annealed liquid quenched samples and sintered sample.

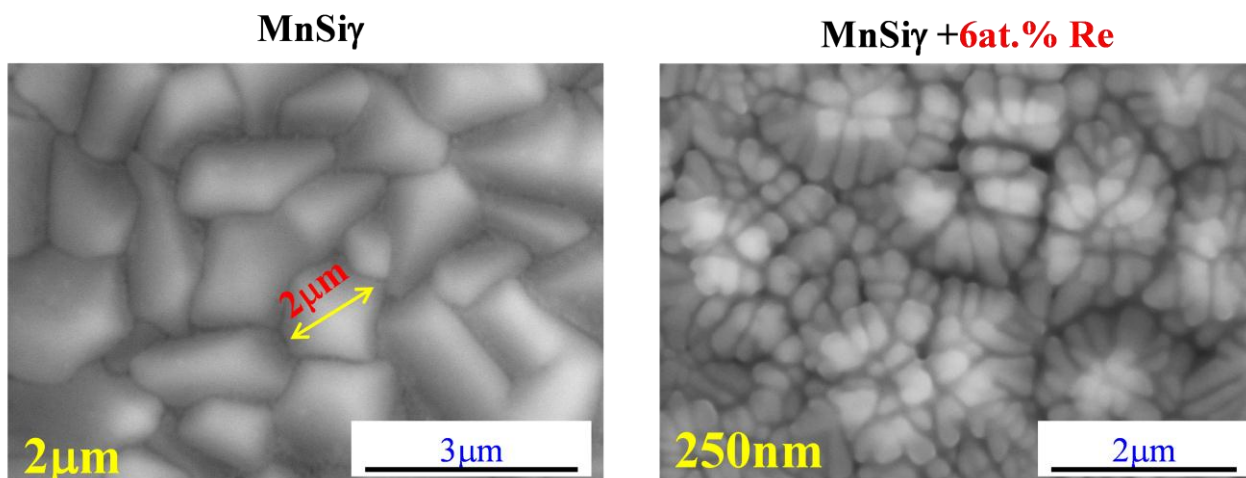


Figure 7.7 SEM for with (right) and without (left) Re substitution

Figure 7.7 shows the microstructure of liquid quenched ribbon samples with/without the Re substitution. The Re-free sample showed an average grain size of $\sim 2 \mu\text{m}$. In case of 6 at. % Re substitution, the grain size was further reduced to $\sim 250 \text{ nm}$ presumably due to change in rate of nucleation in rapid quenching process.

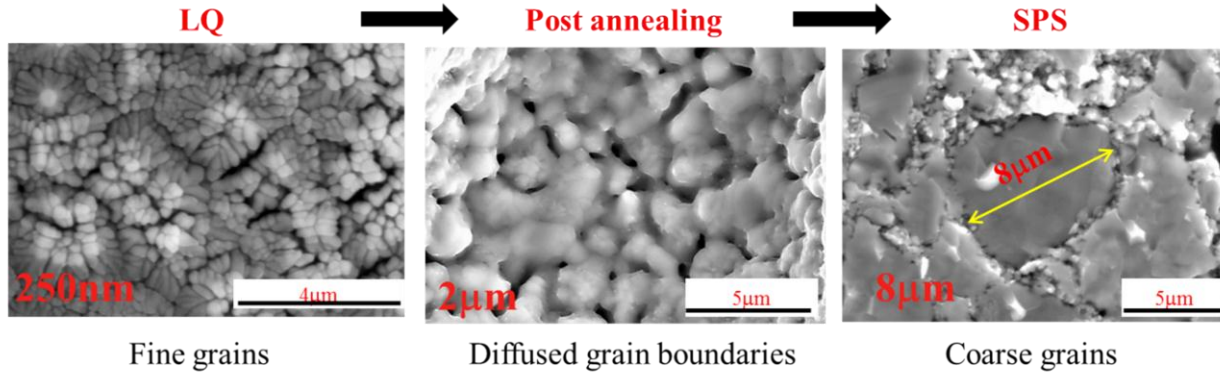


Figure 7.8 Thermal process dependent changes in microstructure of non-annealed, annealed and SPS sample

The heat treatment changed the grain structure. The non-annealed sample showed a fine microstructure but after the annealing and showed a diffused microstructure with mixed grains. The average grain size increased to $\sim 2 \mu\text{m}$ as shown in Fig. 7.8.

The SPS sample showed a drastic increase in grain size that was due to the joule heating in the spark plasma sintering. The joule heating should become most efficient at the resistive portions, which corresponds to the grain boundaries in the SPS sintering. The rapid grain boundary migrations increase the size of grains drastically. The grain boundary density was certainly decreased with the SPS process. Considering the very small grains, we expected large energy filtering effect as we observed in chapter 4.

7.5 Electron transport properties

We measured temperature dependent Seebeck coefficient and electrical resistivity for LQ sample, annealed sample and SPS in the temperature range from 300K to 700K. The temperature dependence were plotted in Fig. 7.9, and the room temperature values are plotted as a function of mean grain size in Fig. 9.

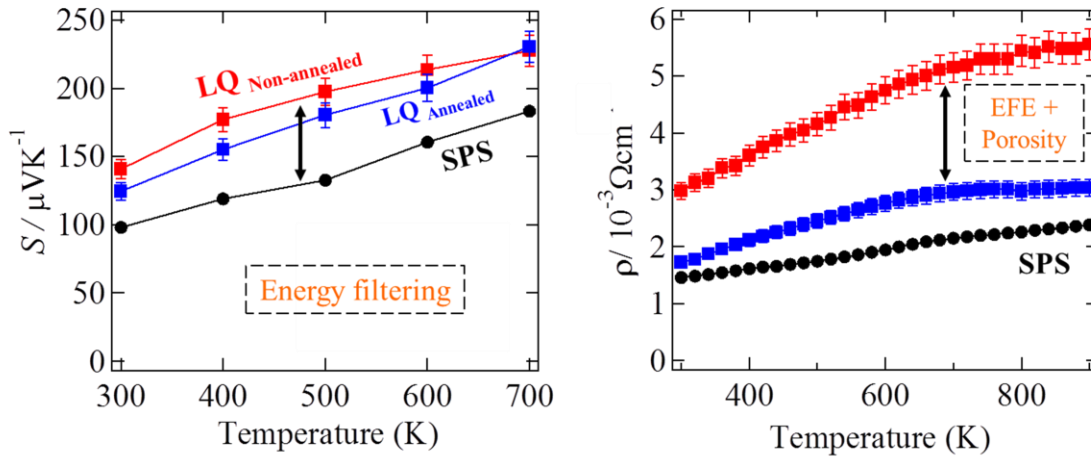


Figure 7.9 Temperature dependent Seebeck coefficient and electrical resistivity

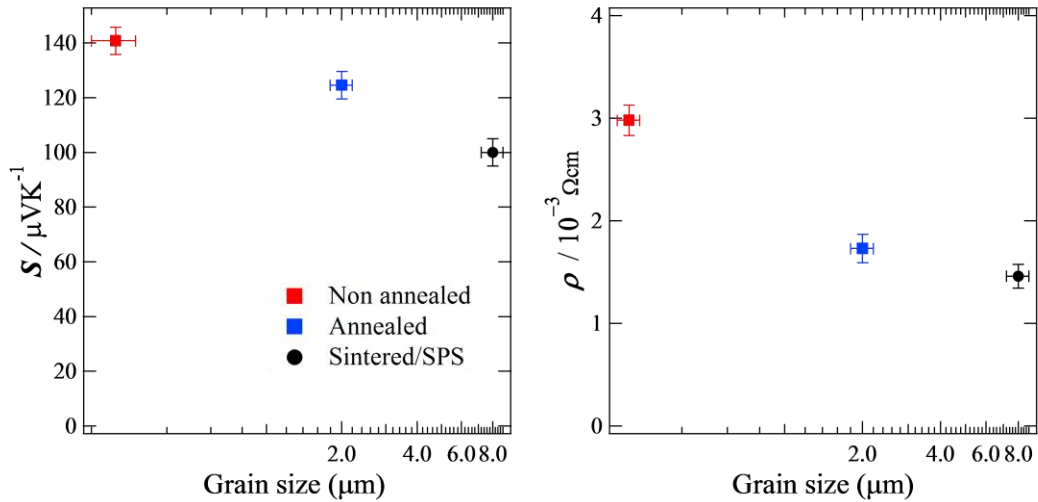


Figure 2.10 Seebeck and electrical resistivity as function of grain size.

The Seebeck coefficient and electrical resistivity obviously reduced with increasing mean grain size. This tendency was observed over the whole temperature range of measurement.

We consider that the grain size dependence of electron transport properties is well accounted for with the grain boundaries acting as an energy dependent scattering center. The increase in Seebeck coefficient for small grain samples was related to energy dependent scatterings, which naturally increases electrical resistivity.

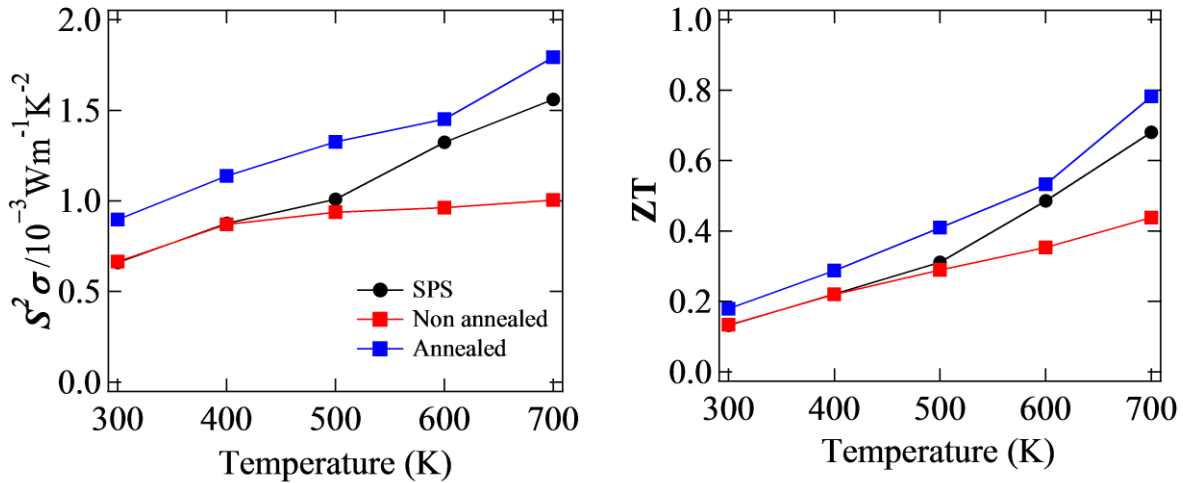


Figure 7.11 Temperature dependence of PF and ZT for non-annealed LQ, annealed LQ and SPS sample for 6 at% Re HMS.

The power factor and was calculated and plotted in Fig. 10 (a). We also calculated the value of ZT by applying the lattice thermal conductivity of SPS samples for the as-quenched LQ sample and the annealed LQ sample. The resulting value was plotted in Fig. 10 (b). The power factor was obviously improved for the annealed LQ samples and it led to an effective increase in ZT . The improvement was 30% at low temperatures below 400 K and 20 % at high temperatures above 600 K. The rough estimation using 20~30 % increase of ZT suggested that we may have $ZT \sim 1.4$ at around 900 K of HMS containing 6 at.% Re

7.5 Discussion

We observed that the as-quenched LQ samples with smallest grain size showed the smaller values both for PF and ZT . The reductions in PF and ZT were definitely contradictory with the energy filtering effect by grain boundaries. We realized that the as-quenched samples are characterized not only by the small grains but also by the voids, which were presumably introduced by the shrinkage of each grain at the cooling process. The SEM images shown in Fig.7.7 clearly prove the presence of such voids. Although the value of Seebeck coefficient is almost independent from the voids, the electrical resistivity sensitively is strongly influenced by the voids. Therefore the much higher electrical resistivity of as-quenched ribbon sample is caused not only by the increase of scattering probability at the grain boundary but also by the presence of voids. This consideration led to a prospect of further increase of PF with eliminating voids in the as-quenched ribbons (Fig. 7.12).

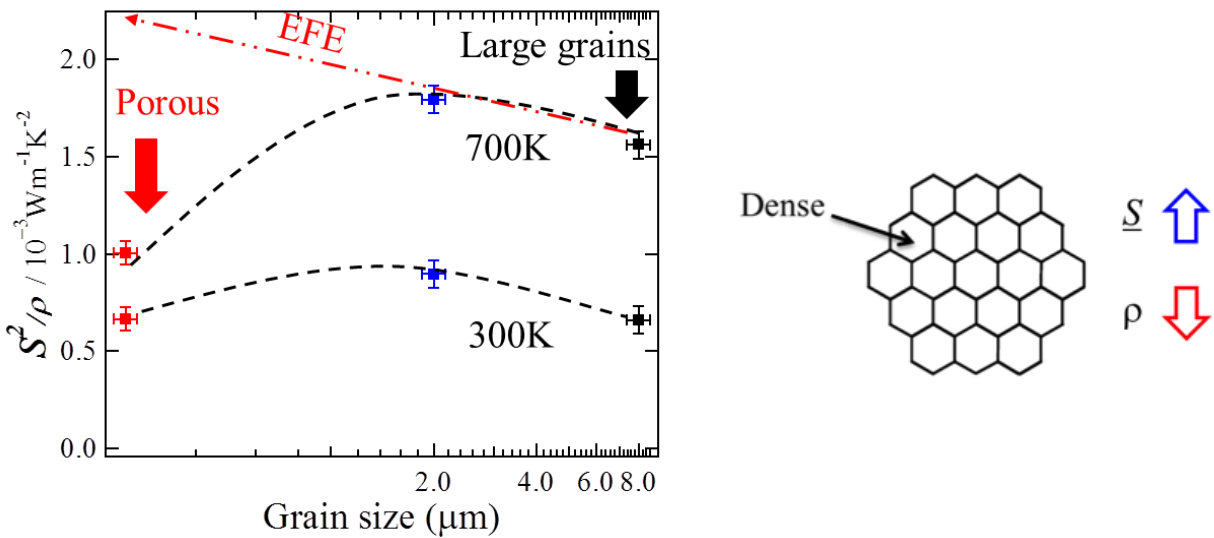


Figure 7.12 (a) Porosity dependent PF at 300k and 700K. (b) a schematic diagram showing dense microstructure to have large S and small ρ

As a consequence, we conclude that the fine grain structure in HMS provide us with a strong energy filtering effect but the voids would sometimes prevent us from obtaining a large enhancement in PF and ZT .

7.6 Conclusion

We succeeded in reducing the lattice thermal conductivity by a partial substitution of Re for Mn in HMS. The drastic reduction in lattice thermal conductivity improved ZT and it reached more than 1 at 920 K. The significant reduction of grain size (~ 250 nm) was observed for the Re-substituted HMS, which was realized under the combined effect of rapid quenching and solute substitution. We also observed improvement in power factor by implementing energy filtering effect by grain boundaries. The annealed liquid quenched samples showed 20-30% improvement. Hence, we estimate that the combined effect could increase the ZT value to 1.4.

7.7 References

1. Yamamoto, H. Miyazaki, and T. Takeuchi: *J. Appl. Phys.* **115**, 23708 (2014).
2. Yamamoto, H. Miyazaki, M. Inukai, Y. Nishino, and T. Takeuchi: *Jpn. J. Appl. Phys.*, **54**, 071801 (2015).
3. P. Villars, A. Prince, and H. Olkamoto, “*Handbook of Ternary Alloy Phase Diagrams Vol.10*” (ASM international, (1995).
4. A. Yamamoto, S. Ghodke, H. Miyazaki, M. Inukai, Y. Nishino, M. Matsunami, and T. Takeuchi, *J. Appl. Phys* **55**, 020301. (2016) doi:10.7567/JJAP.55.020301

Chapter 8

Conclusion

We have implemented different strategies to improve the performance of higher manganese silicides. The results are concluded as follows:

1. Effect of grain boundaries on TE properties of HMS

By implementing liquid quenching technique we succeeded in obtaining fine grain size in the samples. The significant effects of microstructure on TE properties were shown in Chapter 4, Chapter 7. The grain boundaries acted as scattering centers for low energy carriers and improved the PF by 20-30%, which was due to energy filtering effect.

2. Partial substitution of Cr/Fe/W/Re for HMS

The carrier concentration tuning was done with Cr and Fe substitution. The range of carrier tuning was increased by liquid quenching technique because the solubility limit of each element increased in HMS. The Cr substitution resulted in two maxima for PF and ZT at low and high Cr concentration, which explains a fine electronic structure of HMS. The solubility limits of Fe/W were also improved. We obtained n-type HMS with simultaneous substitution of Fe and W. The maximum ZT of 0.5 at 700 K was observed for n-type, which is the highest reported for n-type HMS.

The liquid quenched technique coupled with the element substitutions led to a significant reduction in grain size, and the smallest grain size of ~250 nm was observed for the samples of 5d element substitution for Mn. This was due to the increase in the number of nucleation sites in association with the solute elements.

The heavy element substitution for constituent elements was an effective strategy to reduce the lattice thermal conductivity and improved ZT of HMS to more than unity. The combined effects of the grain boundary energy selective scattering effect, the carrier tuning, and the heavy element substitution would improve ZT of Re substituted HMS close to 1.4 at high temperatures above 800 K.

